Contents

Part I

A search for highly ionising, short tracks at the CMS detector

1 Motivation

Supersymmetry is able to offer solutions to many unexplained phenomena in astrophysics and can solve many of the shortcomings of the Standard Model of particle physics (see Section ??). While SUSY has been analysed at previous particle colliders including Tevatron and LEP [1,2], the LHC with its high centre-of-mass energy offers a unique opportunity to investigate SUSY models with high particle masses that were not accessible in previous experiments.

Therefore, a variety of searches were hunting for SUSY during the Phase I run at the LHC in 2012. Proton-proton collision data from the CMS and ATLAS experiments were analysed with a strong focus on the search for SUSY in the strong production sector (e.g. [3–5]). As a consequence, wide regions of SUSY parameter space are already excluded. However, due to the unknown mechanism of supersymmetry breaking, the most general parametrisation of Supersymmetry introduces over 100 new parameters and thus opens up an incredibly large phenomenological space. Therefore, SUSY models can lead to a plethora of possible signatures at particle colliders. Such more "exotic" SUSY scenarios include models with compressed spectra, where two or more particles are nearly mass-degenerate.

Especially scenarios with a nearly mass-degenerate lightest chargino ($\tilde{\chi}_1^\pm$) and lightest neutralino ($\tilde{\chi}_1^0$) are very interesting from a theoretical perspective as they can help to explain the sources of the relic density [6–8]. In R-parity conserving Supersymmetry, such a mass-degeneracy naturally occurs in case of wino-like neutralinos and charginos, since the mass gap between W_3 and $W_{1/2}$ is fully determined by higher loop corrections (see Section ??). While it is not possible to explain the full relic density with thermally produced neutralinos for $m_{\tilde{\chi}_1^0} \lesssim 2.9\,\mathrm{TeV}$ [9], neutralinos can still be the dominant part if they are non-thermally produced via the decay of a long-lived particle such as a wino-like chargino. The enhanced annihilation cross section (called Sommerfeld enhancement) into WW-, ZZ- or ff-pairs for a wino-like dark matter candidate leads to an underprediction of the relic density if the neutralino and chargino masses are too small [10]. This underprediction can be cured, however, if there is an additional non-thermal production of dark matter that is caused by the decay of a long-lived chargino.

SUSY scenarios with nearly mass-degenerate particles have two distinctive phenomenological properties that require a very different search strategy compared to general SUSY searches. First, if mother and daughter particles in a two body decay are almost mass-degenerate ($\Delta m \lesssim 200\,\mathrm{MeV}$), the remaining decay product is very soft in p_T, making it

76   hard to detect. Second, the mother particle is long-lived due to phase space suppression
77   (see Section **??**) and may traverse several detector layers before decaying.

78   Although supersymmetric models with nearly mass-degenerate $\tilde{\chi}_1^{\pm}$ and $\tilde{\chi}_1^0$ lead to exotic
79   signatures with long-lived charginos and soft decay products, existing SUSY searches at
80   CMS can in principle be sensitive to these models. The exclusion power of existing SUSY
81   searches can be assessed by interpreting their results in terms of the fraction of excluded
82   parameter points in the phenomenological MSSM (see Section **??** for an introduction to
83   the pMSSM). The results of such a study which has been performed in [11] are shown in
84   Figure 1.1. It can be seen that general SUSY searches (blue area) are sensitive to shorter
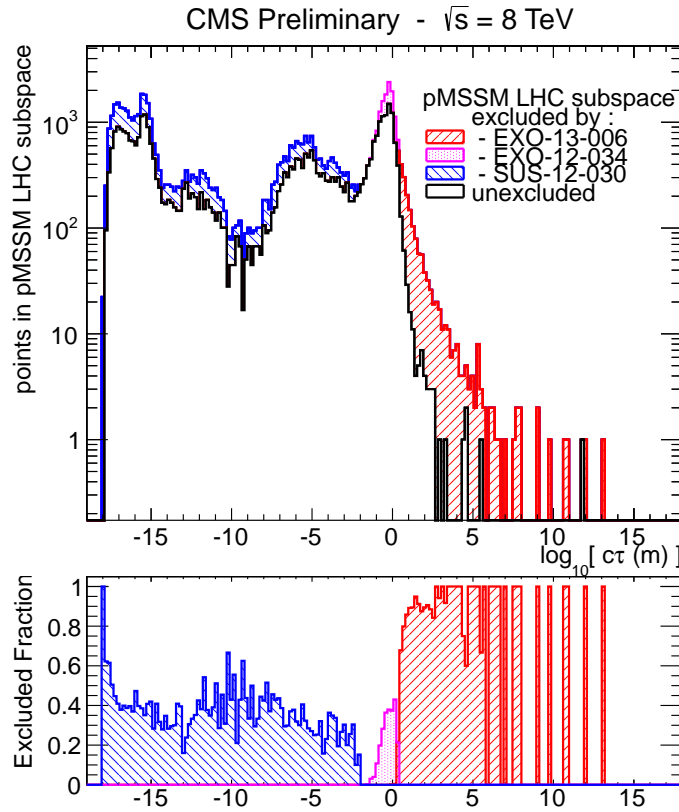
Figure 1.1: The number of excluded pMSSM points at 95% C.L. (upper part) and the
           fraction of excluded pMSSM points (bottom part) vs. the chargino lifetime for
           different CMS searches. Red area: the search for long-lived charged particles
           [12], Purple area: the search for disappearing tracks [11], Blue area: a collection
           of various general SUSY searches [13] The black line indicates the unexcluded
           pMSSM parameter points. The sampling of the parameter space points was
           done according to a prior probability density function which takes pre-LHC
           data and results from indirect SUSY searches into account (see [14] for further
           details). Taken from: [15].

chargino lifetimes ($c\tau \lesssim 10\,\mathrm{cm}$). Due to technical reasons[1], the general SUSY searches were never interpreted in the context of SUSY models with longer chargino lifetimes. Two existing searches, the search for long-lived charged particles [12] and the search for disappearing tracks [11] focus on long and intermediate chargino lifetimes, respectively. These two searches (purple and red areas) are sensitive to chargino lifetimes of $c\tau \gtrsim 35\,\mathrm{cm}$. Taken together, the existing searches exclude a large fraction of pMSSM points at different chargino lifetimes. However, there is a gap between the general SUSY searches and the search for disappearing tracks that is not accessible by any of the existing searches.

The here presented analysis aims at targeting this gap by optimising the search strategy for charginos with intermediate lifetimes of $10\,\mathrm{cm} \lesssim c\tau \lesssim 40\,\mathrm{cm}$. It is the first analysis at CMS focusing on two signature properties that are highly distinctive for charginos with intermediate lifetimes: first, the characteristically high ionisation losses of heavy charginos; second, short reconstructed tracks due to chargino decays early in the detector. The associated challenges and the general search strategy of this analysis will be presented in the next section.

2 General search strategy

At the LHC, there are several possible chargino production channels. Chargino pairs can be produced through a photon or a Z-boson exchange. The chargino then decays via a virtual W-boson to the lightest neutralino and a fermion pair (e. g. a pion). This process is illustrated in the Feynman diagram in Fig. 2.1. Other possible chargino pair production channels include the exchange of a supersymmetric Higgs boson or a t-channel squark exchange (Fig. 2.2).

Apart from pair production, charginos can be produced via the chargino neutralino production channel. On tree-level, there exist two production mechanisms: the s-channel W-boson exchange and the t-channel squark exchange (Fig. 2.3).

Alternatively, charginos can be produced via strong production modes, i. e. in cascade decays of new heavy particles, such as gluinos or squarks. In those cascade decays, other particles are additionally produced and lead therefore to different signatures in the detector. Thus, these strong production channels won't be considered in this analysis since they would require other optimised search strategies.

---

[1]The pMSSM interpretation relied on the use of fast simulation techniques which are not capable of simulating charginos with lifetimes $c\tau > 1\,\mathrm{cm}$.
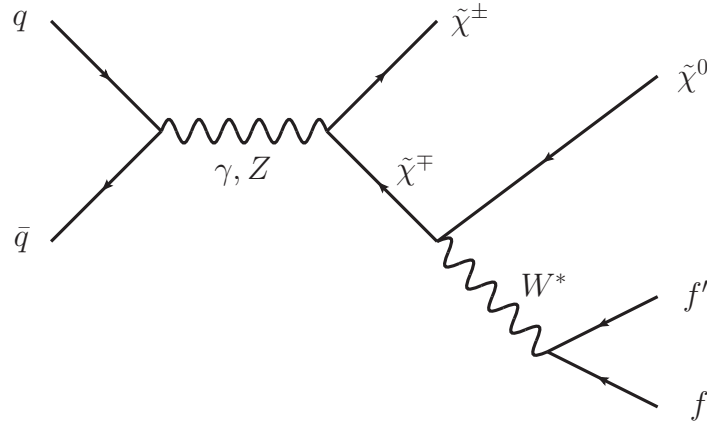
Figure 2.1: Feynman diagram of chargino pair production via gamma or Z-boson exchange and the subsequent decay via a virtual W-boson.
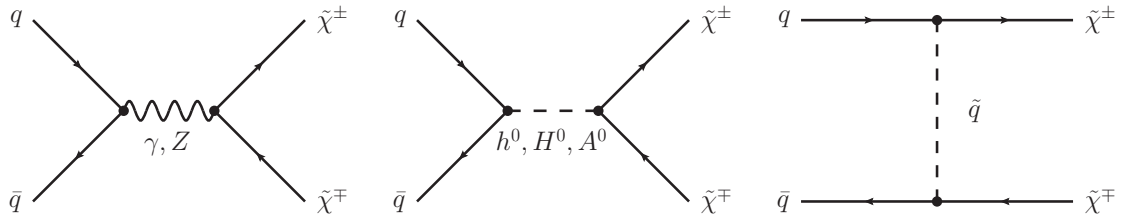

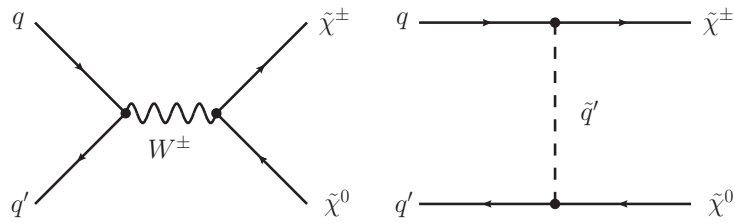Figure 2.2: Main tree-level diagrams for chargino pair production.

Figure 2.3: Main tree-level diagrams for chargino neutralino production.

₁₁₇ When searching for supersymmetric models with long-lived $\tilde{\chi}_1^{\pm}$, the strategy is of course
₁₁₈ highly dependent on the actual lifetime of the chargino. For long lifetimes, the chargino
₁₁₉ can reach the muon chambers and can be reconstructed as a muon even despite a longer
₁₂₀ time-of-flight [16]. For lower lifetimes, the chargino can already decay inside the detector
₁₂₁ (e. g. the tracker), and can hence not be reconstructed as a muon but leads to an isolated,
₁₂₂ potentially disappearing track in the tracker. The detector signatures of these two sce-
₁₂₃ narios are visualised in Fig. 2.4, where simulated chargino-chargino events are shown in a
₁₂₄ cross-sectional view of the CMS detector. In the left picture of Fig. 2.4, both charginos are
₁₂₅ reconstructed as muons, which can be seen in the energy deposition in the muon chambers.
₁₂₆ In the middle and right pictures both charginos have a lower lifetime of $c\tau = 0.5$ m and
₁₂₇ thus are only visible as tracks in the tracker, where both trajectories end inside the silicon
₁₂₈ strip tracker. Since this analysis targets a search for Supersymmetry with charginos of
₁₂₉ lifetimes between $c\tau \approx 10$ cm $- 40$ cm, the charginos decay rather early in the detector,
₁₃₀ even in the inner layers of the tracker. Thus, the signature of chargino events consists of
₁₃₁ isolated, short tracks and the signatures of the decay products, i. e. of a neutralino and a
₁₃₂ fermion pair.

₁₃₃ In case of R-parity conservation one of the chargino decay products, the neutralino, is
₁₃₄ stable and weakly interacting, thus traversing the detector without leaving any further
₁₃₅ signature. The missing transverse energy of the neutralino is balanced by the missing
₁₃₆ transverse energy of the second produced SUSY particle. This is either a neutralino or

(a)   (b)   (c)
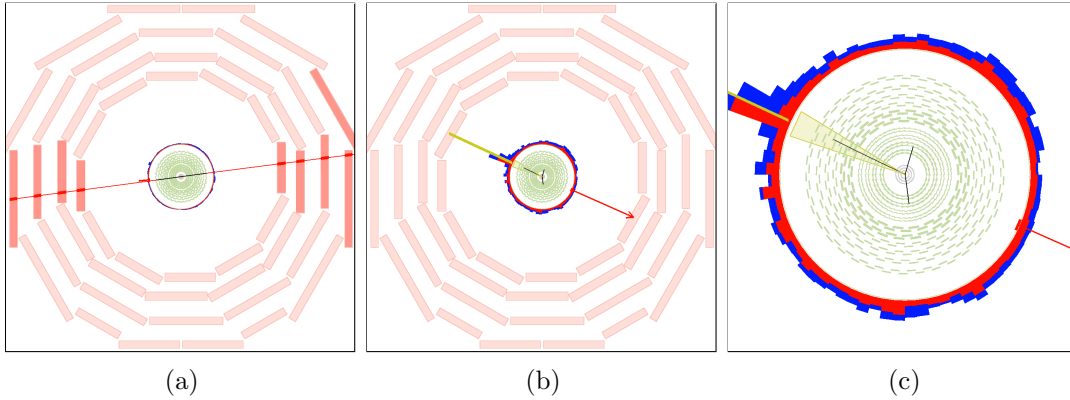
Figure 2.4: Visualisation of possible signatures of a chargino pair produced with a lifetime
of $c\tau = 10$ m (a) and a lifetime of $c\tau = 0.5$ m (b and c). The muon chambers
are the outer layers of the detector and are depicted as red boxes. The black
lines represent the reconstructed chargino tracks. The right picture is a zoom
of the picture in the middle. Here, only the cross-section of the tracker (green
wavy lines for the strip and grey lines for the pixel) is displayed. The red
arrow shows the missing transverse energy in the event. The red (blue) towers
correspond to the energy deposition in the ECAL (HCAL).

137 the decay products of the chargino in events with chargino pairs.

138 The signature of the other decay product, the fermion pair, can in principle be used to
139 select chargino events. However, for mass-degenerate charginos, it can be very hard or even
140 impossible to detect these fermions as will be explained in detail in the next paragraph.

141 First of all, the fermionic decay product (e. g. a pion) can usually not be reconstructed
142 because it does not origin from the primary vertex. Secondly, it is very low in momentum
143 because of the mass-degeneracy between $\tilde{\chi}_1^\pm$ and $\tilde{\chi}_1^0$. The typical momentum of a pion
144 originating from a chargino to neutralino decay in the $\tilde{\chi}_1^\pm$ rest frame is of the order

$$p_\pi \sim \sqrt{m_{\chi_1^\pm} - m_{\chi_1^0} - m_\pi}. \tag{2.1}$$

145 For a mass gap between $\tilde{\chi}_1^\pm$ and $\tilde{\chi}_1^0$ of $\Delta m = 150$ MeV, the pt distribution of the resulting
146 pion peaks at ~ 100 MeV and ends at $p_\mathrm{T} \sim 400$ MeV (Fig. 2.5).

147 If the transverse momentum of a particle is very low, the particle trajectory is much
148 more bended compared to a particle with higher p_T (see Fig. 2.6 for illustration). Due to
149 this bending, the track reconstruction efficiency of particles with a transverse momentum
150 below 1 GeV decreases rapidly, reaching around 40% for isolated pions with a p_T of 100 MeV
151 produced in the primary vertex [17]. It is therefore impossible to rely on a reconstruction
152 of the fermionic chargino decay products in this analysis.

153 In summary, the signature of chargino events in mass-degenerate SUSY models consists
154 only of a - potentially - disappearing track. Such a signature is very difficult to detect,
155 especially since CMS doesn't offer a dedicated track trigger so that triggering on the
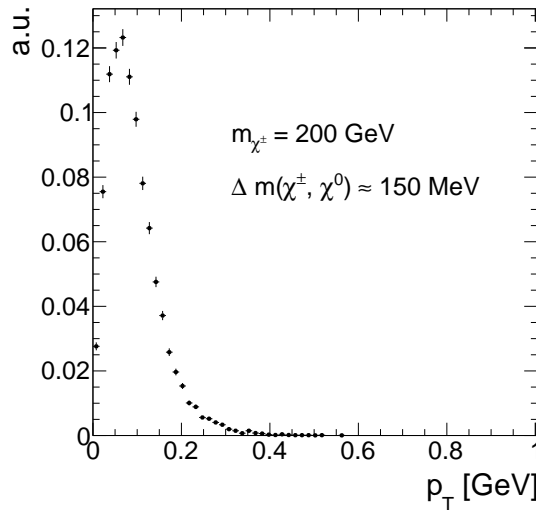

Figure 2.5: Transverse momentum distribution of pions coming from chargino decay into a neutralino with a mass gap of 150 MeV.

156 chargino track is impossible.

157 In order to search for such signatures, one therefore needs to trigger on other, less obvious
158 properties of chargino events. This analysis takes advantage of higher order contributions
159 to the Feynman diagrams shown in Figs. 2.2 and 2.3, resulting in initial state radiation
160 (ISR). If the initial quarks radiate a high p_T gluon, the resulting jet can be detected and can
161 offer a possibility to search for events with nothing more than isolated tracks. Furthermore,
162 the non-detection of the chargino's decay products plus a high p_T ISR jet lead to missing
163 transverse energy (MET) in the event. Exploiting these two circumstances, it is possible
164 to detect chargino-pair or chargino-neutralino events with the help of Jet+MET triggers.

165 Since Jet+MET triggers are not very specific for chargino events, it is important to
166 identify further track properties that can be used to select chargino candidates. One
167 distinctive property of charginos compared to SM particles is their high mass. Therefore,
168 charginos can be identified by selecting high p_T tracks. Furthermore, the energy loss
169 per path length (dE/dx) depends quadratically on the particle's mass for low velocities
170 ($0.2 < \beta\gamma < 0.9$):

$$\langle \frac{dE}{dx} \rangle = K \frac{m^2}{p^2} + C$$

171 Therefore, dE/dx constitutes a very nice discriminating variable for massive particles like
172 charginos against SM particles. The selection of chargino events in this analysis thus relies
173 on the selection of isolated high p_T tracks with high dE/dx values.

174 If the chargino decays before it has crossed the full pixel and strip detector, the as-
175 sociated track is disappearing. For low lifetimes, the tracks can be very short and can
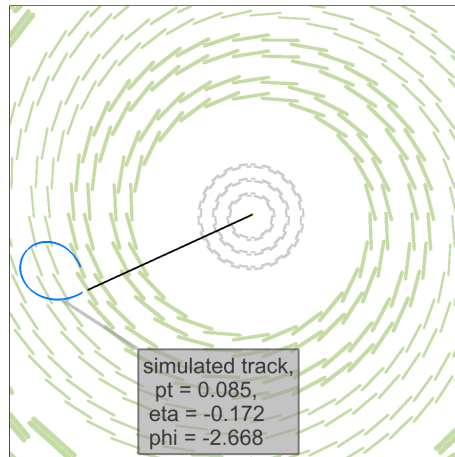

Figure 2.6: Cross-sectional view of the tracker (silicon strip (silicon pixel) tracker layers are
illustrated with green (grey) lines) and a simulated chargino track (black line)
decaying to a pion (bended blue line) with a p_T of ~85 MeV and a neutralino
(not visible).

have only a few hits in the detector. In order to reconstruct a particle's trajectory, a minimum of three hits are required since defining a helical path requires five parameters (see [17]). A specific challenge for this analysis is hence the combination of searching for short tracks and utilising the measurement of the energy deposition of the chargino. For very short tracks, eventually only passing the first couple of layers of the whole tracker system, the pixel tracker information becomes very important. Therefore, an accurate energy measurement in the pixel system is of great importance to this analysis. However, no other CMS analysis has used the energy information of the pixel tracker so far. This analysis thus requires a thorough study of the quality of the pixel energy calibration and, potentially, a recalibration in case the pixel energy calibration is not sufficient.

2.1 Comparison to earlier searches

As already mentioned before, there are two analyses at CMS at $\sqrt{s} = 8$ TeV with $20\,\mathrm{fb}^{-1}$ data that search for intermediate lifetime charginos, the search for long-lived charged particles [12] and the search for disappearing tracks [11]. The here presented analysis aims at achieving an increase in sensitivity towards shorter lifetimes compared to the earlier analyses in a twofold way. First, the selection is optimised for the inclusion of very short tracks. Second, the inclusion of the variable dE/dx is used to increase the search sensitivity compared to [11].

In [12], a minimum number of eight hits were required for every track, whereas [11] required a minimum of seven hits. This can be very inefficient for shorter lifetimes, where most of the charginos already decay shortly after the pixel tracker. In Fig. 2.7 (left), the normalised distribution of the number of measurements (N_{hits}) of chargino tracks is shown. It can be seen, that N_{hits} peaks at the minimal possible value needed for track reconstruction of $N_{\mathrm{hits}} = 3$ for lower lifetimes. For a lifetime of $c\tau = 50$ cm, a second peak at ~17 hits appears corresponding to the number of measurements when crossing all pixel barrel (3) and strip inner and outer barrel (6 from stereo and 8 from normal) layers. However, a notable fraction of $\sim 40\%$ of chargino tracks still has a number of measurements of $N_{\mathrm{hits}} < 8$.

It should be also mentioned, that the track reconstruction efficiency is sufficient for short chargino tracks, such that a loosening of the N_{hits} requirement is expected to be really improving the signal acceptance. The track reconstruction efficiency for different chargino decay points is depicted in Fig. 2.7 (right). For very short tracks ($N_{\mathrm{hits}} = 3$) the efficiency is still around 20%.

Additionally, the search for disappearing tracks which targets models with charginos decaying inside the tracker did not make use of the high energy deposition of heavy parti-
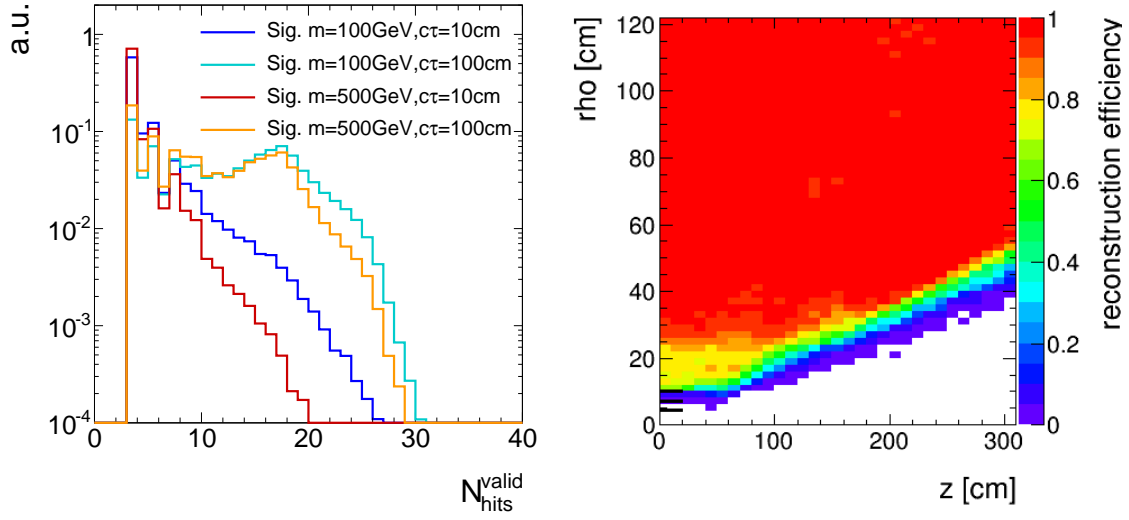
Figure 2.7: Left: Number of measurements in the tracker system N_{hits} for four different
signal lifetimes. Right: Probability to reconstruct a track (z) in dependency
of the chargino's decay point (x and y). More information on the generation
of the simulated signal samples can be found in Section 4.2.

cles. Although this variable was indeed used in the search for long-lived charged particles,
this search was not optimised for intermediate lifetimes (e. g. no explicit muon veto on the
selected tracks was required). Thus, it shows less sensitivity compared to the disappearing
track search in the lifetime region between $35\,\text{cm} \lesssim c\tau \lesssim 100\,\text{cm}$ (see Fig. 1.1).

To conclude, the general search strategy of the here presented analysis is to unite the
strategies of [12] and [11] and to lower the strong selection on the number of hits in these
analyses in order to get an optimised selection for lifetimes around $10\,\text{cm} \lesssim c\tau \lesssim 40\,\text{cm}$.

3 Improved dE/dx measurement for short tracks

As already pointed out in the previous chapter the inclusion of the pixel energy measure-
ments can increase the sensitivity when searching for short and highly ionising tracks.
While the silicon strip detector has already been calibrated as part of the search for long-
lived charged particles [12], no complete calibration has been done for the pixel silicon
tracker so far. To increase the discrimination power of dE/dx for short tracks, such a
calibration procedure is therefore conducted within this PHD thesis.

228   The CMS tracker system provides a measurement of the particle's energy loss for each
229   hit in the tracker. This is done by the detection of the number of electrons produced by
230   the ionisation of the silicon. A detailed introduction to the CMS tracker system and the
231   energy measurement can be found in Section **??**.

232   How to combine the single energy measurements for each tracker hit into one track
233   dE/dx estimator that can be used for analysis porpuses will be explained in the follow-
234   ing Section 3.1. The pixel energy calibration is then described in Section 3.2. How to
235   discrimate SM particles and beyond SM particles with the help of a dE/dx measurement
236   is discussed in Section 3.3, followed by the exploration of the achieved discrimination
237   improvements in Section 3.4.

238   3.1 Ionisation loss of charged particles

239   Energy losses for moderately relativistic charged particles travelling through matter are
240   mostly caused by ionisation effects. The mean energy loss per path length can be described
241   with the Bethe formula [18]:

$$\langle\frac{dE}{dx}\rangle = Kz^2\frac{Z}{A}\frac{1}{\beta^2}[\frac{1}{2}\ln\frac{2m_ec^2\beta^2\gamma^2T_{\max}}{I^2} - \beta^2 - \frac{\delta(\beta\gamma)}{2}]. \tag{3.1}$$

242   It is a function of the atomic number (Z), the atomic mass (A) of the absorber, and the
243   mean excitation energy (I) which is $173\,\mathrm{eV}$ for silicon [19]. $T_{\max}$ represents the maximum
244   energy transfer in a single collision. The relevant particle's properties are the velocity (β),
245   the Lorentz factor (γ) and the charge (z) of the incident particle. The density correction
246   $\delta(\beta\gamma)$ reduces the mean energy loss at high energies because of polarisation effects of the
247   material. The factor K is constant and is 0.307 in units of $\mathrm{MeV\,mol^{-1}cm^2}$. The Bethe
248   formula is valid if the main energy loss originates from ionisation effects, i. e. in a region
249   between $0.1\lesssim\beta\gamma\lesssim 1000$.

250   Even if widely used, the mean energy loss is a quantity which is "ill-defined experimen-
251   tally and is not useful for describing energy loss by single particles" [20]. The problem is
252   caused by the underlying probability distribution of one single dE/dx measurement (this
253   will be named $\Delta E/\Delta x$ throughout the following sections), which can be parametrised by
254   a Landau distribution [21]

$$p(x) = \frac{1}{\pi}\int_0^\infty e^{-t\log t - xt}\sin(\pi t)\,dt. \tag{3.2}$$

255   The Landau distribution has no free parameters. Its most probable value is around 0.222.
256   However, it is possible to introduce artificially a different most probable value and a
257   width (at half maximum) with $x\to\frac{x-\mathrm{MPV}}{\sigma} - 0.222$. The Landau distribution is a highly
258   asymmetric distribution with a long tail towards the right end (see Fig. 3.1). Theoretically
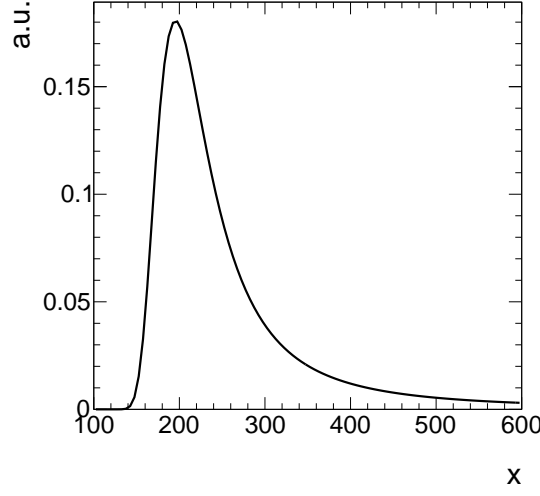
Figure 3.1: Illustration of the shape of a Landau distribution. Parameters were chosen as $\mu = 200$ and $\sigma = 20$.

it extends to infinite energies, however in nature the maximal deposited energy is of course limited by the particle's full energy. Because of its strong asymmetry, measurements of the mean energy loss per path length $\langle dE/dx \rangle$ with only a few single measurements are easily fluctuating towards high values. This makes the use of the mean energy loss described by the Bethe formula for the discrimination of new heavy particles problematic, because massive particles realease in general higher amounts of energy in matter.

A much better observable is the most probable value (MPV) of the Landau distribution. The MPV is much more stable compared to the mean and is not as easily fluctuating to higher dE/dx values. The most probable energy loss of a charged particle, Δ_p, can be described by the Landau-Vavilov-Bichsel equation [22]:

$$\Delta_p = \xi \left[\ln \frac{2m_e c^2 \beta^2 \gamma^2}{I} + \ln \frac{\xi}{I} + j - \beta^2 - \delta(\beta\gamma) \right], \tag{3.3}$$

with $\xi = (K/Z)\langle Z/A \rangle (x/\beta^2)$. The thickness of the absorber x appears explicitly in the Landau-Vavilov-Bichsel equation making the most probable energy loss per path length Δ_p/dx logarithmically dependent on x. A comparison between the Bethe mean energy loss $\langle dE/dx \rangle$ and the most probable energy loss Δ_p/dx for muons is shown in Fig. 3.2.

Particles such as muons are minimally ionising in silicon for $\beta\gamma \sim 3 - 4$. For higher momenta the deposited energies increase again reaching a plateau at around $\beta\gamma \sim 100$. However, new heavy charged particles would mainly be unrelativistic because of their high mass and would therefore deposit much higher energies in the detector. This makes dE/dx
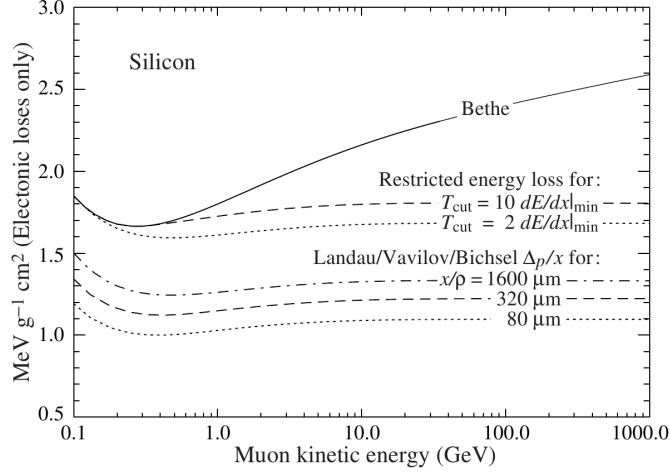
Figure 3.2: Comparison between the Bethe mean energy loss, restricted energy loss and the most probable energy loss described by the Landau-Vavilov-Bichsel function for muons for different values of absorber thickness of silicon. Taken from [20].

a very well discriminating variable. Thus, the energy loss per path length can be used to discriminate between SM particles and new heavy charged particles due to the different velocity distributions.

As said before, the most probable energy loss is much more stable compared to the Bethe mean energy loss. Still, combining only a few measurments of $\Delta E/\Delta x$ can also lead for Δ_p/dx to large fluctuations towards high dE/dx values. In order to estimate experimentally the most probable dE/dx value from only a few energy measurements, several "estimators" can be used that suppress a potential bias towards the high end without introducing a bias towards lower values [23]. One of the estimators for determining a tracks's dE/dx is the harmonic-2 estimator

$$I_{\mathrm{h}2} = \left(\frac{1}{N} \sum_{i=1}^{N} (\Delta E_i/\Delta x_i)^{-2} \right)^{-1/2}, \tag{3.4}$$

where $\Delta E_i/\Delta x_i$ corresponds to the ΔE and Δx measurement in the ith hit of the track. This estimator is known to be robust and not be easily biased by large fluctions in $\Delta E/\Delta x$ because of the supression by a factor of two.

The harmonic-2 estimator is also used for the pixel energy calibration described in the following section.

3.2 Energy calibration of the silicon pixel tracker

During Run I in 2012, the pixel silicon detector was continuously subjected to an energy calibration, a so-called gain calibration. Every pixel was calibrated to the same response, so that the whole pixel tracker should have been well inter-calibrated [24]. Unfortunately, due to various reasons, such as the imperfect constancy of the reference signal, or radiation and temperature induced changes, the energy calibration could not ensure a fully calibrated pixel tracker. This imperfection of the gain calibration can be seen in Fig. 3.3, where the mean of the harmonic-2 estimator for all tracks $\langle I_{h2} \rangle$ over the full data-taking period in 2012 is shown. Four different steps can be spotted. The first and the third steps correspond to changes in the settings of the tracker due to irradiation. The second and fourth step are induced by associated adjustments in the online gain calibration. Unfortunately, although the gain calibration was adjusted (even with some delay), it was not able to ensure a constant energy response of the pixel tracker over time. The variations of the dE/dx measurement over time of around 15% are too large to use dE/dx without a further calibration.

The following sections explain the method of the gain calibration of the pixel silicon tracker which is conducted for this analysis. It is splitted into two sections. The first section is dedicated to the gain inter-calibration of the pixel tracker which ensures a homogenious energy response of all tracker modules. In the second section, the absolute gain calibration is discussed. This calibration step is needed to ensure that the measurement of the energy realease of a particle is actually translated to the correct physical value.
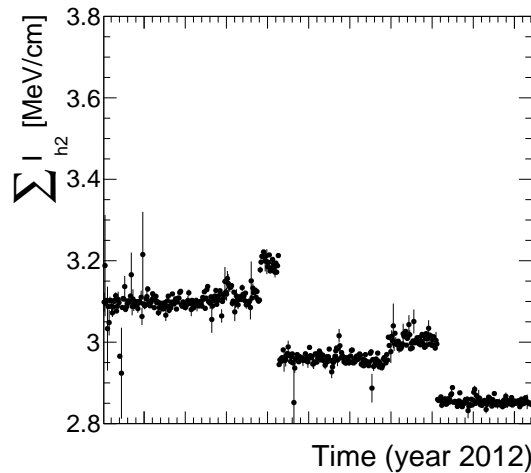

Figure 3.3: Mean of all track's dE/dx (harmonic-2 estimator) over the full year 2012. Only pixel hits are taken into account. Every data point corresponds to one run.

315   Detailed technical information about the pixel tracker can be found in Section **??**.

Inter-calibration of gain

317 The main goal of the gain calibration is to get a uniform response in the ionisation energy
318 loss dE/dx over the full data taking period in 2012. To also ensure a uniform response
319 over all modules within one time step, an additional inter-calibration on module level is
320 carried out. The inter-calibration can in principle be done on various levels: the highest
321 granularity would be a calibration on pixel level, followed by a calibration on read-out-
322 chip (ROC) level and then on module-level. Lower granularities in descending order are
323 rings (modules with same z-position) and finally layers (3 layers in the barrel and 4 disks
324 in the endcap). It is checked that all pixels and all ROCs (on one module) are well
325 inter-calibrated, such that the inter-calibration is finally done module-wise.

326   The gain calibration of the pixel silicon tracker is carried out with the help of minimally
327 ionising particles (MIPs). MIPs in this context are not defined as particles depositing a
328 minimum amount of energy, but more generally a small amount of energy. This denotes
329 all particles located at or near the plateau of the most probable dE/dx distribution vs.
330 momentum (see Fig. **??**). This approach ensures that all particles deposit similar amounts
331 of energy so that the variation due to different momenta is minimised. MIPs are selected
332 by a momentum selection of p > 2 GeV. Additionally, only tracks with at least eight
333 hits and a χ^2/n.d.o.f. < 3 are used to ensure a high-quality track reconstruction. A
334 sample containing around 50 million "minimum bias" events is used for calibration. The
335 "minimum bias" sample was specifically recorded for tracker calibration purposes. Its
336 distinctive property is that neither an online nor offline selection was applied.

337   For every module in the pixel tracker (there are 1440 modules in total), a distribution
338 of the energy loss per path length $\Delta E/\Delta x$ is built. The measurement of $\Delta E/\Delta x$ is
339 done in ADC counts per mm. ADC counts are a measure for the deposited charge after
340 digitisation. Figure 3.4 shows an example distribution for one module. The underlying
341 Landau distribution can be nicely seen. To extract the MPV for every module a fit to
342 the core distribution is performed. The fit is not only done with a Landau but a Landau
343 convoluted with a Gaussian function to be closer to the experimentally observed energy
344 spectrum. This also increases the fit performance and the stability of the fit. The path
345 length Δx is calculated with

$$\Delta x = d_{\text{module}_i} \cdot \cos(\phi_{\text{track}}),$$

346 where d_{module_i} is the thickness of module i and ϕ_{track} is the relative angle of the particle's
347 trajectory to the normal axis of the module. With the measured MPV extracted from the
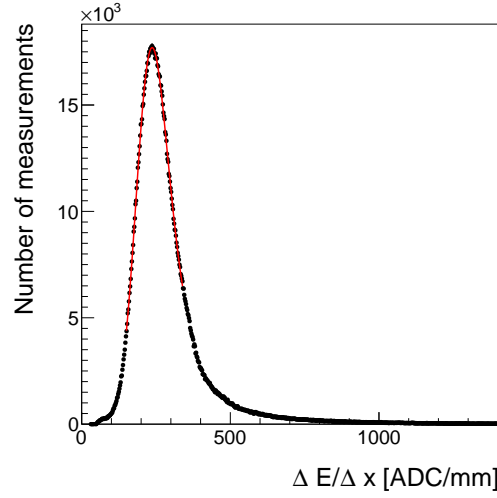
Figure 3.4: An example of the $\Delta E/\Delta x$ distribution measured in ADC count per mm for one module of the CMS pixel tracker. A Landau convoluted with a Gaussian is fitted to the core of the distribution in an iterative procedure.

fit, an inter-calibration factor is calculated for every module

$$c_{\text{inter}} = \frac{\text{MPV}_{\text{target}} \, [\text{ADC/mm}]}{\text{MPV} \, [\text{ADC/mm}]} = \frac{300 \cdot 265 \, \text{ADC/mm}}{\text{MPV} \, [\text{ADC/mm}]}.$$

The factor $300 \cdot 265$ ADC/mm is in principal an arbitrary number since the final response is adjusted by the absolute gain calibration described in the next section. However, it is chosen such that the measured calibration factors are close to one. The calibration factor can then be used to scale every single measurement in a module to a calibrated $\Delta E/\Delta x$ measurement

$$\frac{\Delta E}{\Delta x}_{\text{calibrated}} = c_{\text{inter}} \cdot \frac{\Delta E}{\Delta x}_{\text{uncalibrated}}$$

The determination of the calibration factor is done for every of the five time steps, shown in Fig. 3.3 independently, in order to get rid of the time dependency. The outcome of the application of the calibration factors to the single energy measurements in the pixel tracker can be seen in Fig. 3.5. The variation over time is indeed eliminated, resulting in a maximal time variation of less than $\sim 1\%$.

Additionally, the same procedure is carried out for a corresponding simulated data sample to ensure the inter-calibration of the pixel modules on all simulated samples.

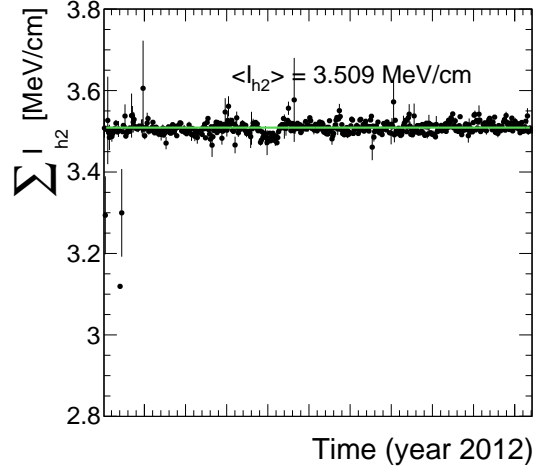Figure 3.5: Sum of all track's dE/dx (harmonic-2 estimator) over the full year 2012 af-
ter applying the calibration factors, resulting in an average dE/dx of 3.51
MeV/cm. Only pixel hits are taken into account. Every data point corre-
sponds to one run.

Absolute calibration of gain

As a final step, the targeted MPV being $\mathrm{MPV_{target}} = 300 \cdot 265\,\mathrm{ADC/mm}$ needs to be
translated to a meaningful physical quantity given in physical units (e. g. MeV/cm). That
means, that the charge measurement in ADC counts needs to be converted to the real
energy release of a particle. The relation between ΔE in ADC counts and the energy loss
in eV is given by

$$\Delta E\,[\,\mathrm{eV}] = c_{\mathrm{inter}} \cdot \Delta E\,[\mathrm{ADC}] \cdot \frac{N_e}{\mathrm{ADC}} \cdot 3.61\ \mathrm{eV}, \tag{3.5}$$

where N_e/ADC is the number of electrons which correspond to one calibrated ADC count
and 3.61 eV is the mean energy needed to create one electron-hole pair in silicon at -
10°C. Such an absolute gain calibration can be done with the help of several methods (all
explained in [23]). The absolute calibration of the silicon pixel tracker can rely on the
already conducted absolute calibration of the silicon strip detector. In [23], the absolute
gain calibration was done with the help of the most probable energy release per path length
of muons, theoretically described by the Landau-Vavilov-Bichsel formula in Eq. (3.3). To
calibrate the pixel tracker to the correct energy loss per path length it is therefore sufficient
to determine one calibration factor to relate the average dE/dx of all tracks in the pixel
tracker as shown in Fig. 3.5 to the average measured dE/dx in the strip tracker, shown in
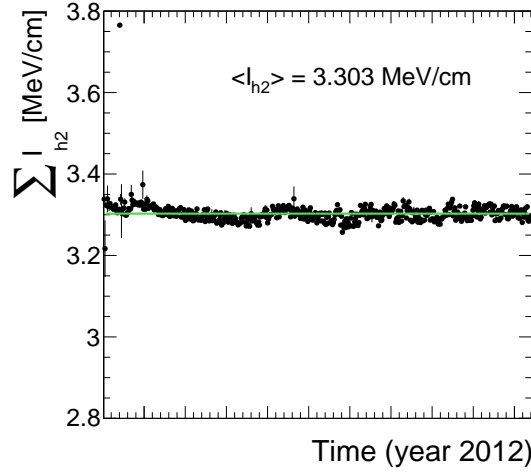
Figure 3.6: Mean of all track's dE/dx (harmonic-2 estimator) measured in the silicon strip detector over the full year 2012. The average most probable dE/dx is $I_{h2} = 3.303$ MeV/cm. Every data point corresponds to one run.

Fig. 3.6 by

$$c_{\text{absolute}} = \frac{\langle dE/dx_{\text{strip}} \rangle}{\langle dE/dx_{\text{pixel}} \rangle} = \frac{3.303}{3.509} = 0.941. \tag{3.6}$$

This factor is then applied on top of c_{inter} for all pixel modules.

Finally, an absolute calibration factor needs to be determined for the simulated samples, where the simulated pixel tracker is calibrated to the average dE/dx of the silicon strip measured in data.

3.3 Discrimination of highly-ionising particles

As mentioned before, it is difficult to find a robust estimator for the most probable energy loss of a particle, if only a few measurements of $\Delta E/\Delta x$ along the particle's trajectory are available. The harmonic-2 estimator I_{h2} was already introduced in Section 3.1 in Eq. (3.4). It is known to be a robust estimator not easily affected by large fluctuations in $\Delta E/\Delta x$. However, it was shown in [23] that a better discrimination between SM particles and possible new heavy particles can be achieved when using likelihood techniques, i. e. determining the probability that the set of all $\Delta E/\Delta x$ belonging to one track is actually compatible with the hypothetical probability distribution of a MIP.

That a measured sample has been drawn from a specific distribution can be tested with the co-called Smirnov-Cramér-von Mises test [25, 26]. It is deduced from the integral of the squared difference of the measured distribution $P_N(x)$ to the hypothesis distribution

394 $P(x)$

$$I_s = \int\limits_{-\infty}^{\infty} \left[P_N(x) - P(x) \right]^2 dP(x) \tag{3.7}$$

395 leading to a test statistics of

$$I_s = \frac{3}{N} \cdot \left(\frac{1}{12N} + \sum_{i=1}^{N} \left[P_i - \frac{2i-1}{2N} \right]^2 \right), \tag{3.8}$$

396 where N is the total number of energy measurements and P_i is the cumulative probability
397 that a MIP would release a $\Delta E / \Delta x$ equal or smaller than the measured $\Delta E / \Delta x$ with all
398 P_i arranged in increasing order.

399   However, this test statistics is not sensitive to the sign of the difference between the
400 measured and the theoretical distribution. It can therefore not distinguish between in-
401 compatibilities due to variations towards higher or lower energy deposits compared to the
402 hypothesis distribution. Thus it is not suitable for the discrimination between MIPs and
403 heavy new particles by dE/dx. A so-called Asymmetric Smirnov-Cramér-von Mises dis-
404 criminator was developed in [23] which is only sensitive to incompatibilities to the MIP
405 hypothesis towards higher energy depositions

$$I_{\mathrm{as}} = \frac{3}{N} \cdot \left(\frac{1}{12N} + \sum_{i=1}^{N} \left[P_i \cdot \left(P_i - \frac{2i-1}{2N} \right)^2 \right] \right). \tag{3.9}$$

406 A value of I_{as} close to zero indicates good compatibility with the MIP hypothesis, whereas
407 a value close to one indicates bad compatibility because of unexpectedly high energy losses.

408   The underlying probability P_i of the energy release for a given path length in the pixel
409 tracker is extracted from the same "Minimum bias" sample used for the pixel energy
410 calibration. In total 28 different templates each for a different given path length are
411 created. In Fig. 3.7 the probability distribution template for the pixel tracker in data and
412 simulation is shown. The corresponding templates for the energy release in the silicon
413 strip detector were already built by [23].

414   A comparison between the energy release by MIPs (I_{as}) in data and simulation for
415 high-quality tracks with $p > 5\,\mathrm{GeV}$ and $|\eta| < 2.1$ can be found in Fig. 3.8.

416   dE/dx shows good agreement in data and simulation for $I_{\mathrm{as}} < 0.1$. For larger values, I_{as}
417 shows a larger decrease in simulation than in measured data. For this reason a data-based
418 approach for analyses exploiting dE/dx information is needed.

419
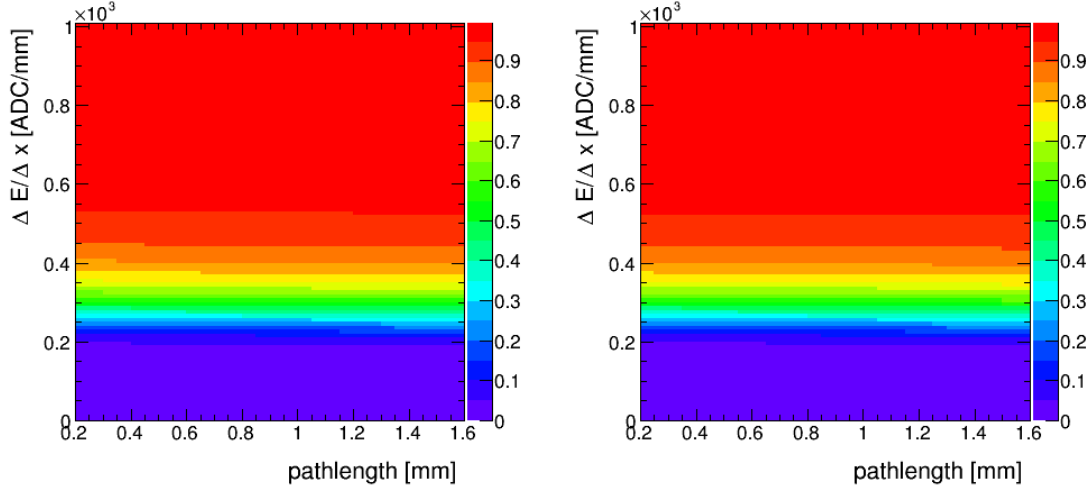
Figure 3.7: Cumulative probability for a MIP to release a $\Delta E/\Delta x$ (y-axis) vs. the path length (x-axis) in data (left) and simulation (right) for the pixel tracker based on the "Minimum bias" sample.

3.4 Discrimination improvements

The goal of including the pixel energy information is to increase the discrimination power of I_{as} between background and signal tracks, especially for shorter lifetimes. In Fig. 3.9, a comparison of the shapes of the energy release by MIPs and by signal tracks in simulation is shown (details about the simulated samples can be found in the next section Section 4.2). It can be seen, that the I_{as} distributions of all signal models show a larger tail towards $I_{\mathrm{as}} = 1$, whereas the I_{as} of the background is rapidly falling. The I_{as} distribution is not only influenced by the velocity (β) of a particle but also by the number of hits of a track. The influence of the velocity can be easily seen in Eq. (3.3). This in turn results in a dependency of I_{as} on the mass of the incident particle. However, also for charginos with same mass, the velocity is higher in average for shorter lifetimes. This is caused by the fact, that for shorter lifetimes (e.g. $c\tau = 10\,\mathrm{cm}$), already a sizable fraction of the charginos decay before reaching the tracker system. The probability of reaching the detector increases for higher velocities because of the boost, which can be clearly seen at the survival probability

$$P\left(t\right) = e^{-\frac{t}{\gamma\tau}}. \tag{3.10}$$
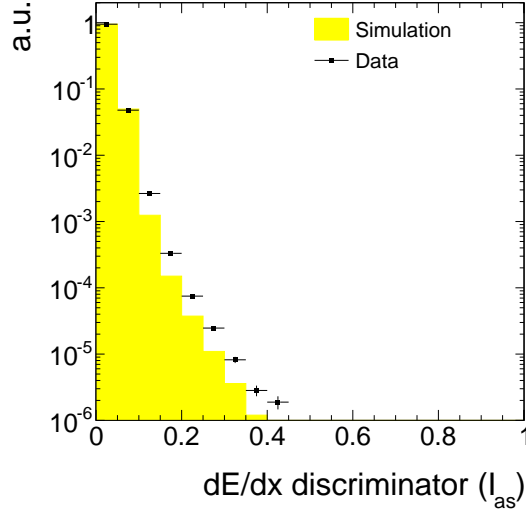
Figure 3.8: Normalised I_{as} distribution for MIPs from the minimum bias sample in data and simulation for high-quality (high purity as defined in [27], a minimum number of eight hits and no missing inner and middle hits) tracks with $p > 5\,\mathrm{GeV}$ and $|\eta| < 2.1$.
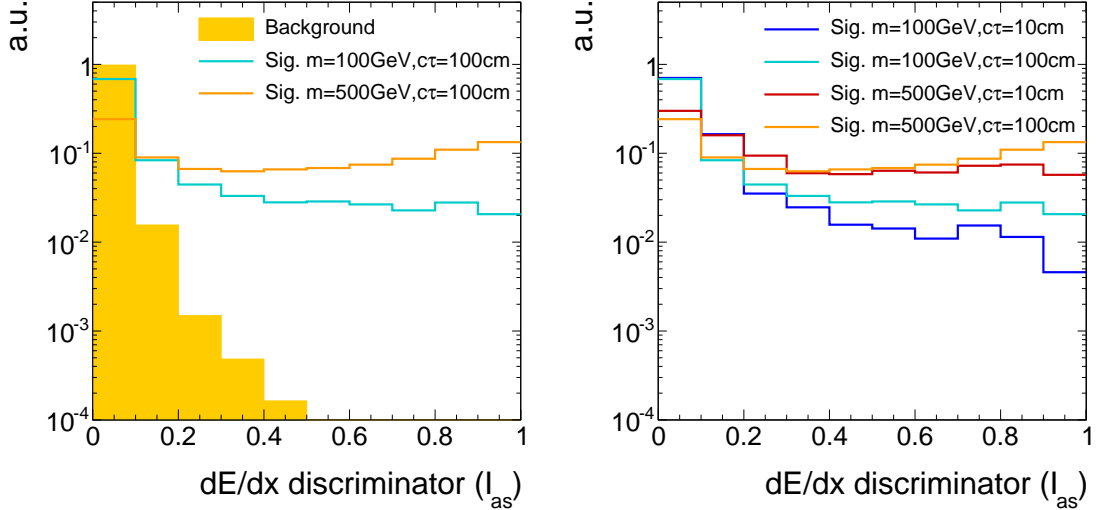
Figure 3.9: Normalised I_{as} distribution for simulated background and signal tracks (left) and for four different signal models (right) for high-purity tracks (as defined in [27]) with $p_{\mathrm{T}} > 10\,\mathrm{GeV}$ and $|\eta| < 2.1$. For the illustration of the background tracks' spectrum simulated $t\bar{t}$+jets events are used (more information about this sample is given in Section 4).

435 This means that the track reconstruction/selection lead to a biased average β for shorter
436 lifetimes which in turn lead to lower values of I_{as}.

437   The number of measurements in the tracker system defines the influence of single fluc-
438 tuations in $\Delta E/\Delta x$ on the I_{as} discriminator, because of the long right tail of the Landau
439 distribution, A low number of hits lead therefore to higher I_{as} values.

440   Thus, I_{as} for charginos with lower lifetimes are affected by two things: First, due to
441 the smaller number of measurements the chargino tends to higher I_{as} values. Second, low
442 lifetimes charginos have in average a higher velocity leading to lower I_{as} values. Both
443 effects can be seen in Fig. 3.9 (right). The large tail for longer lifetimes is caused by the
444 lower velocities, but the small surplus between 0.1 and 0.2 is caused by the smaller number
445 of measurements for lower lifetimes.

446

447   Finally, the impact of the additional $\Delta E/\Delta x$ information from the pixel tracker on the
448 selection efficiency of signal and background tracks is quantified. Figure 3.10 shows the
449 signal selection efficiency against the background selection efficiency for different selection
450 cuts in I_{as}, once including the pixel information and once without it. The background
451 selection efficiency is estimated with simulated W+jets events but was additionally checked
452 on simulated $t\bar{t}$+jets and QCD-multijet events (further information about the simulated
453 samples can be found in the next section). No significant difference between these processes
454 in the background selection efficiency was observed.

455   The signal selection efficiency and the background suppression depend on the mass and
456 the lifetime of the charginos. The discrimination power of I_{as} is much better for higher
457 masses as expected.

458   It can be seen that the inclusion of the pixel information increases the background
459 suppression for a given signal efficiency throughout the investigated signal models. This
460 background suppression improvement is most pronounced for very tight cuts on I_{as} (up to
461 a factor of 20) and still considerable for looser selections with signal efficiencies of around
462 40% (factor of 10).

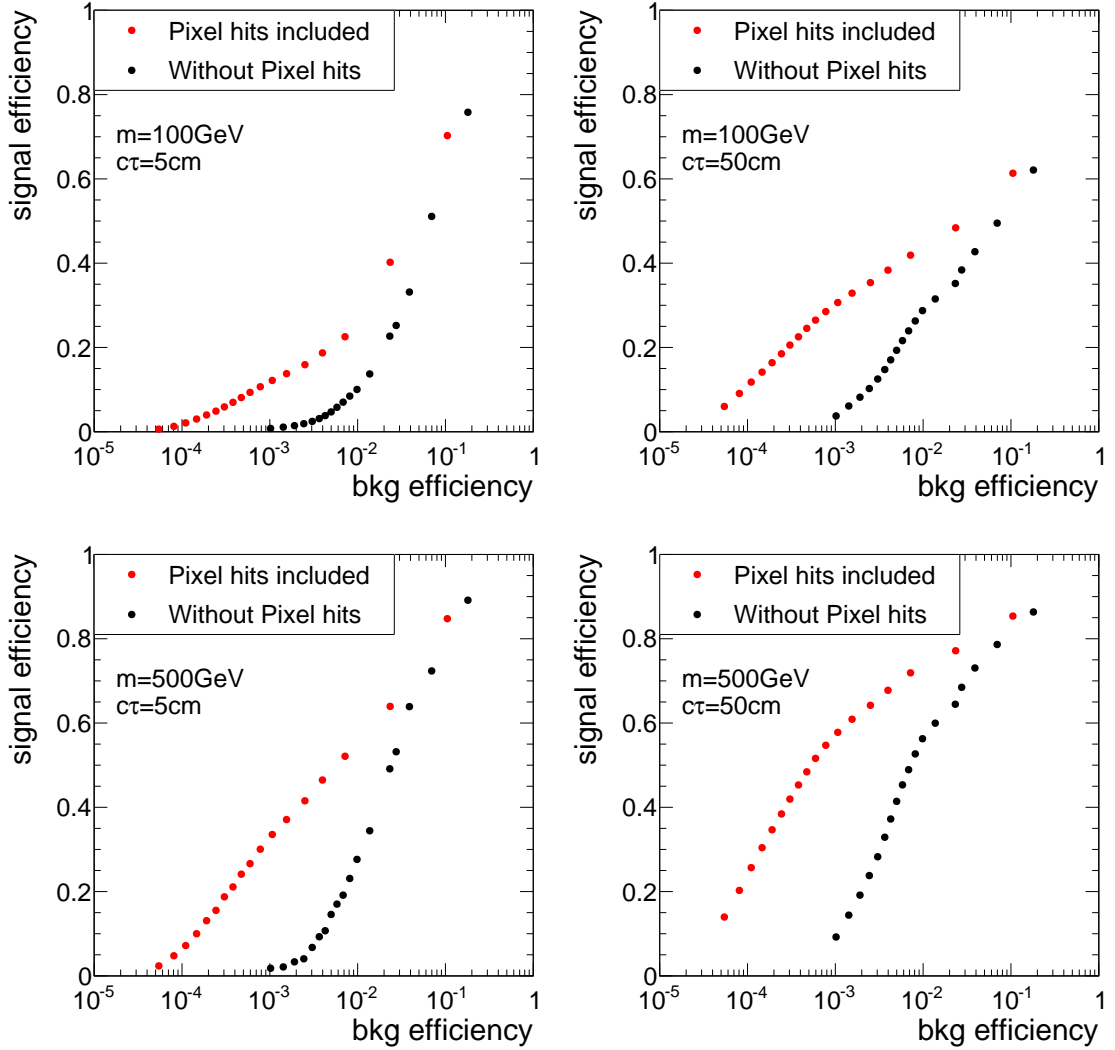Figure 3.10: Signal selection efficiency vs. background selection efficiency with (red) and without (black) pixel information. Each point correspond to one selection cut in I_{as}. The figure is based on a simulated W + jets sample and a simulated signal sample with chargino-chargino production, both subject to a selection of high-quality tracks (without a selection on N_{hits}) with $p_T > 10$ GeV.

4 Simulated samples

In order to design the search and to study background and signal characteristics, this analysis relies on simulated SM and SUSY datasets. An extensive introduction to the techniques and tools required for the simulation of SM and beyond SM processes can be found in Section **??**.

The following two sections present an overview of the SM (Section 4.1) and SUSY samples (Section 4.2) used in this search. All samples are reweighted to match the measured distribution of primary vertices in data.

4.1 Standard Model background samples

To investigate the sources of background, various simulated SM samples are used. Since this analysis aims at making use of dE/dx, a special data format of the simulated samples, the so-called RECO format, is required. Unfortunately, not all SM processes are available in this specific format making it impossible to compare the total number of events in simulation and real data. This, however, does not constitute a serious problem since this analysis will finally use data-based background estimation methods. The simulated SM datasets can still be used to compare the shapes of important distributions in simulation and data.[1]

In Table 4.1 all available SM samples used in this analysis are listed. Due to the size of the samples (between 5 and 70 TB) a reduction needs to be done in order to limit the storage space requirements. This is achieved by selecting only events which contain at least one jet with a minimum transverse momentum of $p_{\mathrm{T}} > 60\,\mathrm{GeV}$.

In addition, further simulated samples not containing the energy information are used. These are needed to study the background inclusively in the variable dE/dx. They are listed in Table 4.2.

---

[1]For example, the simulated $Z \to \nu\bar{\nu}$ + jets sample that can contribute to the background of this search via fake tracks is not available in RECO format. However, as the shape of important observables of fake tracks is independent of the underlying process, this background can be studied with a simulated W + jets sample.

Table 4.1: Available Standard Model background samples containing $\Delta E/\Delta x$ information that are used for background estimation studies.

Process	Cross section [pb]	$\mathcal{O}_{\text{calculation}}$
$W + \text{jets}$	36703.2	NNLO [28]
$t\bar{t} + \text{jets}$	245.8	NNLO [29]
$Z \to \ell\bar{\ell} + \text{jets}$ ($\ell = e, \mu, \tau$)	3531.9	NNLO [28]
QCD ($50\,\text{GeV} < \hat{p}_{\text{T}} < 1400\,\text{GeV}$)	9374794.2	LO

Table 4.2: Standard Model background samples without $\Delta E/\Delta x$ information.

Process	Cross section [pb]	$\mathcal{O}_{\text{calculation}}$
$W + \text{jets}$	36703.2	NNLO [28]
$Z \to \ell\bar{\ell} + \text{jets}$ ($\ell = e, \mu, \tau$)	3531.9	NNLO [28]

4.2 Signal samples

For the investigation of a possible SUSY signal, events containing either chargino pair production $q\bar{q} \to \tilde{\chi}_1^\pm \tilde{\chi}_1^\mp$ or chargino neutralino production $q\bar{q} \to \tilde{\chi}_1^\pm \tilde{\chi}_1^0$ are simulated. The simulation is done with the matrix-element event generator MADGRAPH [30] The parton showering and hadronisation processes are then simulated with PYTHIA [31]. Finally, the interactions of the generator-level particles with the detector material are simulated with GEANT4 [32, 33].

Furthermore, a special treatment for long-lived particles is required. In order to get a correct detector simulation of the energy loss of long-lived particles that decay after the beam pipe, the decay of the chargino cannot be simulated in the matrix-element generator but needs to be simulated within GEANT4.

To narrow down the required computing sources, the simulation is only done for a few lifetimes ($1\,\text{cm}$, $5\,\text{cm}$, $10\,\text{cm}$, $50\,\text{cm}$, $100\,\text{cm}$, $1\,000\,\text{cm}$ and $10\,000\,\text{cm}$). In order to scan in a high resolution over the lifetime space, other lifetimes are generated using lifetime reweighting. The weight for each event depends on the individual proper lifetime of the

chargino and is given by

$$w = \prod_{i=1}^{n} \frac{\tau^{\mathrm{gen}}}{\tau^{\mathrm{target}}} \cdot \exp\left[t_i \cdot \left(\frac{1}{\tau^{\mathrm{gen}}} - \frac{1}{\tau^{\mathrm{target}}}\right)\right],$$

where n is the number of charginos in the event, τ^{gen} is the generated mean lifetime in the particle's rest frame and t_i is the individual proper lifetime of the chargino. The targeted mean lifetime is given by τ^{target}. A derivation of this formula can be found in Appendix **??**. Using this reweighting procedure a good coverage of the lifetime space can be achieved with lifetimes of $c\tau = a \cdot 10^n$ for $n = 0, 1, 2, 3$ and $a = [1, 9]$. Figure 4.1 shows the exponential distribution of the individual proper lifetime of the charginos after the reweighting of a simulated sample with $c\tau^{\mathrm{gen}} = 50\,\mathrm{cm}$ to a lifetime of $c\tau^{\mathrm{target}} = 10\,\mathrm{cm}$. It can be seen that the reweighting procedure does indeed reproduce the targeted lifetime of $10\,\mathrm{cm}$.

All samples are generated for different masses of the chargino, but always almost mass-degenerate to the lightest neutralino. The mass gap between chargino and neutralino is set to $150\,\mathrm{MeV}$. However, as this analysis does not make use of the decay products of the chargino and the lifetime is independently set within GEANT4, the mass gap does not play any role. Six different masses from $100\,\mathrm{GeV}$ to $600\,\mathrm{GeV}$ are simulated. This leads to a total number of 42 signal samples. In Table 4.3 cross sections at $\sqrt{s} = 8\,\mathrm{TeV}$ for $\tilde{\chi}_1^{\pm}\tilde{\chi}_1^{\mp}$ and $\tilde{\chi}_1^{\pm}\tilde{\chi}_1^{0}$ production for wino-like charginos and neutralinos are listed [34, 35]. The cross

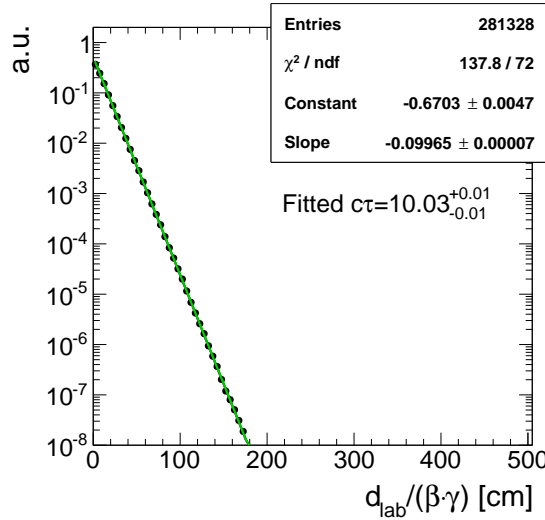Figure 4.1: Normalised distribution of the proper individual lifetime $d_{\mathrm{lab}}/(\beta\gamma)$ of all charginos contained in a signal sample with a generated lifetime of $c\tau^{\mathrm{gen}} = 50\,\mathrm{cm}$ reweighted to a lifetime of $c\tau^{\mathrm{target}} = 10\,\mathrm{cm}$. Fitting an exponential curve $a \cdot \exp\left[\frac{1}{c\tau}ct_i\right]$ yields $c\tau = 1./\mathrm{Slope} = 10\,\mathrm{cm}$.

section does not depend on the lifetime of the chargino.

Table 4.3: Simulated signal mass points with corresponding cross sections at NLO-NLL (NLO: next-to-leading order, NLL: next-to-leading logarithmic) accuracy for wino-like charginos.

$m_{\tilde{\chi}_1^\pm}\,[\,\mathrm{GeV}]$	$\sigma_{\tilde{\chi}_1^\pm \tilde{\chi}_1^\mp}\,[\,\mathrm{pb}]$	$\sigma_{\tilde{\chi}_1^0 \tilde{\chi}_1^\mp}\,[\,\mathrm{pb}]$
100	5.8234	11.5132
200	0.37924	0.77661
300	0.06751	0.14176
400	0.01751	0.03758
500	0.00553	0.01205
600	0.00196	0.00431

5 Event selection

5.1 Datasets and triggers

The analysis is performed on pp collision data recorded in the year 2012 at the CMS experiment for a centre-of-mass energy of $\sqrt{s} = 8\,\mathrm{TeV}$. In total an integrated luminosity of $19.7\,\mathrm{fb}^{-1}$ was recorded in 2012.

As outlined in Section 2, the detection of chargino tracks is a challenging task already on trigger level. Direct triggering of events containing chargino-like tracks is not possible because in 2012 there was no information about the tracking system available on trigger level L1. Furthermore, there is no intrinsic missing transverse energy in the event if the chargino decays inside the tracker. Therefore, this analysis uses initial state radiation for the detection of chargino events. If ISR occurs, it is possible to trigger on a high-p_T jet ($p_\mathrm{T}^{\mathrm{1st\ jet}}$) and missing transverse energy ($\not{E}_\mathrm{T}$).

For this purpose, several triggers are utilised in this analysis. An event is selected, if at least one of the three triggers in Table 5.1 fired.

Table 5.1: $\not{E}_T$ and $\not{E}_T$ + jet triggers used in this analysis together with the corresponding recorded integrated luminosity during the time when they were in place.

Trigger	Luminosity [fb^{-1}]
HLTMonoCentralPFJet80_PFMETnoMu95_NHEF0p95	5.3
HLTMonoCentralPFJet80_PFMETnoMu105_NHEF0p95	14.4
HLT_MET120_HBHENoiseCleaned	19.7

The HLTMonoCentralPFJet80_PFMETnoMu95_NHEF0p95 and HLTMonoCentralPF-Jet80_PFMETnoMu105_NHEF0p95 triggers both rely on the L1 ETM40 trigger which requires the missing energy to be larger than 40 GeV. On HLT level, they further require at least one particle-flow jet with $p_T > 80$ GeV and a missing transverse momentum (not taking into account the p_T of muons) to be larger than 95 GeV or 105 GeV respectively. Finally, the energy release by neutral hadrons must not be larger than 95% for all jets in the event. The HLTMonoCentralPFJet80_PFMETnoMu95_NHEF0p95 trigger was active during Run A and Run B in 2012 data taking, whereas HLTMonoCentralPF-Jet80_PFMETnoMu105_NHEF0p95 was in place during Run C and Run D in 2012.

The HLT_MET120_HBHENoiseCleaned trigger is based on the two L1 triggers ETM40 and ETM36 that are combined by a logical OR. On HLT level, the trigger requires that the missing energy measured in the calorimeter is larger than 120 GeV. The HBHENoise-filter reduces background from electronic noise in the HCAL.

The events that were selected by the described triggers are available in the MET datasets listed in Table 5.2. Again, because of the size of the datasets (~ 150 TB in total), a reduction of the size is achieved by selecting only events where one of the used triggers fired and that contain at least one jet with a minimum p_T of 50 GeV.

5.2 Selection of signal candidate events

In order to suppress events originating from Standard Model processes such as QCD-multijet events, W + jets, etc., a selection for signal-like tracks is applied. The signal candidate event selection closely follows the selection required in [36, 37]. It relies on event-based and track-based variables as described in the following two sections.

Table 5.2: MET data samples used in the search with the contained integrated luminosity.

Dataset	Luminosity [fb^{-1}]
/MET/Run2012A-22Jan2013-v1/RECO	0.876
/MET/Run2012B-22Jan2013-v1/RECO	4.412
/MET/Run2012C-22Jan2013-v1/RECO	7.055
/METParked/Run2012D-22Jan2013-v1/RECO	7.354

5.2.1 Event-based selection

First a selection on the quality of the vertex is applied in order to suppress cosmic events and noise from the beam halo . This selection includes requirements on the position of the vertex with respect to the beam axes and the number of degrees of freedom of the vertex which is strongly correlated to the number of tracks originating from the vertex [38]:

❖ The vertex must have at least four degrees of freedom: vtx with ≥ 4 d.o.f.

❖ The position of the vertex along the beam line must be within $24\,\mathrm{cm}$ with respect to the nominal interaction point: $|dz| \leq 24\,\mathrm{cm}$.

❖ The position in the transverse direction must be within $2\,\mathrm{cm}$ with respect to the nominal interaction point: $|d0| \leq 2\,\mathrm{cm}$.

After these selection cuts are applied the remaining events are subjected to a further pre-selection.

To maximise the signal acceptance, the trigger related selection cuts are chosen as close as possible to the trigger thresholds (see Section 5.1). In Fig. 5.1, the distributions of $\not{E}_\mathrm{T}$ and the transverse momentum of the leading jet, $p_\mathrm{T}^{1^{\mathrm{st}}\,\mathrm{jet}}$, are shown for different signal models. Only jets with $|\eta| < 2.4$ that fulfil the following further criteria are taken into account:

• Charged hadron energy fraction (CHF) > 0.2

• Charged electromagnetic energy fraction (CEF) < 0.5

• Neutral hadron energy fraction (NHF) < 0.7

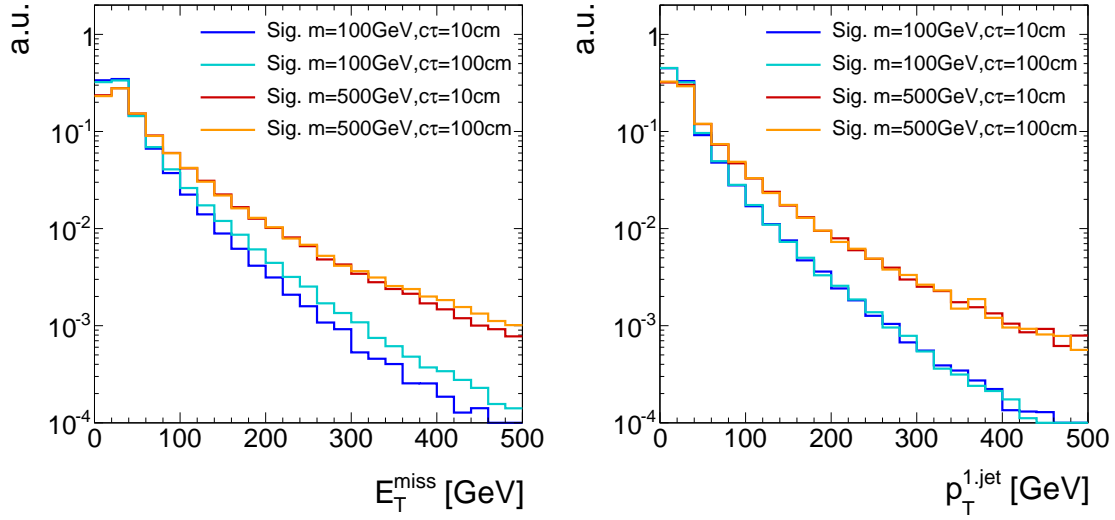• Neutral electromagnetic energy fraction (NEF) < 0.7.

Figure 5.1: Normalised distributions of the missing transverse momentum (left) and the transverse momentum of the leading jet (right) for four different signal models.

These additional jet quality criteria ensure that noise from cosmic and beam halo muons and high-p_T photons and electrons is suppressed [39].

The trigger efficiency as a function of $\not{E}_T$ and $p_T^{1^{st}\,jet}$ was determined within [40] with a single-muon reference sample. The trigger paths become fully efficient for $p_T^{1^{st}\,jet} \gtrsim 110\,\text{GeV}$ and $\not{E}_T \gtrsim 220\,\text{GeV}$ [39]. However, it can be seen in Fig. 5.1 that for a selection of $\not{E}_T > 220\,\text{GeV}$ more than 99% of the signal events are rejected.

In order to achieve a reasonable signal acceptance, this search imposes a trigger selection closer to the intrinsic trigger thresholds. The trigger requirements are as follows:

❖ There is at least one jet within $|\eta| < 2.4$ with transverse momentum larger than 110 GeV which fulfils the above mentioned jet noise cleaning criteria: $p_T^{1^{st}\,jet} > 110\,\text{GeV}$.

❖ The missing transverse momentum must be larger than 100 GeV: $\not{E}_T > 100\,\text{GeV}$

These requirements result in a trigger efficiency of 100% in the variable $p_T^{1^{st}\,jet}$ and $\sim 20\%$ in the variable $\not{E}_T$ at the cut thresholds [39].

Because of the huge cross section, QCD-multijet events are frequently produced at the LHC. Due to jet energy mismeasurements, they can also contribute to data samples recorded with MET triggers. Therefore, special requirements are enforced in order to suppress events emerging from strong production processes. QCD-multijet events can be characterised by topologies where two jets are almost back-to back. Additionally, in QCD-multijet events the missing energy is usually aligned with one of the leading jets in
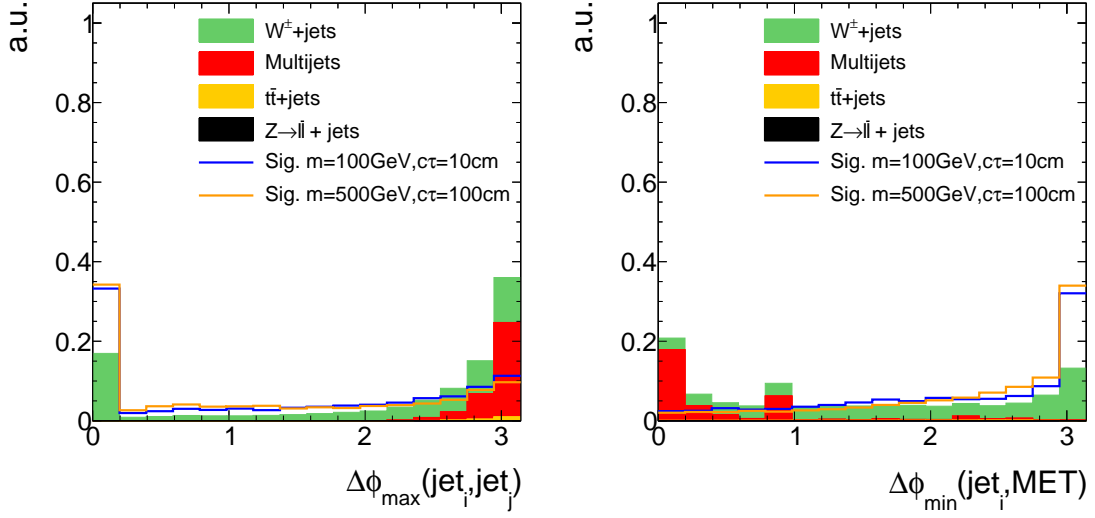
Figure 5.2: Maximum $\Delta\phi$ between any of two jets (left) and the minimum $\Delta\phi$ between the $\slashed{E}_{\mathrm{T}}$ vector and any of the two leading jets (right) normalised to unit area after the trigger selection. Only jets with $p_{\mathrm{T}} > 20\,\mathrm{GeV}$ and $|\eta| < 4.5$ are considered.

the event. Figure 5.2 shows the maximum $\Delta\phi$ of any of two jets and the minimum $\Delta\phi$ between the $\slashed{E}_{\mathrm{T}}$ vector and any of the two leading jets for the SM background and two different signal datasets.

The following two requirements are sufficient to suppress QCD-multijet events efficiently:

❖ $\Delta\phi$ between any of two jets (with $p_{\mathrm{T}} > 20\,\mathrm{GeV}$ and $|\eta| < 4.5$) in the event must be smaller than 2.5.

❖ $\Delta\phi$ between any of the two leading jets (with $p_{\mathrm{T}} > 20\,\mathrm{GeV}$ and $|\eta| < 4.5$) and the $\slashed{E}_{\mathrm{T}}$ must be larger than 0.5.

5.2.2 Candidate track selection

After the reduction of background processes with event-based variables, a track-based selection is carried out. To get an optimised selection for possible chargino tracks several signal track characteristics are exploited.

First, a selection of high-quality tracks is enforced:

❖ The track must be of "high purity" as defined in [27].

❖ The track is required to have no missing middle or inner hits: $N_{\mathrm{miss}}^{\mathrm{middle/inner}} = 0$

616 ❖ The radial and longitudinal distance of the track to the primary vertex must be
617 small: $|d0| < 0.02\,\text{cm}$, $|dz| < 0.5\,\text{cm}$.

618 In Figs. 5.3 and 5.4, the power of the latter two quality selection cuts is shown.
619
620 Furthermore, a first kinematic preselection is applied:

621 ❖ Only tracks in the central region are considered : $|\eta| < 2.1$.

622 ❖ Only tracks with a minimum transverse momentum of 20 GeV are considered:
623 $p_{\text{T}} > 20\,\text{GeV}$.
624

625 In order to suppress background tracks emerging from SM processes, an electron, muon
626 and tau veto is applied. This rejects tracks that are close to a reconstructed electron,
627 muon or tau. Additionally, the candidate track must not be close to a jet ($p_{\text{T}} > 20\,\text{GeV}$
628 and $|\eta| < 4.5$).
629 Unfortunately, the lepton veto selection cuts lack efficiency in some of the detector
630 directions. For example, the reconstruction of an electron easily fails in the direction of
631 a dead ECAL cell. This reduces the discrimination power of the electron veto. For this
632 reason, tracks that point towards dead or noisy ECAL cells are rejected. A general list of
633 dead and noisy ECAL cells is provided centrally at CMS. Further dead cells were identified
634 within a study in [36,37] resulting in a total number of 1234 dead or noisy ECAL channels.
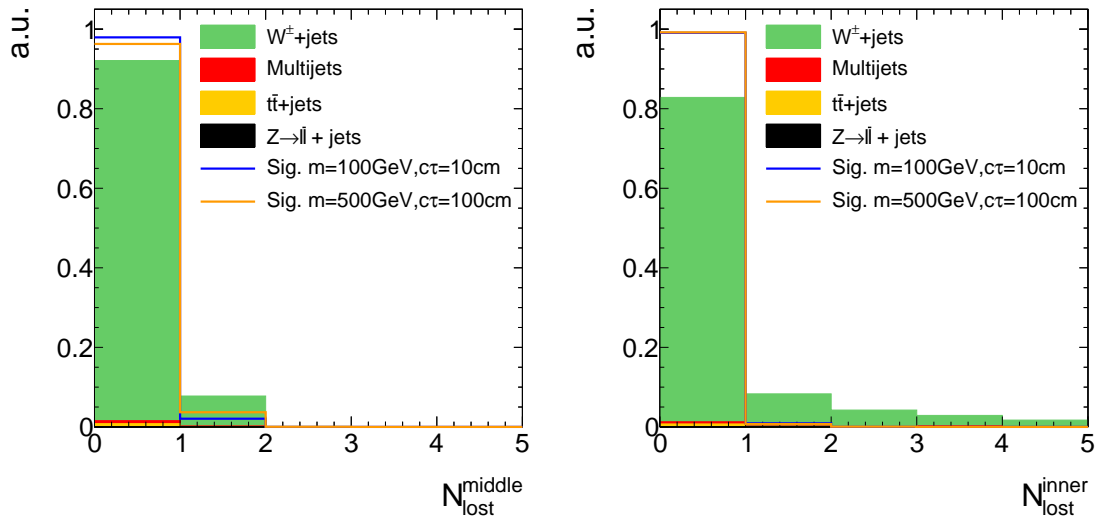

Figure 5.3: Number of missing middle (left) and inner (right) hits of background and signal
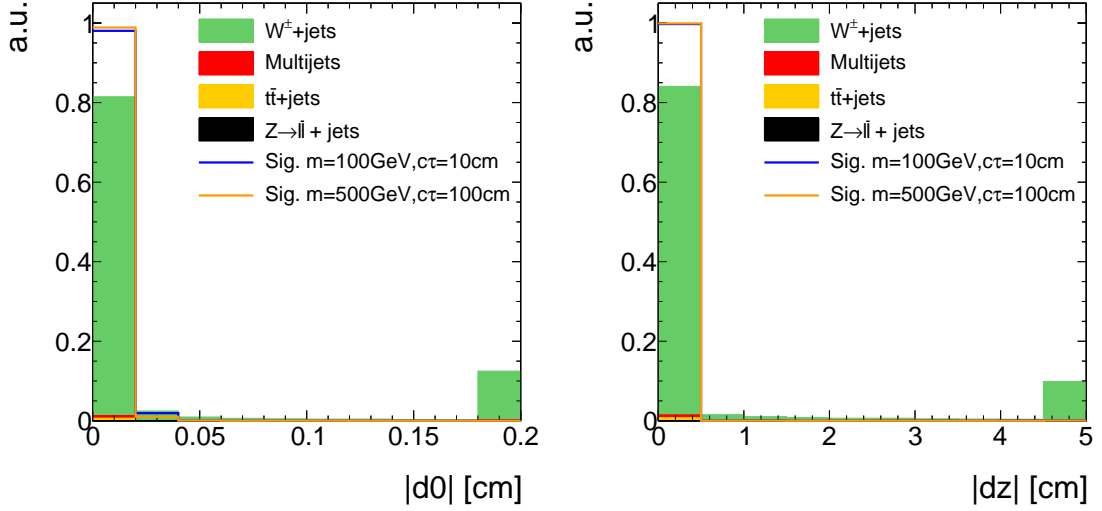tracks after trigger requirements and QCD suppression cuts.

Figure 5.4: Absolute value of the radial (left) and longitudinal (right) distance between the track and the primary vertex after trigger requirements and multijet suppression cuts. All events with a candidate track with a radial (longitudinal) distance larger than 0.2 cm (5 cm) are contained in the last bin.

These are illustrated in Fig. 5.5 showing a map of all ECAL channels not considered in the search.

Additionally, tracks that point towards intermodule gaps of ECAL cells or to the ECAL barrel endcap gap at $1.42 < |\eta| < 1.65$ are rejected. A list of the ECAL intermodule gaps, that is supplied centrally at CMS, is given in Table 5.3.

The muon reconstruction is less efficient for muons in detector regions with bad cathode strip chambers (CSC). These bad chambers are also identified centrally at CMS and their η and ϕ values are visualised in Fig. 5.6. Thus, also tracks pointing towards these regions within a distance of $\Delta R < 0.25$ are rejected.

To summarise, the candidate track must fulfil the following selection criteria:

❖ The track must not be within a cone of $\Delta R < 0.15$ to a reconstructed standalone, tracker or global muon with a transverse momentum larger than $10\,\mathrm{GeV}$ (see Section **??** for details on the different muon definitions).

❖ The track must not be within a cone of $\Delta R < 0.15$ to a reconstructed electron with a transverse momentum larger than $10\,\mathrm{GeV}$ (see Section **??** for details on the electron reconstruction).

❖ The track must not be within a cone of $\Delta R < 0.15$ to a reconstructed tau with $p_\mathrm{T} > 20\,\mathrm{GeV}$ and $|\eta| < 2.3$ (see Section **??** for details on the tau reconstruction).
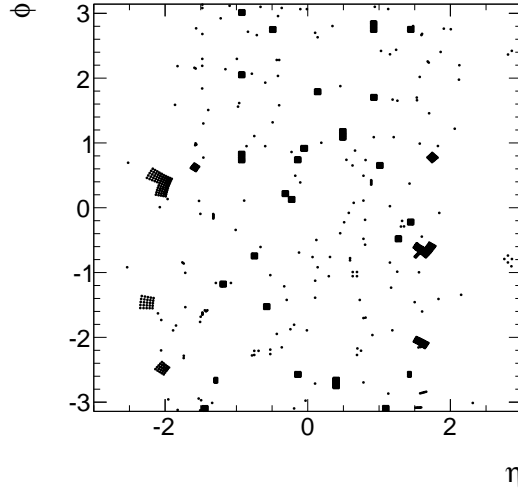
Figure 5.5: Visualisation of dead and noisy ECAL cells in the detector's $\phi - \eta$ plane according to [36, 37].

Some loose isolation requirements are enforced to protect the tau reconstruction from jet contamination.

❖ The track must not be within a cone of $\Delta R < 0.5$ to a reconstructed jet ($p_\text{T} > 20\,\text{GeV}$ and $|\eta| < 4.5$).

❖ Veto tracks within a cone of $\Delta R < 0.05$ to a dead or noisy ECAL cell (visualised in Fig. 5.5).

Table 5.3: Intermodule ECAL gaps.

η-ranges
-1.14018 $< \eta <$ -1.1439
-0.791884 $< \eta <$ -0.796051
-0.44356 $< \eta <$ -0.447911
0.00238527 $< \eta <$ -0.00330793
0.446183 $< \eta <$ 0.441949
0.793955 $< \eta <$ 0.789963
1.14164 $< \eta <$ 1.13812
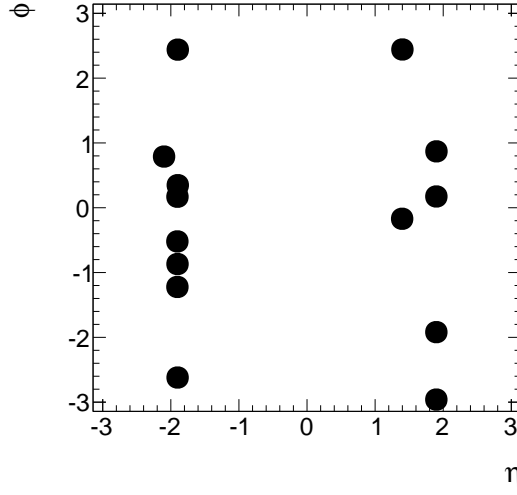
Figure 5.6: Visualisation of bad cathode strip chambers in the detector's $\phi - \eta$.

❖ Veto tracks that point towards the direction of the ECAL intermodule gap listed in Table 5.3.

❖ Veto tracks that point towards a bad CSC (visualised in Fig. 5.6).

❖ Veto tracks that point towards the region between ECAL barrel and endcap at $1.42 < |\eta| < 1.65$

These lepton and jet veto selection requirements are of course highly suppressing the background emerging from real lepton/jet production like in $W +$ jets events. The discrimination power of the lepton and jet vetos is shown in Fig. 5.7 where the minimum ΔR between the candidate track and a reconstructed electron, muon, tau or jet is shown.

Finally, two further characteristics of chargino tracks are exploited. As the chargino is produced in a very clean environment, the isolation of the track can discriminate signal against background events.

Furthermore, for charginos decaying inside the tracker there is no associated energy deposition in the calorimeters in the direction of the track. This is a very pronounced characteristics of signal tracks.

The resulting selection cuts are as follows

❖ No further substantial track activity (less than 10%) is allowed in a cone of $\Delta R < 0.3$ around the candidate track: $\sum\limits_{\Delta R < 0.3} p_{\mathrm{T}}/p_{\mathrm{T}}^{\mathrm{cand}} < 0.1$

❖ Little calorimeter energy deposits (ECAL+HCAL) in a cone of $\Delta R < 0.5$ around the track: $E_{\mathrm{calo}}^{\Delta R < 0.5} < 5\,\mathrm{GeV}$.
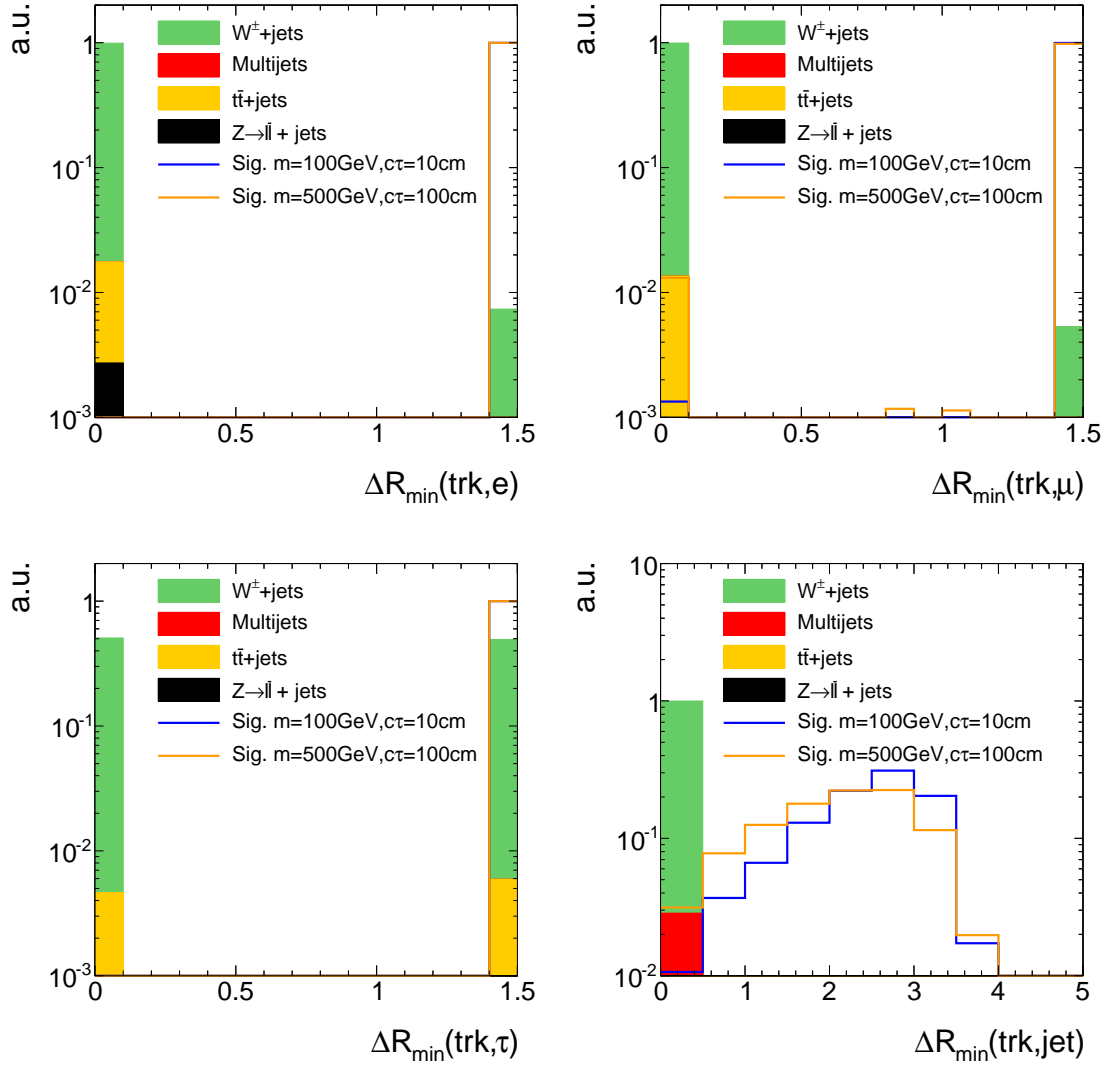
Figure 5.7: The minimum ΔR between the candidate track and a reconstructed electron (top left), muon (top right), tau (bottom left) or jet (bottom right) after the full candidate track selection cuts besides the one shown in the corresponding plot. The last bin contains all events where the candidate track has a ΔR_{min} larger than 1.5 or 5.0 to the next lepton or jet respectively.

The discrimination power of these two variables is shown in Fig. 5.8.

As emphasised before, this analysis aims at being sensitive especially on shorter lifetimes. Still, in order to allow for charginos decaying at any layer of the tracker, no explicit selection cut on the number of missing outer hits is required.

An overview over the full analysis preselection is given in Table 5.4. A summary table
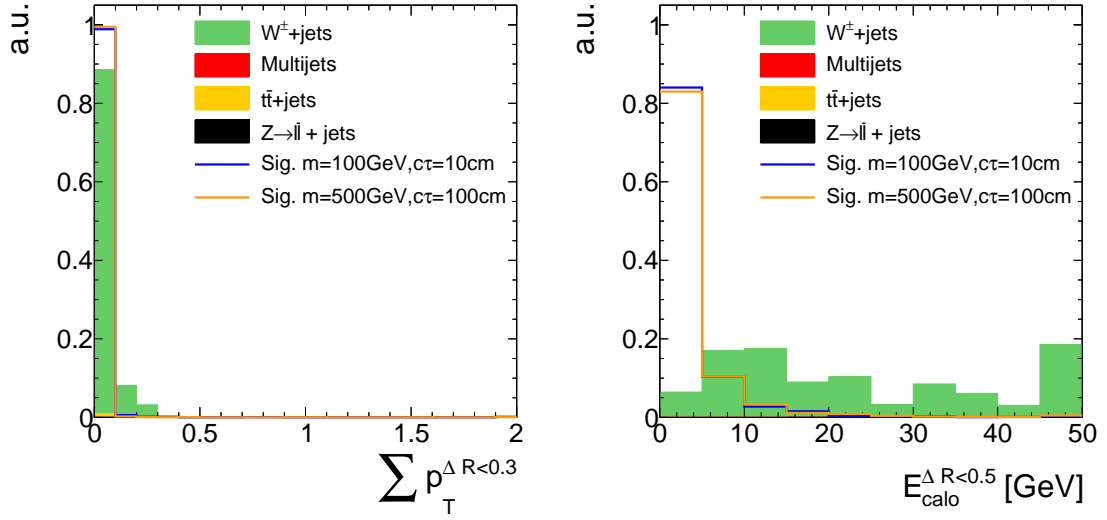
Figure 5.8: Track isolation (left) and calorimeter energy deposits (right) of the candidate track after the full previous selection.

of the event yields after each selection step for the simulated background datasets and for some of the signal models can be found in Appendix **??**.

Given the presented signal candidate selection, a set of two variables remain that are highly discriminating: The transverse momentum p_T and the energy release per path length dE/dx of the candidate track. In this analysis, the Asymmetric Smirnov discriminator I_{as} is used to enhance the discriminating power of dE/dx. See Section 3.3 for the definition and a detailed explanation of I_{as}.

In Fig. 5.9, the distribution of the remaining two variables are shown after the application of the full signal candidate selection. These variables are used to optimise the sensitivity of the search. The optimisation process will be explained in Section 7. However, before the optimisation can be accomplished, a characterisation end estimation of the background is needed. This topic will be discussed in the following section.

Table 5.4: Summary and categorisation of the analysis selection.

Trigger		HLTMonoCentralPFJet80_PFMETnoMu95_NHEF0p95
		HLTMonoCentralPFJet80_PFMETnoMu105_NHEF0p95
		HLT_MET120_HBHENoiseCleaned
Event-based selection	Trigger selection	$p_{\mathrm{T}}^{1^{\mathrm{st}}\,\mathrm{jet}} > 100\,\mathrm{GeV}$ with $\|\eta_{1.\mathrm{jet}}\| < 2.4$, $\mathrm{CHF}_{1.\mathrm{jet}} > 0.2$, $\mathrm{CEF}_{1.\mathrm{jet}} < 0.5$, $\mathrm{NHF}_{1.\mathrm{jet}} < 0.7$, $\mathrm{NEF}_{1.\mathrm{jet}} < 0.7$ $\not{E}_{\mathrm{T}} > 100\,\mathrm{GeV}$
	QCD suppression	$\Delta\phi_{\max}\left(\mathrm{jet}_i, \mathrm{jet}_j\right) < 2.7$ for all jets with $p_{\mathrm{T}} > 20\,\mathrm{GeV}$, $\|\eta\| < 4.5$ $\Delta\phi_{\max}\left(\mathrm{jet}_i, \not{E}_{\mathrm{T}}\right) > 0.5$ for two leading jets
Candidate track selection		≥ 1 track that fulfils the following criteria:
	Good quality selection	high-purity as defined in [27] $N_{\mathrm{miss}}^{\mathrm{middle/inner}} = 0$ $\|d0\| < 0.02\,\mathrm{cm}$ $\|dz\| < 0.5\,\mathrm{cm}$
	Kinematic selection	$\|\eta\| < 2.1$ $p_{\mathrm{T}} > 10\,\mathrm{GeV}$
	Lepton/jet veto	No muon within $\Delta R < 0.15$ No electron within $\Delta R < 0.15$ No tau within $\Delta R < 0.15$ No jet within $\Delta R < 0.5$ No dead/noisy ECAL cell within $\Delta R < 0.05$ Not within an ECAL intermodule gap Not within $1.42 < \|\eta\| < 1.65$ Not within $\Delta R < 0.25$ to a bad CSC
	Isolation selection	$\sum_{\Delta R < 0.3} p_{\mathrm{T}}/p_{\mathrm{T}}^{\mathrm{cand}} < 0.1$ $E_{\mathrm{calo}}^{\Delta R < 0.5} < 5\,\mathrm{GeV}$
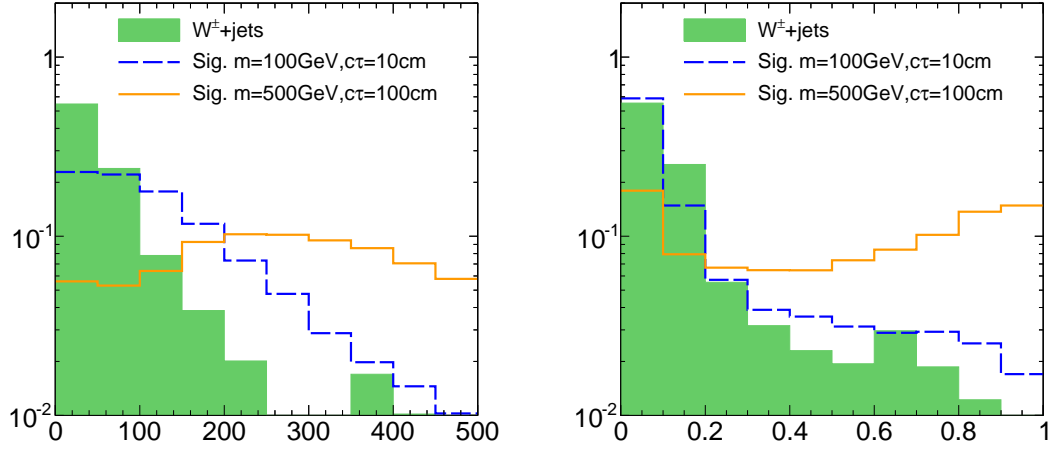
Figure 5.9: Candidate track p_T (left) and I_{as} (right) after the full signal candidate selection for signal and $W + \text{jets}$ events. Because of the low statistical precision of the $W + \text{jets}$ sample, the trigger requirements are not applied. This does not influence the shape of the distributions since $\not{E}_T$ and $p_T^{1\text{st jet}}$ are not expected to be correlated with the track characteristics.

6 Characterisation and estimation of the Standard Model backgrounds

After the application of the signal candidate selection, explained in the previous section, the background arising from Standard Model processes is dramatically reduced. Only two events in the simulated $W + \text{jets}$ sample remain. One of these originates from an unreconstructed muon, the other one from an unreconstructed electron. This implies, that the electron, muon, and tau vetos cannot reject all leptons because some are not properly reconstructed. Due to the limited size of the simulated $W + \text{jets}$ dataset (15 times smaller than the number of events expected from $W + \text{jets}$ processes during 2012 data taking), it is not possible to rely on a full simulation-based estimation of the leptonic background. The underlying mechanism of the non-reconstruction of a lepton and the corresponding methods to estimate the leptonic background will be explained in detail in Section 6.2.

Furthermore, there is the possibility that a track is reconstructed out of a set of hits

that do not origin from only one single particle. Such tracks are called "fake tracks". Background tracks arising from a combination of unrelated hits will be explained in the following Section 6.1. It should be noted that the fake background is contributing through all SM processes, not only via W + jets. Still, as the characteristics of fake tracks are independent of the underlying process, this background can also be studied on simulation using W + jets events only.

6.1 Fake background

Fake tracks are tracks that are not reconstructed out of the trajectory of one single particle. The rate at which this wrong reconstruction occurs is highly restrained by the quality cuts on χ^2 and the vertex compatibility of the track reconstruction algorithm. Details on the reconstruction algorithm of tracks at CMS can be found in Section **??**.

The probability of reconstructing a fake track is strongly correlated with the number of hits in the tracker system. This can be seen in Fig. 6.1, where the normalised distribution of the number of hits from fake tracks is depicted. There are almost no fakes with a number of hits larger than seven. In simulation, fake tracks are defined as tracks that cannot be matched to a generator-level particle within a distance of $\Delta R < 0.01$.

Fakes are efficiently suppressed by the requirements of no missing middle or inner hits and the compatibility with the primary vertex. Unfortunately, wrongly reconstructed tracks which pass these criteria, do also easily pass the $E_{\mathrm{calo}}^{\Delta R<0.5} < 5\,\mathrm{GeV}$ requirement
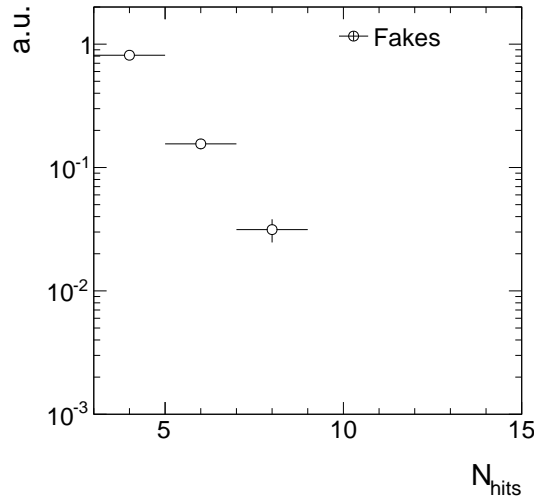

Figure 6.1: Normalised distribution of the number of hits for fake tracks after the signal candidate selection from Table 5.4. To increase the statistical precision, only track selection requirements are applied.

732   with high efficiency.

733

734   In this analysis, the estimation of the fake background is split into two parts. First, the
735   background is determined inclusively in dE/dx. Second, the dE/dx (I_{as}) distribution is
736   estimated with the help of a fake enriched control region. This second step is needed to
737   enable an optimisation in dE/dx (see Section 7).

6.1.1 Inclusive fake background estimation

739   The inclusive background estimation closely follows the background estimation method
740   done in [36, 37]. It aims at determining the probability of having a fake track in an event
741   that passes the full signal candidate selection (Table 5.4) plus a potential additional p_{T}
742   selection cut that is determined in an optimisation procedure (Section 7). This probability
743   will be called the fake rate ρ_{fake}.

744   The inclusive fake background is estimated with the help of $Z \rightarrow \mu\bar{\mu}$ and $Z \rightarrow e\bar{e}$
745   events from data. $Z \rightarrow \ell\bar{\ell}$ events can be selected with high purity by requiring two well
746   reconstructed muons or electrons that are opposite in charge and for which the invariant
747   mass is around the Z-boson mass of $\sim 90\,\mathrm{GeV}$. As these events do not contain further
748   leptons from the hard interaction, any additional track is either an ISR jet, a soft particle
749   from the underlying event or is a fake, reconstructed out of a combination of several
750   soft particles. Since the track-based signal candidate selection requires a track with a
751    $p_{\mathrm{T}} > 20\,\mathrm{GeV}$ that is no lepton or jet, it suppresses ISR jets and soft tracks from the
752   underlying event. Thus, applying the track-based signal candidate selection on $Z \rightarrow \ell\bar{\ell}$
753   events selects fake tracks with high purity.

754   The selection of two well reconstructed muons and electrons is done with the single-
755   muon and single-electron datasets listed in Table 6.1. For the $Z \rightarrow \mu\bar{\mu}$ selection, an event
756   is required to have two muons with $p_{\mathrm{T}} > 25\,\mathrm{GeV}$ and $|\eta| < 2.4$. To suppress background
757   from cosmic muons, the distance from the primary vertex must be less than $|d0| < 0.2\,\mathrm{cm}$
758   in radial and $|dz| < 0.5\,\mathrm{cm}$ in longitudinal direction. In order to suppress background
759   arising from jets that fake muons, various quality criteria are applied: it is required that
760   there is at least one hit in the muon detector that is considered in the global muon fit, and
761   that at least two measurements are from different muon detector stations. Concerning the
762   track of the muon in the tracker system, at minimum one hit in the pixel tracker and at
763   least six hits in the full tracker system are required. An isolation criterion is applied that
764   requires the sum of transverse momenta of all particle-flow particles in a cone of $\Delta R < 0.4$
765   around the muon to be less than 12%. Finally, the muons are required to be opposite in
766   charge and to have an invariant mass between $80 - 100\,\mathrm{GeV}$. The $Z \rightarrow \mu\bar{\mu}$ + fake track
767   selection is summarised in Table 6.2.

768   In order to select $Z \rightarrow e\bar{e}$ events in data, the two electrons are required to have

Table 6.1: Datasets used for the determination of the fake rate.

Dataset	Luminosity $[\,\mathrm{fb}^{-1}\,]$
/SingleMu/Run2012A-22Jan2013-v1/AOD	0.876
/SingleMu/Run2012B-22Jan2013-v1/AOD	4.405
/SingleMu/Run2012C-22Jan2013-v1/AOD	7.040
/SingleMu/Run2012D-22Jan2013-v1/AOD	7.369
/SingleElectron/Run2012A-22Jan2013-v1/AOD	0.876
/SingleElectron/Run2012B-22Jan2013-v1/AOD	4.412
/SingleElectron/Run2012C-22Jan2013-v1/AOD	7.050
/SingleElectron/Run2012D-22Jan2013-v1/AOD	7.368

$p_\mathrm{T} > 25\,\mathrm{GeV}$, $|\eta| < 2.5$ and no missing hits in the inner layers of the tracker. Furthermore, the electrons need to pass a conversion veto as described in [41] in order to reduce background arising from photon conversions. An isolation requirement similar to the muon isolation criterion is applied with an increased threshold of 15%. The electron identification is further based on a multivariate technique developed within [42] that exploits electron characteristics about the track quality, the ECAL cluster shapes, and the combination of the measurements in the tracker and in the ECAL. Again, the two electrons must be opposite in charge and their invariant mass must be between $80 - 100\,\mathrm{GeV}$. A summary of the $Z \to e\bar{e} +$ fake track event selection can be found in Table 6.3.

When applying a $Z \to \ell\bar{\ell}$ selection plus the candidate track selection, the selected track should be a fake. If this is indeed the case can be tested on simulated $Z \to \ell\bar{\ell}$ events. As can be seen in Fig. 6.2, a reasonable purity in fake tracks can be achieved by applying the candidate track selection on top of the $Z \to \ell\bar{\ell}$ selection. In simulated $Z \to \mu\bar{\mu}$ events, a purity of 88%, whereas in simulated $Z \to e\bar{e}$ events a purity of 92% of fake tracks can be achieved.

As already mentioned, the fake rate is defined as the probability that an event contains a fake track that fulfils the candidate track selection. Thus, for the $Z \to \ell\bar{\ell}$ datasets it is defined as the number of events passing the full selection described in Table 6.2 (Table 6.3) divided by the number of events that pass only the event-based selection in

Table 6.2: Event selection cuts for the $Z \to \mu\bar{\mu}$ + fake control sample to estimate the inclusive fake background.

Event-based selection	Two global muons with $p_\mathrm{T} > 25\,\mathrm{GeV}$
	$\lvert\eta\rvert < 2.4$
	$\sum_{\Delta R < 0.4} p_\mathrm{T}^\mathrm{PF\ particle} / p_\mathrm{T}(\mu) < 0.12$
	$\left.\frac{\chi^2}{ndof}\right\rvert_\mathrm{global\ track} < 10$
	$\lvert d0 \rvert < 0.2\,\mathrm{cm}$
	$\lvert dz \rvert < 0.5\,\mathrm{cm}$
	≥ 1 hit in the muon detector considered in global fit
	≥ 2 hits in different muon stations
	≥ 1 hit in the pixel detector
	≥ 6 hits in the tracker system
	Muons opposite in charge
	$80\,\mathrm{GeV} < M_\mathrm{inv}\left(\mu_1, \mu_2\right) < 100\,\mathrm{GeV}$
Candidate track selection	Good quality selection
	Kinematic selection
	Lepton/jet veto
	Isolation selection

Table 6.2 (Table 6.3)

$$\rho_\mathrm{fake} = \frac{N_{Z \to ll}^\mathrm{cand\ trk\ selection}}{N_{Z \to ll}}$$

Fake rates are determined independently for the $Z \to \mu\bar{\mu}$ + fake and $Z \to e\bar{e}$ + fake event selection and then averaged to obtain the final fake rate. The fake rate with the candidate track selection given in Table 5.4 is $(6.86 \pm 0.25) \cdot 10^{-5}$. This is not the final result as the optimisation in p_T will add an additional p_T selection cut to the candidate track selection.

Within [36,37], it was checked that the fake rate is constant for different processes. This is shown in Fig. 6.3 where the fake rate is depicted for the most important SM processes. Since the fake rate is constant for different SM processes, the fake rate determined on the $Z \to \ell\bar{\ell}$ dataset can be generalised for all SM background possibly contributing to this

Table 6.3: Event selection cuts for the $Z \to e\bar{e}$ + fake control sample to estimate the inclusive fake background.

Event-based selection	Two Electrons with	$p_T > 25\,\text{GeV}$
		$\lvert\eta\rvert < 2.5$
		$\sum\limits_{\Delta R < 0.4} p_T^{\text{PF particle}}/p_T(e) < 0.15$
		pass conversion veto [41]
		no missing inner tracker hits
		good MVA electron as defined in [42]
	Electrons opposite in charge	
	$80\,\text{GeV} < M_{\text{inv}}\,(e_1, e_2) < 100\,\text{GeV}$	
Candidate track selection	Good quality selection	
	Kinematic selection	
	Lepton/jet veto	
	Isolation selection	

search. Thus, the inclusive fake background can be estimated by multiplying the fake rate with the number of events selected from the MET dataset (Table 5.2) by applying the event-based signal candidate requirements from Table 5.4.

$$N_{\text{bkg}}^{\text{fake, inclusive in } I_{\text{as}}} = \rho_{\text{fake}} \cdot N_{\text{event-based selection}}^{\text{MET}}.$$

Given the number of events after the event-based selection of $N_{\text{event-based selection}}^{\text{MET}} = 1.38 \cdot 10^6$ and the fake rate cited above, the inclusive fake background can be estimated to 94.7 ± 3.4 for the candidate track selection.

It should be noted again that the inclusive fake background estimation will be only inclusive in I_{as} not in p_T. That means that after the definition of the signal region, $N_{\text{bkg}}^{\text{fake, inclusive in } I_{\text{as}}}$ is determined with the additional optimal p_T selection.

Possible differences between the fake rate in $Z \to \ell\bar{\ell}$ events and other SM processes are estimated on simulated events and taken into account as a systematic uncertainty (see Section 6.4.1).
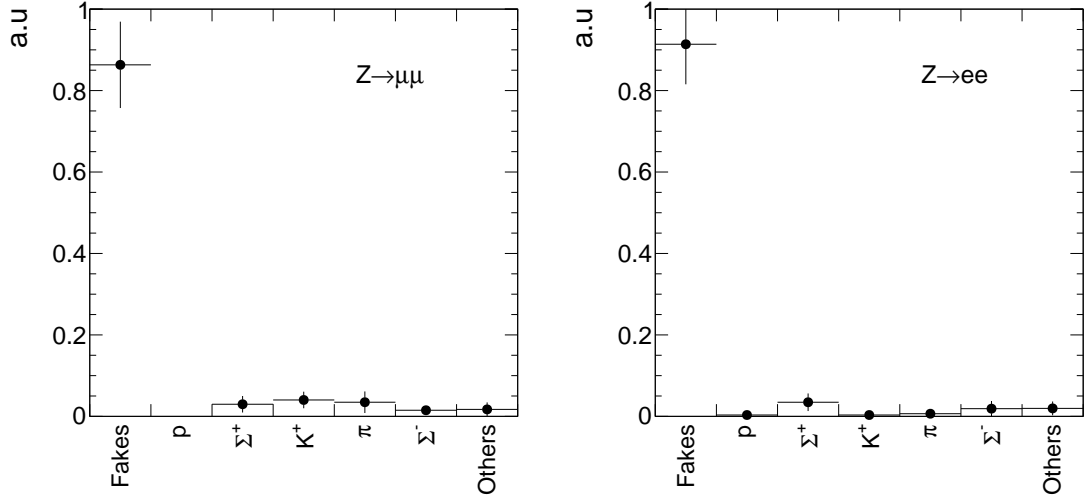
Figure 6.2: Corresponding generator-level particles of all tracks within $Z \to \ell\bar{\ell}$ + fake that were selected according to the candidate track selection. The full selection for tracks in $Z \to \mu\bar{\mu}$ events (left) is given in Table 6.2. The full selection for tracks in $Z \to e\bar{e}$ events (right) is given in Table 6.3. "Fake" means that no corresponding generator-level particle is found.
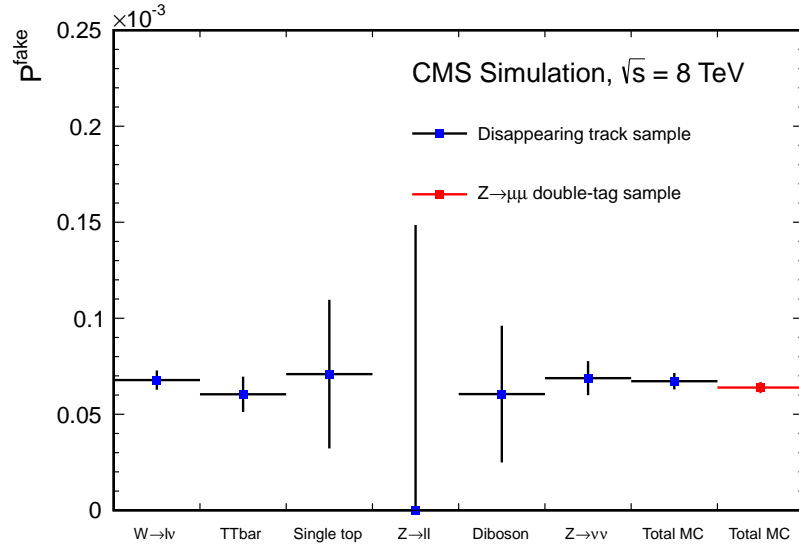
Figure 6.3: Fake track rate estimated in [36, 37] for tracks with four hits. Taken from [37]

6.1.2 dE/dx shape of fake background

The information about the energy release per path length for fake tracks should not be taken from simulated samples as the simulation of dE/dx is not reliable (cf. Fig. 3.8). Within this analysis the Asymmetric Smirnov discriminator I_{as} is used to discriminate signal against background with respect to dE/dx (see Section 3.3). In order to estimate the I_{as} shape of fake tracks, a control region $\mathrm{CR}_{I_{\mathrm{as}}}^{\mathrm{fake}}$ is defined that is enriched with fakes and shows the same I_{as} distribution as fake tracks in the signal region.

To enrich fake tracks, it is possible to invert the selection cuts on the number of missing middle and inner hits, i.e. requiring at least one missing inner or middle hit $\left(N_{\mathrm{miss}}^{\mathrm{inner}} + N_{\mathrm{miss}}^{\mathrm{middle}} > 0\right)$. Figure 6.4 shows the distribution of the number of missing inner plus missing middle hits for fake and leptonic tracks in simulated $W + \mathrm{jets}$ events. It can be seen that the enrichment of fakes by this selection works. The resulting purity of fakes in $\mathrm{CR}_{I_{\mathrm{as}}}^{\mathrm{fake}}$ is about 98% (see Fig. 6.5).

Additionally, it must be checked whether the I_{as} shape in $\mathrm{CR}_{I_{\mathrm{as}}}^{\mathrm{fake}}$ is comparable to the I_{as} shape in the signal region. As the exact definition of the signal region will be addressed during optimisation, this test is done for various p_{T} selection cuts.

The comparison of the I_{as} shape of fake tracks can only be done on simulation. Thus, simulated $W + \mathrm{jets}$ events are used to select fake tracks in both regions. A comparison of the shape for the candidate track selection and the $\mathrm{CR}_{I_{\mathrm{as}}}^{\mathrm{fake}}$ is shown in Fig. 6.5.

The I_{as} shape is almost identical in the signal and in the control region which makes the
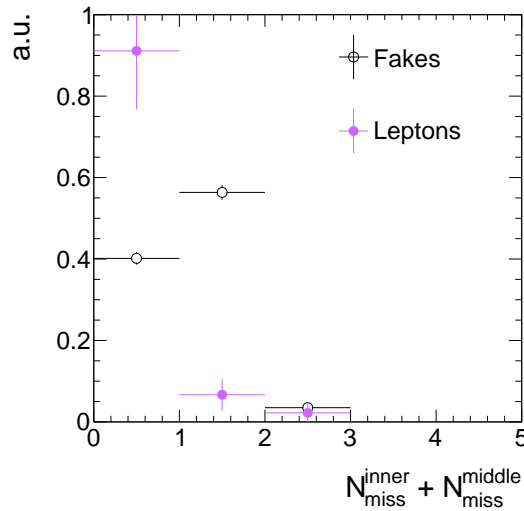

Figure 6.4: Normalised number of missing inner plus missing middle hits for fake and leptonic tracks for the full candidate track selection with the selection requirements on $N_{\mathrm{miss}}^{\mathrm{inner}}$ and $N_{\mathrm{miss}}^{\mathrm{middle}}$ removed. Trigger requirements and QCD suppression cuts were removed to enhance the statistical precision.
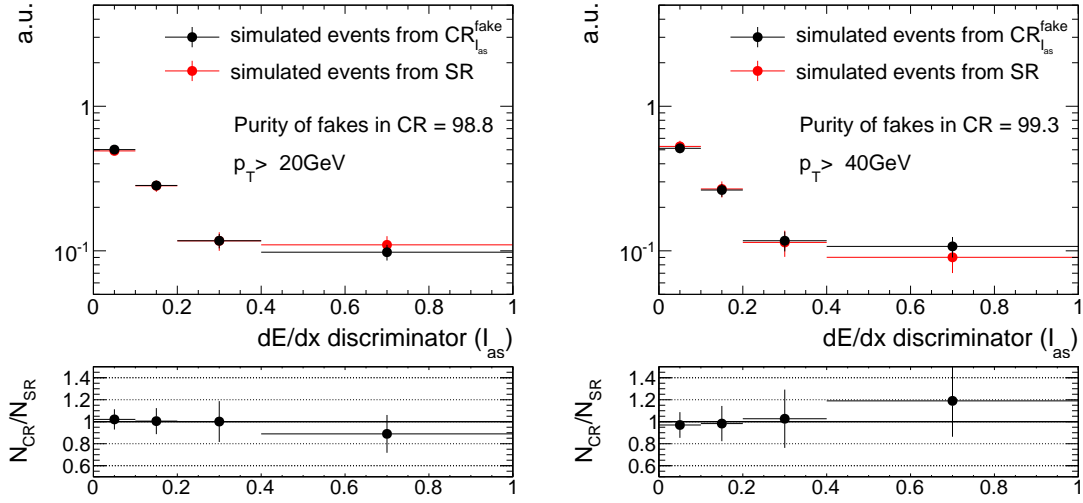
Figure 6.5: Comparison of the I_{as} shape between $CR_{I_{as}}^{fake}$ and the signal region for two different track p_T selections of $p_T > 20\,GeV$ (left) and $p_T > 40\,GeV$ (right). To enhance the statistical precision only the track-based selection is applied.

definition of the control region perfectly suited for estimating the I_{as} shape from $CR_{I_{as}}^{fake}$ in data. The remaining shape differences are taken into account as a systematic uncertainty (discussed in Section 6.4.2).

6.2 Leptonic background

The leptonic background of the here presented search is caused by non-reconstructed leptons that circumvent the lepton veto selection. However, at least non-reconstructed electrons or taus should in principle deposit enough energy in the calorimeters such that they can still be vetoed by the calorimeter isolation requirement $E_{calo}^{\Delta R<0.5} < 5\,GeV$. As muons don't deposit much energy in the calorimeters, this reasoning does not apply to them. In the following, the sources of the three different leptonic backgrounds are characterised.

Electrons

To reject unreconstructed electrons, all tracks pointing to a dead or noisy ECAL cell, to an ECAL intermodule gap, or to the region between ECAL barrel and endcap at $1.42 < |\eta| < 1.65$ are vetoed, as described in Section 5.2. By this selection, almost all electrons are efficiently rejected. In the simulated W+jets sample only one simulated event remains that passes all signal candidate selection criteria and for which the candidate track can be matched to a generator-level electron. This event is visualised in Fig. 6.6.

In this event no energy deposits in the ECAL are read out, which suggests that the

Figure 6.6: Visualisation of a $W \to e\nu_e$ event contributing to the SM background. In light blue, generator-level particles including e and ν_e of the W-boson decay are shown. The neutrino, only weakly interacting does not show any signature in the detector, whereas the electron ($p_\mathrm{T} \simeq 90\,\mathrm{GeV}$) leaves a track (black line) with $p_\mathrm{T} \simeq 70\,\mathrm{GeV}$ in the tracker. No ECAL energy deposits in the direction of the electron are visible. This is caused by the fact that the corresponding ECAL energy deposits were not read out in this event. An ISR jet ($p_\mathrm{T} \simeq 230\,\mathrm{GeV}$) causes the $\not{E}_\mathrm{T}$ (read arrow) in the event.

corresponding ECAL tower was not working properly in 2012. Additionally, electrons can do bremsstrahlung which can change the direction of the electron significantly. Thus, the energy deposits in the ECAL can possibly not be matched to the original electron.

Taus

Taus are contributing to the leptonic background through the hadronic decay of a tau lepton to one charged pion $\tau \to \pi^{\pm}\nu_\tau$. Other decay modes of the tau lepton are suppressed by the track isolation criterion. Taus fail reconstruction if they don't deposit energy in the HCAL or ECAL. Unreconstructed taus can therefore also easily bypass the calorimeter isolation criterion. Because of nuclear interactions in the tracker, pions often result in short reconstructed tracks that can easily be highly mismeasured in p_T. Thus, taus can contribute to the background even if imposing a tight selection in the transverse momentum. Such an event is shown in Fig. 6.7.
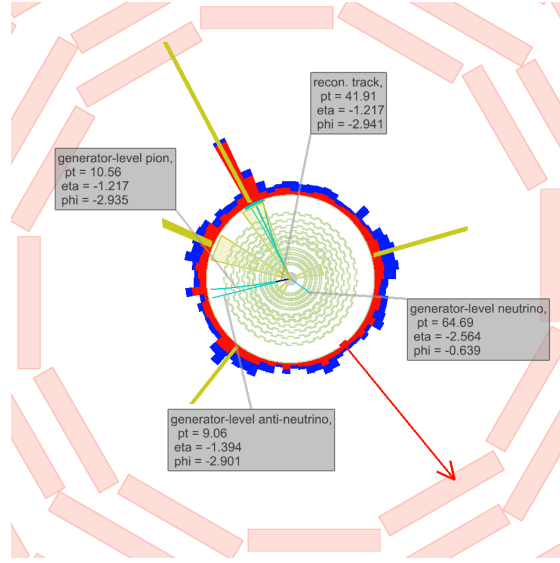
Figure 6.7: Visualisation of a $W^+ \to \tau^+ \nu_\tau \to \pi^+ \bar{\nu}_\tau \nu_\tau$ event contributing to the SM background. In light blue, the generator-level particles including π^+, $\bar{\nu}_\tau$ and ν_τ are shown. The transverse momentum of the generator-level pion is only $p_T \sim 10\,\text{GeV}$, but because the reconstructed track (black line) is very short, it leads to a high mismeasurement of the track p_T of $\sim 40\,\text{GeV}$. The shortness of the track is caused by nuclear interactions of the pion. As no corresponding ECAL or HCAL energy deposits are measured, the reconstruction of the pion fails. The ISR jet causes the $\not{E}_T$ (read arrow) in the event.

Muons

Muons can fail reconstruction if they point towards a bad cathode strip chamber. This is taken into account in the candidate track selection. However, some of the muons still fail reconstruction if they fall within the gap between stations 0 and 1 of the drift tube system at $|\eta| = 0.25$. The muon reconstruction efficiency drops from around 99% to a value of around 94% as shown in [36, 37]. This possibility is illustrated in a simulated event shown in Fig. 6.8.

In [36, 37] events are rejected if the track is pointing in a region of $0.15 < |\eta| < 0.35$. In this search, this cut was omitted to maximise signal acceptance. Due to the additional selection in I_{as}, muons can be efficiently suppressed. E.g. in the event shown in Fig. 6.8, the muon has an I_{as} value of about 0.007.

In general, all leptons are minimally ionising. However, as electrons are much lighter compared to muons or pions, they loose more energy also via radiative effects. Still, all three lepton types loose much less energy compared to hypothetical new heavy particles. To have the possibility to make an optimisation in the two main discriminating variables
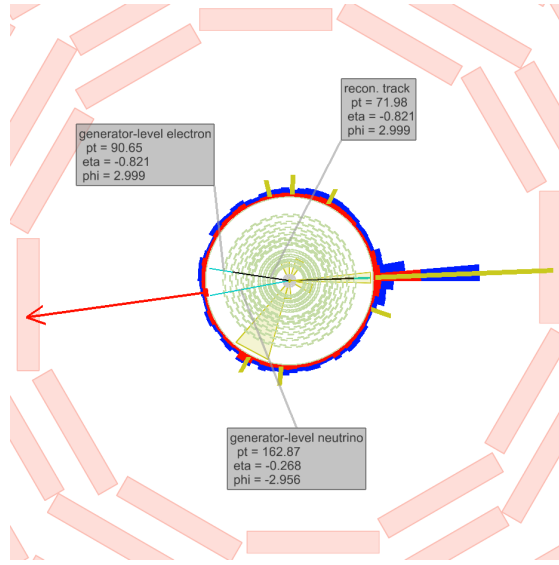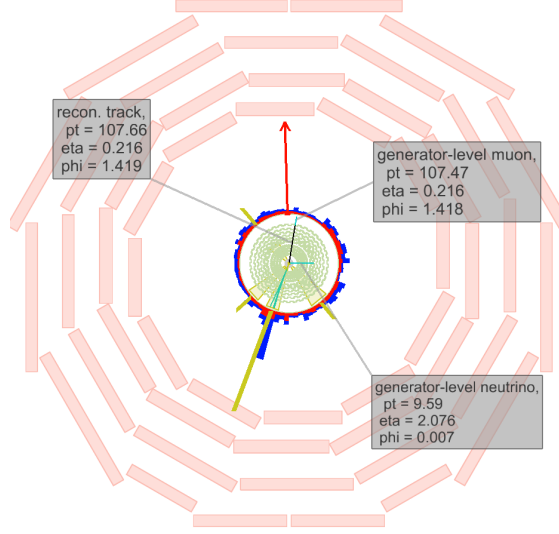
Figure 6.8: Visualisation of an $W \to \mu\nu_\mu$ event contributing to the SM background. In light blue, the generator-level particles including μ and ν_μ of the W decay are shown. The muon is pointing to the η-region between stations 0 and 1 of the DT system at $|\eta| \sim 0.25$. In this region the muon reconstruction is less efficient. No signal in the muon chambers is visible. Therefore the muon could not be reconstructed. The ISR jet causes the $\not{E}_T$ (read arrow) in the event.

p_T and I_{as}, the background estimation methods are designed to work for all different p_T and I_{as} selection cuts.

As for the fakes, the leptonic background estimation is splitted into two parts. First, the estimation of the inclusive background without I_{as} information. Second, the estimation of the I_{as} shape for all three leptonic background sources.

6.2.1 Inclusive leptonic background estimation

The inclusive (without dE/dx information) lepton background estimation method is similar to the background estimation method used in [36, 37].

In order to estimate the number of events in the signal region originating from unreconstructed leptons, information from simulated events is used. With the help of simulated $W +$ jets events, the ratio $\rho_{MC}^{lep_i}$ between the number of events in the signal region with the selected track matched to a generator-level lepton $N_{SR}^{\text{trk matched to lepton}_i}$ and the number of events in a control region $N_{CR}^{\text{lepton}_i \text{ veto inverted}}$ with a inverted lepton veto is determined.

890   For muons, this lead to the following expression

$$\rho_{\mathrm{MC}}^{\mu} = \frac{N_{\mathrm{SR,MC}}^{\mathrm{trk\ matched\ to\ }\mu}}{N_{\mathrm{CR,MC}}^{\mu\ \mathrm{veto\ inverted}}}.$$

891   Since for electrons and taus the reconstruction efficiency is highly correlated with the
892    $E_{\mathrm{calo}}^{\Delta R < 0.5}$ selection requirement, the $E_{\mathrm{calo}}^{\Delta R < 0.5}$ requirement is additionally removed in the
893   control regions for these two lepton types

$$\rho_{\mathrm{MC}}^{e,\tau} = \frac{N_{\mathrm{SR,MC}}^{\mathrm{trk\ matched\ to\ }e,\tau}}{N_{\mathrm{CR,MC}}^{e,\tau\ \mathrm{veto\ inverted}, \cancel{E_{\mathrm{calo}}^{\Delta R < 0.5} < 5\,\mathrm{GeV}}}}.$$

894   In order to estimate the inclusive background for all three lepton types, the scaling
895   factor $\rho_{\mathrm{MC}}^{\mathrm{lep}_i}$ is applied to the number of events in the lepton veto inverted control region
896   measured in data. Also in data the control region for electrons and taus is defined with
897   the $E_{\mathrm{calo}}^{\Delta R < 0.5}$ requirement removed. Thus, the inclusive number of predicted background
898   events can be estimated with

$$N_{\mathrm{bkg}}^{\mu,\ \mathrm{inclusive\ in\ I_{as}}} = \rho_{\mathrm{MC}}^{\mu} \cdot N_{\mathrm{CR,data}}^{\mu\ \mathrm{veto\ inverted}}.$$

899   for muons, and

$$N_{\mathrm{bkg}}^{e,\tau,\ \mathrm{inclusive\ in\ I_{as}}} = \rho_{\mathrm{MC}}^{e,\tau} \cdot N_{\mathrm{CR,data}}^{e,\tau\ \mathrm{veto\ inverted}, \cancel{E_{\mathrm{calo}}^{\Delta R < 0.5} < 5\,\mathrm{GeV}}}.$$

900   for electrons and taus.

901   This method relies on the simulation of the lepton reconstruction efficiencies which is
902   expected to be reasonably accurate [43–45]. For electrons and taus the simulation of the
903   calorimeter isolation is utilised as well. Possible discrepancies between simulation and
904   data are taken into account as a systematic uncertainty via a comparison of the lepton
905   reconstruction efficiencies in data and simulation in $Z \to \ell\bar{\ell}$ events (see Section 6.4.3).

906   To reduce the statistical uncertainty, the scale factor is calculated without applying the
907   QCD suppression cuts. After the signal candidate selection described in Section 5.2, only
908   one event remains in the simulated W + jets sample where the candidate track can be
909   matched to an electron. There are five track candidates that can be matched to a muon,
910   and zero selected tracks that can be matched to a pion. The statistical uncertainties
911   are calculated as the 68% upper and lower limits on the inclusive background with the
912   Neyman procedure [20, 46]. Table 6.4 gives the result for the prediction of the inclusive
913   leptonic background for the signal candidate selection from Section 5.2.

Table 6.4: Scaling factor $\rho_{\mathrm{MC}}^{\mathrm{lep}_i}$, number of events in the data control region $N_{\mathrm{CR,data}}$ and the resulting inclusive estimation $N_{\mathrm{predicted}}$ after the candidate track selection.

	scaling factor $\rho_{\mathrm{MC}}^{\mathrm{lep}_i}$	$N_{\mathrm{CR,data}}$	$N_{\mathrm{predicted}}$
electrons	$1.25^{+1.70}_{-0.77} \cdot 10^{-4}$	60067	$7.49^{+10.19}_{-4.63}$
muons	$2.17^{+1.65}_{-0.93} \cdot 10^{-4}$	76664	$16.64^{+12.64}_{-7.12}$
taus	$< 2.13 \cdot 10^{-2}$	445	< 9.46

6.2.2 dE/dx shape of leptonic background

In order to get information about the I_{as} (see Section 3.3) shape in the signal region of electrons, muons and taus, a control region must be found where the shape of the observable is at least similar to that in the signal region. The most natural control region, being the lepton veto inverted control region, cannot be used because the variable I_{as} is highly correlated to the lepton reconstruction efficiency, as can be seen in Fig. 6.9. The discrepancies reach factors up to an order of magnitude.

Various other control regions were tested and could not be used because of too large I_{as} shape differences to the signal region.

As no suitable control region exists where the I_{as} shape of the leptons is at least similar to the shape in the signal region, it is decided to use the I_{as} information from simulation. This introduces a large systematic uncertainty since dE/dx (and therefore I_{as}) is not
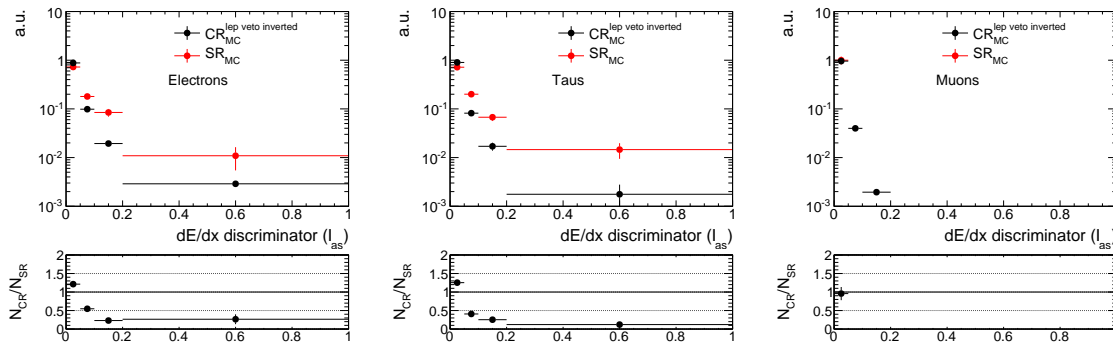

Figure 6.9: Normalised I_{as} distribution for electrons (left), pions from the tau decay (middle) and muons (right) in the signal region (red) and the lepton veto inverted control region (black).
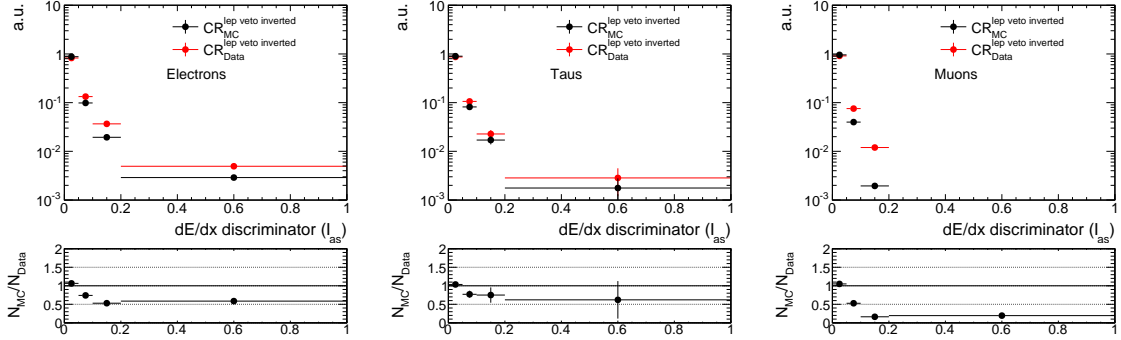
Figure 6.10: Normalised I_{as} distribution for electrons (left), pions from the tau decay (middle) and muons (right) in the lepton veto inverted control region from simulated (black) and real (red) events.

simulated well. However, the corresponding systematic uncertainty is still smaller than taking the I_{as} shape from a control region in data: compare Fig. 6.9 and Fig. 6.10.

In order to take into account the bias when using I_{as} from simulation, a systematic uncertainty is estimated that addresses simulation-data differences of the I_{as} distributions. This systematic uncertainty is discussed in Section 6.4.4.

6.3 Background estimation validation

The background estimation methods are exhaustively validated with the help of signal depleted control regions. Various control regions are used for validation. For each control region it has been checked that the signal contamination is less than the statistical uncertainty of the background prediction. For some of the models the expected number of events exceeds this limit. However, these models are already ruled out by the search for disappearing tracks [11] (see Appendix **??**).

First, to validate the estimation method of the leptonic background, a leptonic control region is defined by selecting only tracks with a minimum number of seven hits in the tracker. This reduces the fake contribution to a minimum (cf. Fig. 6.1). Additionally in order to minimise signal contamination, the calorimeter isolation requirement is inverted to $E_{\text{calo}}^{\Delta R < 0.5} > 10\,\text{GeV}$.

The validation test for the control region with $E_{\text{calo}}^{\Delta R < 0.5} > 10\,\text{GeV}$ and $N_{\text{hits}} > 6$ is shown in Table 6.5. The predicted number of events by the leptonic background estimation is compatible with the observed data yield.

As the fake background can only be estimated within the low calorimeter isolation region $\left(E_{\text{calo}}^{\Delta R < 0.5} < 10\,\text{GeV} \right)$ to ensure high fake purity, the information about the num-

Table 6.5: Validation test of leptonic background estimation. Left: $E_{\mathrm{calo}}^{\Delta R<0.5} > 10\,\mathrm{GeV}$ and $N_{\mathrm{hits}} > 6$. Right: $E_{\mathrm{calo}}^{\Delta R<0.5} > 10\,\mathrm{GeV}$, $N_{\mathrm{hits}} > 6$ and $I_{\mathrm{as}} > 0.2$. Only statistical uncertainties are included.

	Predicted Yield	Data Yield
Total bkg	$131.70^{+26.30}_{-18.42}$	156
Electrons	$14.67^{+11.16}_{-6.29}$	
Muons	$7.99^{+10.90}_{-5.00}$	
Taus	$109.04^{+21.18}_{-16.58}$	

	Predicted Yield	Data Yield
Total bkg	$0.0^{+0.50}_{-0.0}$	1
Electrons	$0.0^{+0.07}_{-0.0}$	
Muons	$0.0^{+0.32}_{-0.0}$	
Taus	$0.0^{+0.38}_{-0.0}$	

ber of fake tracks in the high calorimeter isolation region is taken from the fake enriched control region $\mathrm{CR}_{I_{\mathrm{as}}}^{\mathrm{fake}}$ defined in Section 6.1. In this control region, the ratio of $N_{E_{\mathrm{calo}}^{\Delta R<0.5}>10\,\mathrm{GeV}}/N_{E_{\mathrm{calo}}^{\Delta R<0.5}<10\,\mathrm{GeV}}$ is estimated and taken as a multiplicand to the number of events predicted from the $E_{\mathrm{calo}}^{\Delta R<0.5} < 10\,\mathrm{GeV}$ region. In Table 6.6, two different validation tests are shown, once an inclusive validation in I_{as} and once with an I_{as} selection of 0.2. Again, the predicted background events is in agreement with the number of observed events.

The whole validation is done for different selections in p_{T} and I_{as}. All validation tests

Table 6.6: Validation test of fake and leptonic background estimation methods. Left: $E_{\mathrm{calo}}^{\Delta R<0.5} > 10\,\mathrm{GeV}$. Right: $E_{\mathrm{calo}}^{\Delta R<0.5} > 10\,\mathrm{GeV}$ and $I_{\mathrm{as}} > 0.2$. Only statistical uncertainties are included.

	Predicted Yield	Data Yield
Total bkg	$309.00^{+33.46}_{-26.62}$	324
Electrons	$59.92^{+16.11}_{-11.85}$	
Muons	$8.04^{+10.97}_{-5.03}$	
Taus	$173.06^{+24.62}_{-20.23}$	
Fakes	$67.98^{+11.57}_{-11.57}$	

	Predicted Yield	Data Yield
Total bkg	$14.80^{+2.92}_{-2.85}$	16
Electrons	$0.75^{+0.36}_{-0.25}$	
Muons	$0.00^{+0.32}_{-0.00}$	
Taus	$2.33^{+0.74}_{-0.55}$	
Fakes	$11.72^{+2.79}_{-2.79}$	

show good agreement. A variety of validation tests with different p_T and I_as selections can be found in Appendix **??**.

Still, systematic uncertainties need to be estimated. The sources of systematic uncertainties and how they are estimated will be explained in the following section.

6.4 Systematic uncertainties

Systematic uncertainties on the background estimation include:

- the uncertainty on the fake rate ρ_fake;

- the uncertainty on the I_as shape of fake tracks predicted from a control region;

- the uncertainty on the leptonic scale factor $\rho_\mathrm{MC}^{\mathrm{lep}_i}$ determined with simulated events;

- the uncertainty on the I_as shape of the leptonic background.

6.4.1 Uncertainty on the fake rate

The fake rate ρ_fake is determined with the help of observed $Z \to \ell\bar\ell$ events. To estimate the uncertainty on this fake rate caused by differences in the fake rate between different underlying processes, a comparison between the fake rate in simulated $Z \to \ell\bar\ell$ + jets and simulated W + jets events is done. The fake rate in the $Z \to \ell\bar\ell$ + fake track control samples (see Tables 6.2 and 6.3) and the fake rate in the signal candidate selection from Table 5.4 in W + jets events are compared.

Unfortunately, the statistical precision of the simulated W+jets dataset is limited. Thus, the estimation of the systematic uncertainty is mainly driven by statistical uncertainties. In order to enhance the statistical precision of the estimation, the selection requirements on $\not{E}_\mathrm{T}$ and $p_\mathrm{T}^{\mathrm{1^{st}\,jet}}$ are loosened and the QCD suppression requirements are removed. As these variables are not expected to be correlated with the fake rate, the relative uncertainty of the fake rate should stay the same. That this is indeed the case, can be seen in Table 6.7.

The systematic uncertainty is estimated as the 1-sigma deviation of the ratio $\rho_\mathrm{fake}^{W+\mathrm{jets}}/\rho_\mathrm{fake}^{Z\to\ell\bar\ell}$ from 1. For the candidate track selection, this is estimated to $\rho_\mathrm{fake}^{W+\mathrm{jets}}/\rho_\mathrm{fake}^{Z\to\ell\bar\ell} = 0.96 \pm 0.16$ leading to a systematic uncertainty of 20%.

6.4.2 Uncertainty on the dE/dx shape of fake tracks

The systematic uncertainty on the shape of the I_as distribution takes into account the differences between the I_as shape in the fake control region $\mathrm{CR}_{I_\mathrm{as}}^\mathrm{fake}$ and in the signal region. For the estimation, information from simulated W + jets events is used. A comparison between the simulated I_as shape in the signal and in the control region can be seen in Fig. 6.11. To enhance the statistical precision only track-based selection cuts are applied.

Table 6.7: Fake rates in simulated $W +$ jets and $Z \to \ell\bar{\ell} +$ jets events for different event-based selections of the $W +$ jets sample. The track-based selection is the candidate track selection from Table 5.4.

$W +$ jets selection	$\rho_{\text{fake}}^{W+\text{jets}}$	$\rho_{\text{fake}}^{Z \to \ell\bar{\ell}}$
$\not{E}_{\text{T}} > 100 \,\text{GeV}, p_{\text{T}}^{1^{\text{st}} \text{jet}} > 110 \,\text{GeV}$	$\left(3.16^{+4.26}_{-1.94}\right) \cdot 10^{-5}$	$(3.17 \pm 0.21) \cdot 10^{-5}$
$\not{E}_{\text{T}} > 0 \,\text{GeV}, p_{\text{T}}^{1^{\text{st}} \text{jet}} > 70 \,\text{GeV}$	$(3.03 \pm 0.68) \cdot 10^{-5}$	$(3.17 \pm 0.21) \cdot 10^{-5}$
$\not{E}_{\text{T}} > 0 \,\text{GeV}, p_{\text{T}}^{1^{\text{st}} \text{jet}} > 70 \,\text{GeV}$, no QCD cuts	$(3.05 \pm 0.44) \cdot 10^{-5}$	$(3.17 \pm 0.21) \cdot 10^{-5}$

The 1-sigma difference of the ratio of the number of events in the signal region and the control region from one is taken as systematic uncertainty. For a signal region definition with $p_{\text{T}} > 20 \,\text{GeV}$ and $I_{\text{as}} > 0.2$ this corresponds to an uncertainty of around 21% and for a definition with $p_{\text{T}} > 40 \,\text{GeV}$ and $I_{\text{as}} > 0.2$ of around 25%.
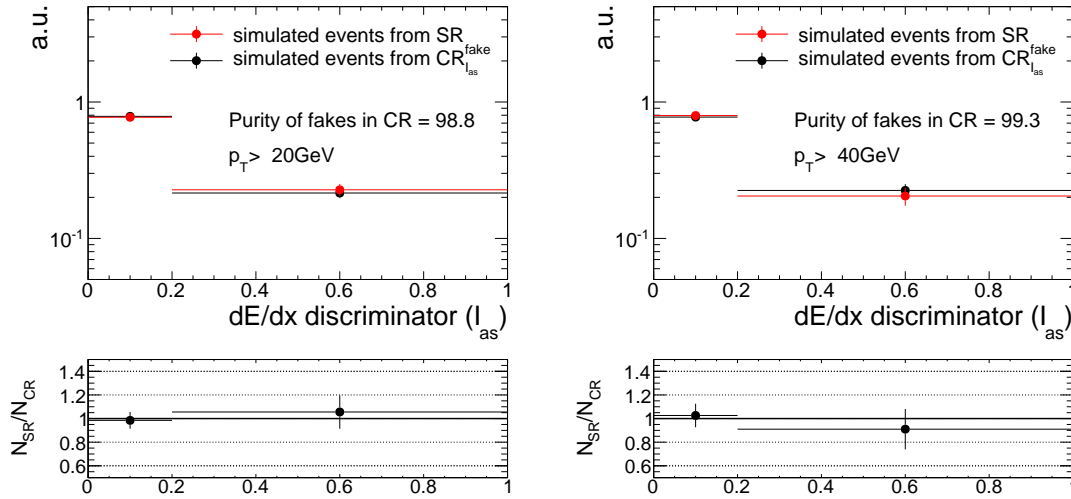

Figure 6.11: Underlying histograms to estimate the fake I_{as} systematic uncertainty. Normalised distributions of the I_{as} shape of fake tracks in the signal and control region of simulated $W +$ jets events with a p_{T} selection of $20 \,\text{GeV}$ (left) and a $40 \,\text{GeV}$ (right).

6.4.3 Uncertainty on the leptonic scale factor

The leptonic scale factor $\rho_{\mathrm{MC}}^{\mathrm{lep}_i}$ is estimated on simulated W+jets events. The corresponding systematic uncertainty that addresses the use of information from simulation is derived by a "tag-and-probe" method conducted on real data and simulated events.

For this method a selection of $Z \to \ell\bar{\ell}$ events is done with one "tagged" well reconstructed lepton and one "probed" candidate track. To ensure a selection of $Z \to \ell\bar{\ell}$ events, a selection on the invariant mass of the reconstructed lepton and the candidate track is applied with $80\,\mathrm{GeV} < M_{\mathrm{inv}}\,(\mathrm{lepton}, \mathrm{cand.\ trk}) < 100\,\mathrm{GeV}$ for muons and electrons. For taus, a muon from a $\tau \to \mu\nu\nu$ decay is selected with $40\,\mathrm{GeV} < M_{\mathrm{inv}}\,(\mu, \mathrm{cand.\ trk}) < 75\,\mathrm{GeV}$ and $m_T\,(\mu, \not{E}_{\mathrm{T}}) < 40\,\mathrm{GeV}$ [36, 37]. Furthermore, the candidate track and the lepton are required to be opposite in charge. In order to reduce the contamination of fakes in the "tag-and-probe" samples an additional selection on the number of hits of $N_{\mathrm{hits}} > 5$ is required.

The "tag-and-probe" selection is done for each lepton type separately. In order to determine the leptonic scale factors, the number of events is once estimated for the candidate track selection including the corresponding lepton veto which gives the a number of events in the "tag-and-probe" signal region $N_{SR}^{\mathrm{T\&P}}$, and once inverting the lepton veto selection requirement which gives the the number of events in the "tag-and-probe" lepton inverted control region $N_{\mathrm{CR,\ lepton\ veto\ inverted}}^{\mathrm{T\&P}}$. As for the determination of the tau and electron scale factor with simulated $W + $ jets events, no requirement on the calorimeter isolation is applied in the lepton veto inverted control region for taus and electrons. This leads to the following expression of the lepton scale factor for muons

$$\rho^{\mu} = \frac{N_{\mathrm{SR}}^{\mathrm{T\&P}\mu}}{N_{\mathrm{CR,\ \mu\ veto\ inverted}}^{\mathrm{T\&P}}}.$$

and for electrons and taus

$$\rho^{e,\tau} = \frac{N_{\mathrm{SR}}^{\mathrm{T\&P}e,\tau}}{N_{\mathrm{CR,\ e,\tau\ veto\ inverted}}^{\mathrm{T\&P}}}.$$

The selection requirements for the three tag-and-probe samples are listed in Tables **??**, **??** and **??** in Appendix **??**.

The leptonic scale factors are calculated using simulated $Z \to \ell\bar{\ell}$ events and real data from the single-muon and single-electron samples listed in Table 6.1. The 1-sigma difference of the ratio $\rho_{\mathrm{MC}}^{\mathrm{lep}_i}/\rho_{\mathrm{Data}}^{\mathrm{lep}_i}$ from unity is taken as systematic uncertainty. This results for the signal candidate selection in an uncertainty of 69% for the electron, 39% for the muon and 79 % for the tau scale factor.

6.4.4 Uncertainty on the leptonic dE/dx shape

The uncertainty on lepton I_{as} shape is estimated by a comparison of the I_{as} shape in data and simulation in the lepton veto inverted control region. Figure 6.12 shows the leptonic I_{as} distributions for all three lepton types in the lepton veto inverted control region in data and simulation. The 1-sigma difference of the ratio of the number of events in the control region in data and simulation from 1 is taken as systematic uncertainty. This leads for example to uncertainties between $37\% - 81\%$ for the signal candidate selection plus a selection requirement of $I_{as} > 0.2$.
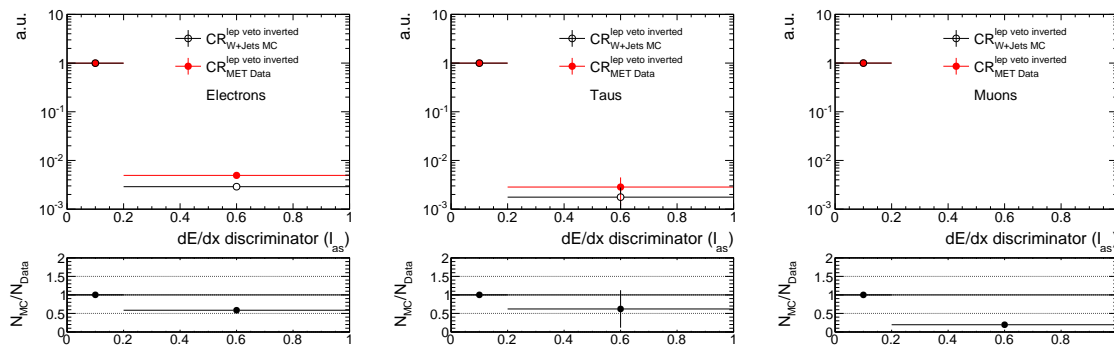
Figure 6.12: Underlying histograms to estimate the leptonic I_{as} systematic uncertainty. Normalised distributions of the lepton I_{as} distributions in the lepton veto inverted control region for data (red) and simulation (black) for all three lepton types. The event-based selection requirements and the calorimeter isolation requirement are removed to enhance the statistical precision.

7 Optimisation of the search sensitivity

Finally, having all background estimation methods in place, an optimisation procedure is conducted in order to increase the search sensitivity with respect to different signal models as introduced in Section 4.2. The optimisation is done in the most sensitive variables, p_T and I_{as} (see Section 3.3 for a definition and explanation of the Asymmetric Smirnov discriminator I_{as}). A potential additional discriminating variable is the number of missing outer hits N_{lost}^{outer} in the tracker system. This variable is, however, not considered in this analysis because studies show that the discriminating potential is limited (see Appendix **??**).

1041   SUSY models with different chargino lifetimes and masses are characterised by different
1042 p_{T} and I_{as} distributions as well as different theoretical cross sections. Therefore, the usual
1043   search optimisation strategy that maximises $N_S/\Delta B$ (N_S = number of signal events of
1044   model S, ΔB = background uncertainty) implies a potential fine-tuning on the specific
1045   SUSY cross sections. In order to keep the search as general as possible, a cross section
1046   independent optimisation is performed. This is achieved by a minimisation of the cross
1047   section for which a 5σ-discovery of the corresponding signal model is possible, i. e. finding
1048   the optimal selection cuts for p_{T} and I_{as} for which the lowest possible cross section, σ_{min},
1049   can be discovered

$$\frac{\alpha_{\mathrm{min}} \cdot N_S(\mathrm{mass}, \mathrm{c}\tau, p_{\mathrm{T}}^{\mathrm{cut}}, I_{\mathrm{as}}^{\mathrm{cut}})}{\Delta B(p_{\mathrm{T}}^{\mathrm{cut}}, I_{\mathrm{as}}^{\mathrm{cut}})} = 5. \qquad \text{with } \alpha_{\mathrm{min}} = \frac{\sigma_{\mathrm{min}}}{\sigma_S}. \qquad (7.1)$$

1050   The number of expected events N_S of the signal model S depends on the p_{T} and I_{as}
1051   selection cut as well as the mass and the lifetime of the chargino. The uncertainty on
1052   the background ΔB is dependent on the p_{T} and I_{as} cut, and takes into account the full
1053   systematic uncertainty as well as the statistical uncertainty on the background prediction
1054   which is the 68% one sided upper limit of a Poisson distribution with $\mu = N_B$ estimated
1055   with the Neyman construction [20, 46]. The systematic uncertainty on the background
1056   prediction includes systematic uncertainties as described in Section 6.4, and statistical
1057   uncertainties arising from limited statistical precision of the control regions and simulated
1058   samples used in the background estimation. The factor α_{min} that is minimised is the ratio
1059   of the minimum cross section σ_{min} divided by the nominal cross section σ_S of the signal
1060   model S.

1061

1062   As this analysis focuses on short tracks, rather low lifetimes are considered in the opti-
1063   misation procedure: $\mathrm{c}\tau = 1\,\mathrm{cm}$, $10\,\mathrm{cm}$, $50\,\mathrm{cm}$. These lifetimes are further suitable as they
1064   lie at the edge of the sensitivity of the search for disappearing tracks [11]. To cover the
1065   full mass space, the optimisation is done for masses between $100\,\mathrm{GeV}$ and $500\,\mathrm{GeV}$. The
1066   corresponding results are shown in Table 7.1.
1067   It can be seen that the optimal selection is highly dependent on the signal models. The
1068   best sensitivity for low masses ($\leq 200\,\mathrm{GeV}$) is mainly achieved by soft selection cuts in
1069 p_{T} between $20 - 30\,\mathrm{GeV}$, while models with higher chargino masses require tighter p_{T}
1070   selections of around $50\,\mathrm{GeV}$. The optimal I_{as} selection is mostly dependent on the mass of
1071   the chargino. For low masses and low lifetimes a soft selection in $I_{\mathrm{as}} > 0.05$ is preferred.
1072   Since for longer lifetimes more charginos are able to reach the tracking system, a tighter
1073   selection in I_{as} of 0.3 is preferable. For high masses the highest search sensitivity is always
1074   achieved by a high I_{as} selection cut of 0.3.

1075

1076   In order to visualise the mass and $\mathrm{c}\tau$ dependence of the optimal p_{T} and I_{as} selection, the

Table 7.1: Optimal p_T and I_as selection cuts and the corresponding minimum cross section σ_min that can be discovered with 5σ significance for different signal models. For some signal samples, an optimisation result is not available due to the limited size of these samples.

Mass [GeV]	Lifetime [cm]	Optimal p_T cut	Optimal I_as cut	σ_min
100	1	30	0.05	61.596
200	1	20	0.05	43.414
300	1	n/a	n/a	n/a
400	1	n/a	n/a	n/a
500	1	n/a	n/a	n/a
100	10	30	0.05	1.531
200	10	30	0.30	0.561
300	10	30	0.30	0.354
400	10	30	0.30	0.238
500	10	50	0.30	0.201
100	50	50	0.30	0.435
200	50	50	0.30	0.110
300	50	50	0.30	0.063
400	50	50	0.30	0.045
500	50	50	0.30	0.037

optimisation results for two very different lifetimes (5 cm and 50 cm) and masses (100 GeV and 500 GeV) are shown in Fig. 7.1, where the minimum cross section that is possible to discover is shown in the $p_\mathrm{T} - I_\mathrm{as}$ plane. For the visualisation, general systematic uncertainties on the leptonic and the fake background of 100% and 20% respectively are imposed. Uncertainties arising from limited statistical precision of the samples used for the background estimation are propagated consistently into formula 7.1. Similar to the full optimisation, it can be seen that for low masses and low lifetimes, the highest search sensitivity is achieved by imposing rather soft selection cuts on I_as and p_T. Optimising for higher lifetime pushes the optimal selection in p_T and I_as to larger values, where signal
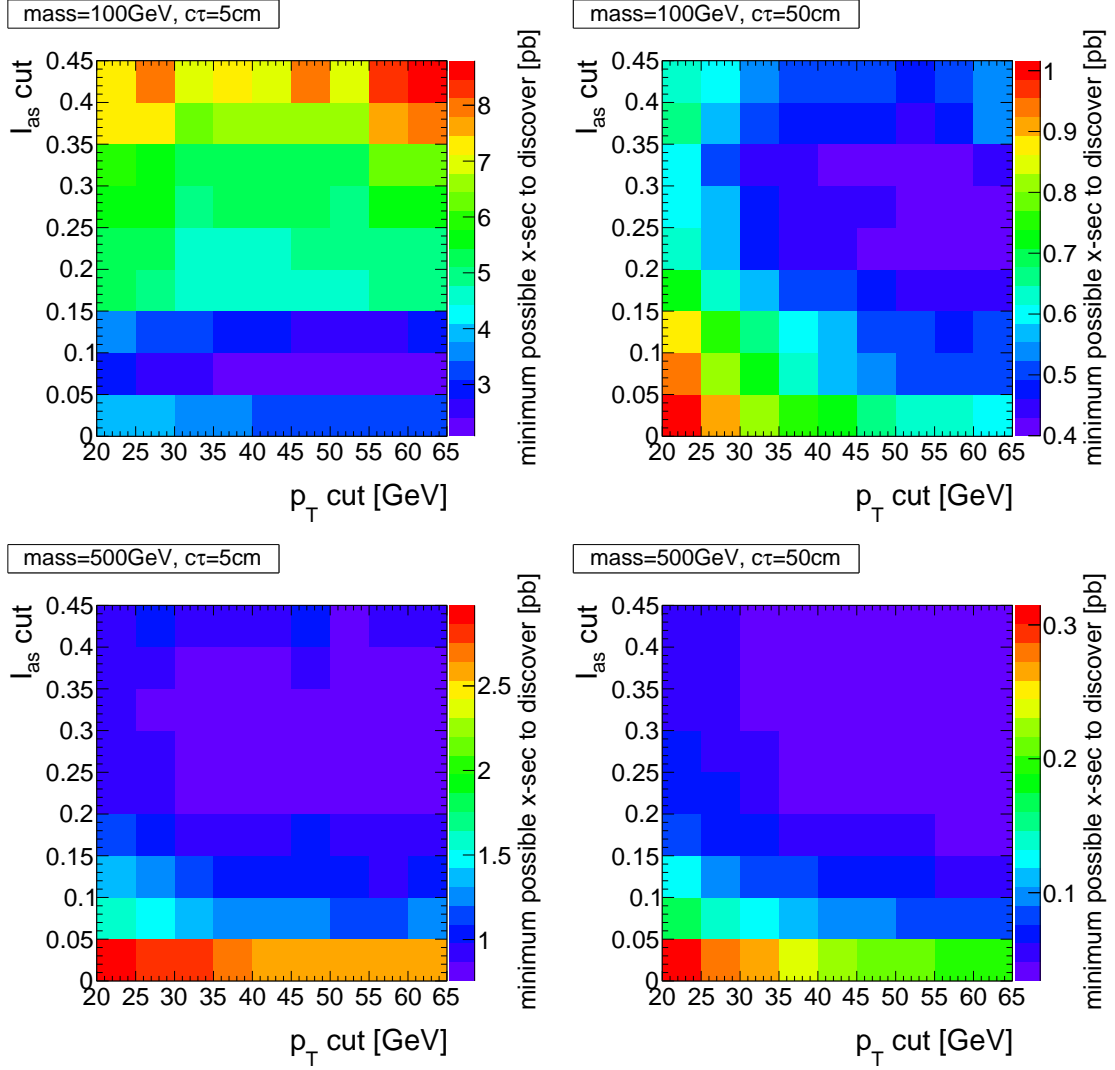
Figure 7.1: Minimum possible cross section that can be discovered with 5σ significance in the $I_{as}-p_T$ plane for four different signal models. The systematic uncertainties are taken to be 20% and 100% for the fake and the leptonic background respectively. The uncertainty on the background arising from the limited size of the used samples are propagated consistently to the search optimisation. In Table **??** of Appendix **??**, the corresponding histograms of the background yield, the background uncertainty and the signal yield for the four signal models can be found.

models with higher masses prefer even tighter I_{as} selection cuts than the corresponding lower mass signal model. It can also be seen, that for low lifetimes, the p_T dependence of the search sensitivity is less pronounced than for long lifetimes.

Based on the optimisation, four different exclusive signal regions are defined in order to achieve an optimal coverage over a wide mass space and a high sensitivity for different lifetimes:

1.) $30\,\text{GeV} < p_T < 50\,\text{GeV}$ and $0.05 < I_{as} < 0.3$

2.) $p_T > 50\,\text{GeV}$ and $0.05 < I_{as} < 0.3$

3.) $30\,\text{GeV} < p_T < 50\,\text{GeV}$ and $I_{as} > 0.3$

4.) $p_T > 50\,\text{GeV}$ and $I_{as} > 0.3$.

The unblinded results of the search for highly ionising, short tracks are presented in the following chapter.

8 Results

After developing the methods of the background estimation for all different background sources and their corresponding systematic uncertainties (all explained in Section 6), the search is performed in four exclusive signal regions with $19.7\,\text{fb}^{-1}$ of data collected at a centre-of-mass energy of $\sqrt{s} = 8\,\text{TeV}$ at the CMS experiment. The predicted number of events for the fake and the leptonic background in the four signal regions is depicted in Table 8.1. It can be seen, that fake tracks are by far the dominant background to this search. The leptonic background contributes only in one signal region to the total background with a share of about 10%.

Finally, the comparison between the predicted number of events and the number of observed events is shown in Fig. 8.1. Additionally, the corresponding numbers of predicted and observed events can be found in Table 8.2. The event yields observed in data after each selection requirement for the four signal regions are listed in Table **??** in Appendix **??**.

The results are compatible with the Standard Model background within 1σ uncertainties in all four signal regions. No excess above the SM prediction is observed in either of the four signal regions. Thus, no evidence for physics beyond the Standard Model could be found.

Table 8.1: Background prediction in the four exclusive signal regions for the fake and the leptonic background.

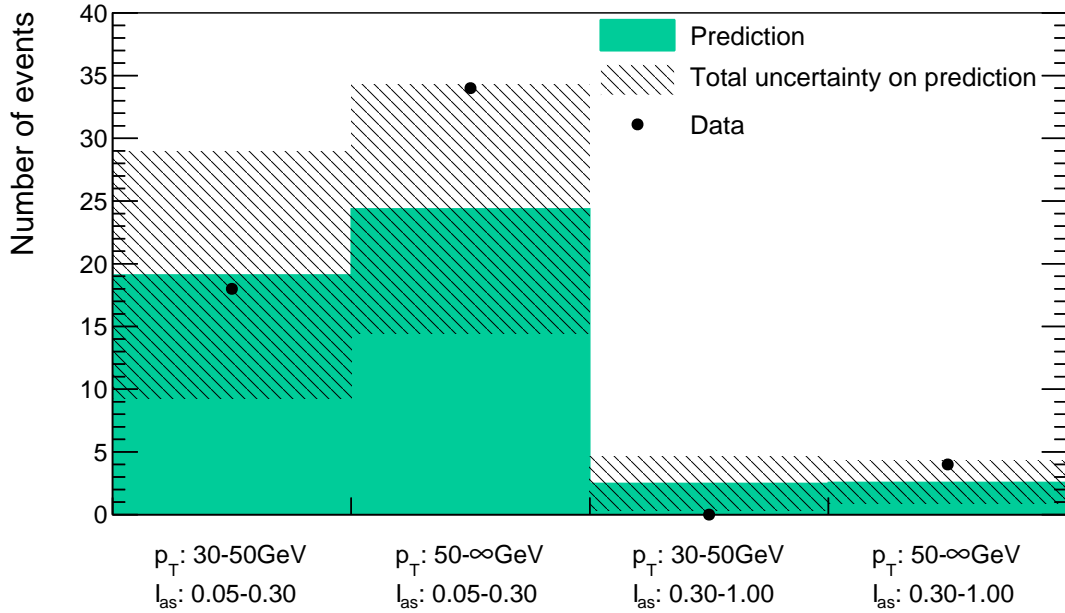| Signal region	Fake Bkg	Leptonic Bkg
$p_T : 30 - 50\,\text{GeV} \ / \ I_{as} : 0.05 - 0.30$	$19.11\ ^{+2.61}_{-2.61}$ (stat) $\pm$ 9.35 (sys)	$0.00\ ^{+2.58}_{-0.00}$ (stat) $\pm$ 0.00 (sys)
$p_T : 50 - \infty\,\text{GeV} \ / \ I_{as} : 0.05 - 0.30$	$22.21\ ^{+3.60}_{-3.60}$ (stat) $\pm$ 8.78 (sys)	$2.17\ ^{+2.99}_{-1.34}$ (stat) $\pm$ 1.65 (sys)
$p_T : 30 - 50\,\text{GeV} \ / \ I_{as} : 0.30 - 1.00$	$2.49\ ^{+0.85}_{-0.85}$ (stat) $\pm$ 1.98 (sys)	$0.00\ ^{+0.22}_{-0.00}$ (stat) $\pm$ 0.00 (sys)
$p_T : 50 - \infty\,\text{GeV} \ / \ I_{as} : 0.30 - 1.00$	$2.52\ ^{+1.14}_{-1.14}$ (stat) $\pm$ 1.27 (sys)	$0.04\ ^{+0.30}_{-0.03}$ (stat) $\pm$ 0.03 (sys)

Figure 8.1: Number of predicted (green area) and observed (black dots) events for the four different signal regions. The hashed area represents the total uncertainty on the background prediction.

Table 8.2: Number of predicted and observed events for the four different signal regions.

Signal region	Prediction	Observation
$p_{\mathrm{T}} : 30 - 50\,\mathrm{GeV}\ /\ I_{\mathrm{as}} : 0.05 - 0.30$	$19.11\ ^{+3.67}_{-2.61}\ \text{(stat)} \pm 9.35\ \text{(sys)}$	18
$p_{\mathrm{T}} : 50 - \infty\,\mathrm{GeV}\ /\ I_{\mathrm{as}} : 0.05 - 0.30$	$24.38\ ^{+4.68}_{-3.84}\ \text{(stat)} \pm 8.93\ \text{(sys)}$	34
$p_{\mathrm{T}} : 30 - 50\,\mathrm{GeV}\ /\ I_{\mathrm{as}} : 0.30 - 1.00$	$2.49\ ^{+0.87}_{-0.85}\ \text{(stat)} \pm 1.98\ \text{(sys)}$	0
$p_{\mathrm{T}} : 50 - \infty\,\mathrm{GeV}\ /\ I_{\mathrm{as}} : 0.30 - 1.00$	$2.57\ ^{+1.18}_{-1.14}\ \text{(stat)} \pm 1.27\ \text{(sys)}$	4

Therefore, in the following section these results will be used to constrain the parameter space of supersymmetric models with almost mass degenerate charginos and neutralinos.

9 Interpretation

In order to interpret the result of the search in the context of supersymmetric models with almost mass degenerate charginos and neutralinos, sources of systematic uncertainties on the number of selected signal events must be identified and quantified. The interpretation will then be done with statistical methods that allow for the exclusion of parts of the supersymmetric parameter space on a 95% confidence level.

9.1 Systematic uncertainties of simulated signal samples

The systematic uncertainties on the number of signal events in the four signal regions are mainly caused by uncertainties on the quality of the simulation. This influences the signal efficiency of each selection requirement in this analysis. Furthermore, an uncertainty on the overall number of events is caused by the uncertainty on the integrated luminosity recorded in 2012 at CMS and the theoretical signal cross sections.

All systematic uncertainties are estimated for each signal model and each search bin separately. In the following, the sources of systematic uncertainties are discussed and the minimum and maximum value of the corresponding uncertainty is given.

Uncertainty on the theoretical cross section

The theoretical cross sections of $\tilde{\chi}_1^{\pm}\tilde{\chi}_1^{\mp}$ and $\tilde{\chi}_1^{\pm}\tilde{\chi}_1^0$ production at a centre-of-mass energy of 8 TeV are taken from [34, 35]. The corresponding theoretical uncertainties range between $4.5 - 12.1\%$.

Luminosity uncertainty

The integrated luminosity recorded at CMS during the year 2012 is measured by counting of pixel clusters during the crossing of two bunches (zero-bias event). A detailed explanation of this method and the corresponding total uncertainty of 2.6% can be found in [47].

Uncertainty on the simulation of initial state radiation

Initial state radiation affects the transverse momentum distribution of the 2-particle system, $p_T\,(p_1^{\mu} + p_2^{\mu})$, in a 2-body decay. Differences between data and simulation of ISR are taken into account by reweighting the simulated events, such that the simulated transverse momentum distribution matches the measured distribution in data. The weights and associated systematic uncertainties are determined in [48] by comparing simulated and observed p_T distributions of Z and $t\bar{t}$ events. These weights are applied to the simulated $\tilde{\chi}_1^{\pm}\tilde{\chi}_1^{\mp}$ and $\tilde{\chi}_1^{\pm}\tilde{\chi}_1^0$ events. To account for the systematic uncertainties on the reweighting procedure, the event weights are varied up and down by up to 25% according to [48] depending on the $p_T^{\chi_1\chi_2}$. The resulting uncertainty on the ISR simulation is between $9.2 - 12.6\%$.

Uncertainty on the simulation of the trigger efficiency

The HLTMonoCentralPFJet80_PFMETnoMu105_NHEF0p95 trigger with the higher MET threshold of 105 GeV active in Run C and Run D during 2012 was not available in the simulated signal samples. It is therefore emulated using HLT trigger information. More details on the emulation of this trigger can be found in Appendix **??**.

The trigger uncertainty is assessed by comparing data-simulation differences of the trigger efficiency. This uncertainty has been quantified within [36, 37] by comparing simulated and measured trigger turn-on curves and determining weights for simulated events such that simulated and observed turn-on curves are compatible. These event weights are applied on the simulated signal samples in this analysis and lead to changes in the signal prediction of $1.9 - 4.4\%$.

Uncertainty on the jet energy scale

The transverse momentum of all jets is corrected for non-uniformities in the energy response as a function of the jet η and p_T and for data-simulation differences [49]. The uncertainty on the jet energy scale (JES) is neatly described and quantified in [49]. It arises from uncertainties on the jet response in data including jet fragmentation, jet flavor composition, etc.. The JES correction is applied as a multiplicand on each jet's transverse momentum contained in an event. The corresponding systematic uncertainty is assessed by an up- and downward variation of the correction factor within $1\,\sigma$. The resulting uncertainties are of minor importance and range between $0.4 - 3.1\%$.

Uncertainty on the jet energy resolution

The jet energy resolution (JER) is smaller in simulation than in measured data (see Part **??**). In order to take these differences into account, the simulated jet energy response is smeared to match the measured response. The systematic uncertainty on the smearing factors is estimated in [49, 50]. It covers the uncertainty on JER in data, including the JES uncertainty, uncertainties arising from out-of-cone showering etc. [49, 50]. The resulting uncertainty on the signal efficiency in this study is between $0.1 - 2.0\%$ and therefore almost negligible.

Uncertainty on the simulation of the parton distribution functions

The parton distribution function (PDF) used for the simulation of proton-proton collisions is provided by the CTEQ group [51] (see Section **??** for more information about PDFs). In [51], a detailed description of the determination of a parton distribution function and its uncertainties is given. Practically, the estimation of the PDF uncertainty is done by the application of 44 different sets of event weights which take into account 22 different sources of uncertainties [52, 53] (up and down variations lead to a factor of 2). The sources correspond inter alia to uncertainties in the single distributions of gluons, up/down-quarks, etc, with the gluon distribution being by far the largest source of uncertainty.

The resulting uncertainties on the signal efficiency for this search are between $2.6 - 6.8\%$.

Uncertainty of the pileup reweighting

The distribution of the number of primary vertices in simulation is reweighted to match the measured distribution in data. The number of primary vertices in data is determined by the luminosity of each bunch-crossing times the proton-proton inelastic cross section which is $69.4\,\mathrm{mb}$ [54]. The uncertainty on the number of interactions thus consists of the uncertainty on the luminosity and the uncertainty on the cross section. To cover both

sources, a variation of the inelastic cross section by plus/minus 5% is done according to the recommendation by [55].

For most of the signal models and signal regions, the signal efficiency is only affected by less than 1% by the pileup reweighting uncertainty. If the statistical precision of the signal prediction in a specific search bin is low, the uncertainty can become significantly larger. However, the search sensitivity is always driven by search bins with high signal content so that large values of this uncertainty have no effect on the overall search sensitivity.

Uncertainty on the simulation of the calorimeter isolation

The uncertainty on the simulation of the calorimeter isolation $E_{\mathrm{calo}}^{\Delta R < 0.5}$ is estimated by comparing simulated and measured selection efficiencies of $E_{\mathrm{calo}}^{\Delta R < 0.5} < 5\,\mathrm{GeV}$ in the fake enriched control sample $\mathrm{CR}_{I_{\mathrm{as}}}^{\mathrm{fake}}$. The fake enriched control region is well suited for this estimation, as fake tracks are also expected to deposit only a low amount of energy in the calorimeters. The selection efficiency in data is higher than in simulation in both p_{T} bins of $30 - 50\,\mathrm{GeV}$ and $50 - \infty\,\mathrm{GeV}$, resulting in an uncertainty of 12.1% and 3.0% respectively.

Uncertainty on the simulation of missing middle/inner hits

The uncertainty on the simulation of the number of missing inner and middle hits is assessed by comparing the probability in simulation and data of passing the selection requirements of $N_{\mathrm{miss}}^{\mathrm{middle/inner}} = 0$ of a candidate track in the muon-veto inverted control region. This control region is particularly suitable because muons are not expected to have intrinsic sources of missing hits, as e. g. pions or electrons have. Pions can interact nuclearly with the tracker material and electrons can have sizable radiative losses, such that both can change direction or don't deposit energy in a tracker layer. For muons, on the other hand, sources of missing inner and middle hits are mainly algorithmic [36, 37], making them very similar to the algorithmic sources of missing inner/middle hits for chargino tracks.

The uncertainty is estimated as the relative difference of the cut selection efficiency of $N_{\mathrm{miss}}^{\mathrm{middle/inner}} = 0$ in data and simulation. The selection efficiency is always higher in simulation, resulting in systematic uncertainties of around 3.5% for the simulation of $N_{\mathrm{miss}}^{\mathrm{inner}} = 0$ and around 2.2% for $N_{\mathrm{miss}}^{\mathrm{middle}} = 0$. The uncertainties are of very similar size in the signal regions with different p_{T}. No I_{as} dependence is considered.

Uncertainty on the simulation of I_{as}

An uncertainty on the simulation of I_{as} needs to be estimated in order to account for possible data-simulation differences for highly ionising particles. The estimation of the I_{as} uncertainty is done following the methodology in [12, 56]. The I_{as} uncertainty can be

assessed by comparing data and simulation differences of slow protons. Slow protons are highly ionising and can thus be used to determine the uncertainty in the high I_{as} region.

In order to select slow protons, high quality tracks with a momentum smaller than 2.5 GeV are selected. The I_{as} versus momentum distribution for the selected tracks is shown in Fig. 9.1. The kaon, proton, and in data also the deuteron line is visible. Two
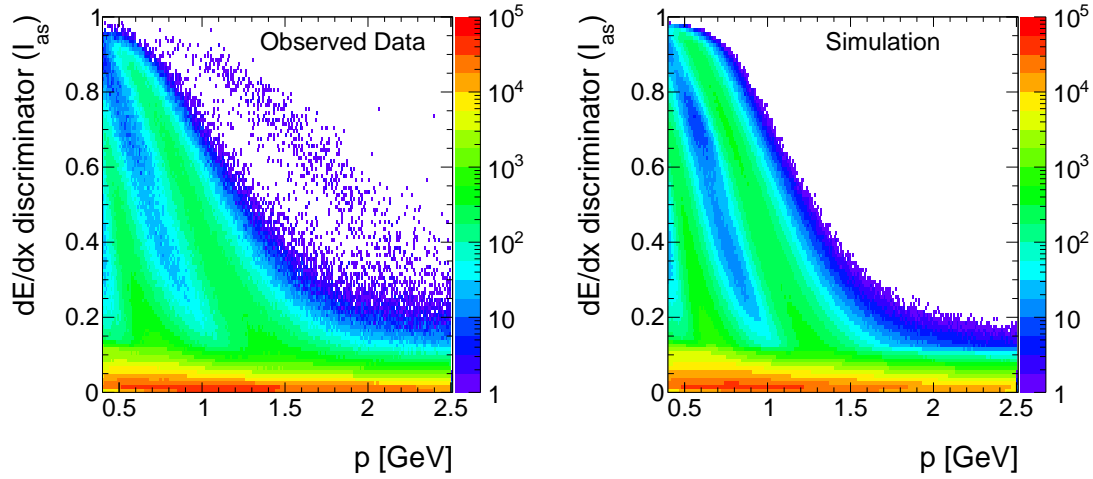

Figure 9.1: I_{as} versus momentum for good quality tracks with at least eight hits in observed data (left) and simulation (right). The kaon and proton line are visible in both datasets. The deuteron line is only visible in data, as deuteron's are not simulated.

different slices in the momentum are extracted where the proton line is contained: p between $0.80 - 0.85$ GeV and $0.95 - 1.00$ GeV. A Gaussian function is fitted to the proton peak and the maximum difference of the mean of the fitted Gaussian between simulation and observed data is taken as systematic uncertainty. The I_{as} distribution for the two momentum ranges with the Gaussian fit is depicted in Fig. 9.2. The systematic uncertainty is estimated to a value of 6%.

Uncertainty on the simulation of the track reconstruction efficiency

One final source of uncertainty is the simulation of the track reconstruction efficiency. Possible differences of the reconstruction efficiency in simulation and data can lead to a different signal acceptance. Differences in the track reconstruction efficiency are especially expected for short tracks. Therefore, a worst case estimation is done, comparing the track reconstruction efficiency in data and simulation for tracks with only three hits.

In simulation and observed data, well reconstructed muon tracks are selected and all hits after the third hit are removed. Afterwards the full track reconstruction is performed
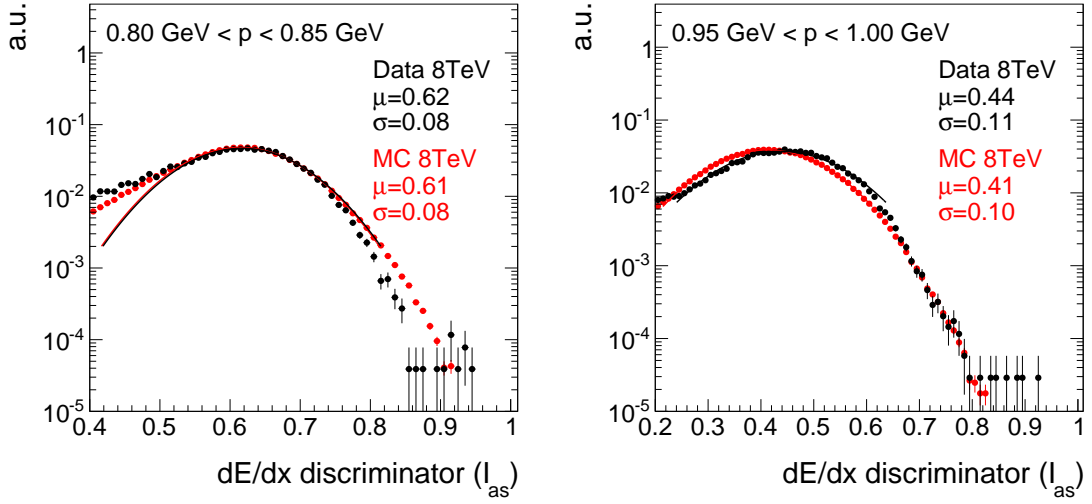
Figure 9.2: I_{as} distribution for slow protons in simulation and observed data for a momentum range of $0.80 - 0.85\,\text{GeV}$ (left) and $0.95 - 1.00\,\text{GeV}$ (left). For the momentum range of $0.80 - 0.85\,\text{GeV}$, the proton line is contained between I_{as} values of $0.4 - 0.8$, whereas for the momentum range of $0.95 - 1.00\,\text{GeV}$, the proton line I_{as} lies between $0.2 - 0.6$.

again. The relative difference of the track reconstruction efficiency in data and simulation ($\epsilon = N_{\text{recon. trk matched to muon trk}}/N_{\text{selected muon trks}}$) is taken as systematic uncertainty. The track reconstruction efficiency is higher in simulation than in data and results in uncertainties between $4.6 - 6.0\%$.

Summary of systematic uncertainties on the simulated signal samples

All systematic uncertainties are estimated for all simulated signal samples and in each of the four signal regions. An overview of the range of the uncertainties is given in Table 9.1.

In order to avoid an overestimation of the systematic uncertainties due to limited sizes of the samples (especially for low lifetimes like $1\,\text{cm}$), the corresponding signal sample with longer lifetime ($100\,\text{cm}$) is used instead for determining the systematic uncertainty. This is possible for uncertainty sources, where the size is not affected by the lifetime of the chargino, including ISR, trigger efficiency, JES, JER, and PDF uncertainties.

It can be seen, that major uncertainties are the simulation of the initial state radiation, of the calorimeter isolation, and of I_{as}. The high maximum value of the pile-up uncertainty is caused by limited statistical precision.

The systematic uncertainties on the simulated signal samples are considered as fully correlated among the four signal regions.

Table 9.1: Ranges of systematic uncertainties on the simulated signal samples. Min and Max correspond to variations between different signal samples and search bins.

Uncertainty	Min [%]	Max [%]
Theoretical x-section	4.5	12.1
Luminosity	2.6	2.6
Simulation of ISR	9.2	12.6
Simulation of trigger efficiency	1.9	4.4
JES	0.4	3.1
JER	0.1	2.0
Simulation of PDF	2.6	6.8
Pile-up reweighting	0.0	16.0
Simulation of calorimeter isolation	3.0	12.1
Simulation of missing middle hits	2.2	2.2
Simulation of missing inner hits	3.3	3.7
Simulation of I_{as}	6.0	6.0
Simulation of track reconstruction efficiency	4.6	6.0

9.2 Statistical Methods/ Limit setting

This section is a small interlude to give a short introduction into the methods and techniques that are used to exclude theoretical models in this analysis. For a detailed and pedagogical introduction to the methods, the reader is referred to [57].

In this analysis, the exclusion of the underlying theoretical model is achieved with the CL_s method [58–60]. A model is considered as excluded at a 95% confidence level if CL_s is smaller than 5%. The CL_s method was developed for the Higgs searches at LEP in order not to overestimate the exclusion power of a result if an under-fluctuation of the background expectation occurs. CL_s is defined as the confidence level of the background plus signal hypothesis divided by the confidence level of the background only hypothesis

$$CL_s = \frac{CL_{s+b}}{CL_b}.$$

The confidence level CL is defined as the probability of obtaining less than or equal the number of observed events $P(n \leq n_{\text{obs}})$ for a given background (or background+signal) hypothesis. In general, the considered distribution can be any test statistics Q and is not necessarily the distribution of the number of events. However, For Poissonian statistics it leads to the following expressions for CL_{s+b} and CL_b for one signal region

$$CL_{s+b} = \text{Poisson}\left(n \leq n_{\text{obs}}|\lambda = b + \mu \cdot s\right),$$
$$CL_b = \text{Poisson}\left(n \leq n_{\text{obs}}|\lambda = b\right),$$

where λ is the mean of the Poisson distribution and the signal strength μ is the measure for the size of the signal cross section.

Systematic uncertainties are included by varying the background expectation b and the signal expectation $\mu \cdot s$ according to a predefined probability density function (pdf). For one Gaussian distributed source of systematic uncertainty on the background, this leads to the following expressions for CL_{s+b} and CL_b

$$CL_{s+b} = \text{Poisson}\left(n \leq n_{\text{obs}}|\lambda = b \cdot (1 + \delta_b) + \mu \cdot s\right) \text{Gauss}\left(\delta_b|\text{mean} = 0, \sigma = \sigma_b\right),$$
$$CL_b = \text{Poisson}\left(n \leq n_{\text{obs}}|\lambda = b \cdot (1 + \delta_b)\right) \text{Gauss}\left(\delta_b|\text{mean} = 0, \sigma = \sigma_b\right),$$

These expressions can be generalised for more than one signal region and more than one systematic uncertainty [57]. In case of multiple signal regions, the distribution of the systematic uncertainties becomes a multi-dimensional probability density function that takes the covariance matrix of the systematic uncertainties in different signal regions into account. In order to get rid of the nuisance parameters δ_s and δ_b, the expression for CL_s is integrated over all possible values of $\delta_{s/b}$. This integration is generally not solvable analytically, but is calculated with pseudo data drawn from the pdf and inserted into the Poisson distribution.

In this search, the systematic uncertainties on the background and the signal yields as well as the statistical uncertainty on the fake background are modelled with log-normal distributions, whereas the statistical uncertainties on the leptonic background are modelled using gamma distributions. A log-normal distribution is used instead of a normal distribution to ensure that the prediction cannot become negative. The gamma distribution is well suited for statistical uncertainties arising from very limited statistical precision in control regions or in simulated samples that are used for the background estimation [61].

Correlations between systematic uncertainties on the background expectation in different search bins are assumed as shown in Table 9.2. The systematic uncertainties on the expected signal yields are considered fully correlated across search bins.

The exclusion limits are derived according to the above presented methodology using the *Combine* framework [61] which was developed for the Higgs searches at CMS.

Table 9.2: Correlation of systematic and statistical uncertainties between the four different signal regions.

	Fakes	Taus	Electrons	Muons
Statistical uncertainty	0% correlated	100% for same bins in I_{as}	0% correlated	100% for same bins in I_{as}
Leptonic scale factor uncertainty	-	100% for same bins in I_{as}	100% for same bins in I_{as}	100% for same bins in I_{as}
Fake rate uncertainty	100% for same bins in I_{as}	-	-	-
I_{as} uncertainty	0% correlated	100% for same bins in p_T	100% for same bins in p_T	100% for same bins in p_T

9.3 Exclusion limits

The presented search for highly ionising, short tracks is interpreted in the context of SUSY models with almost mass degenerate wino-like charginos and neutralinos. As explained in the previous section, the exclusion is done with the help of the CL_s method. Two direct production channels are taken into account: chargino pair production and chargino neutralino production. The corresponding cross sections can be found in Table 4.3.

In total, 37 different lifetimes from $c\tau = 1 - 10000\,\mathrm{cm}$ for each mass point $(100 - 600\,\mathrm{GeV})$ are considered, leading to 37 different exclusion limits. Four exemplary exclusion limits are shown in Fig. 9.3, the full set of exclusion limits can be found in Appendix **??**.

The upper 95% confidence level (CL) limit on the signal cross section is strongest for lifetimes between $10 - 100\,\mathrm{cm}$. For lower lifetimes a sizable fraction of the charginos already decay before reaching the tracker. For longer lifetimes, the cross section upper limit gets weaker again because the charginos start to be reconstructed as muons and do not pass the muon veto. Also, the $E_{\mathrm{calo}}^{\Delta R < 0.5}$ requirement rejects these charginos with higher efficiency.

Due to the falling spectrum of the chargino production cross section, charginos with lower masses are more effectively excluded than charginos with higher masses. A 2-dimensional exclusion limit in the chargino lifetime-mass parameter space is shown in Fig. 9.4.

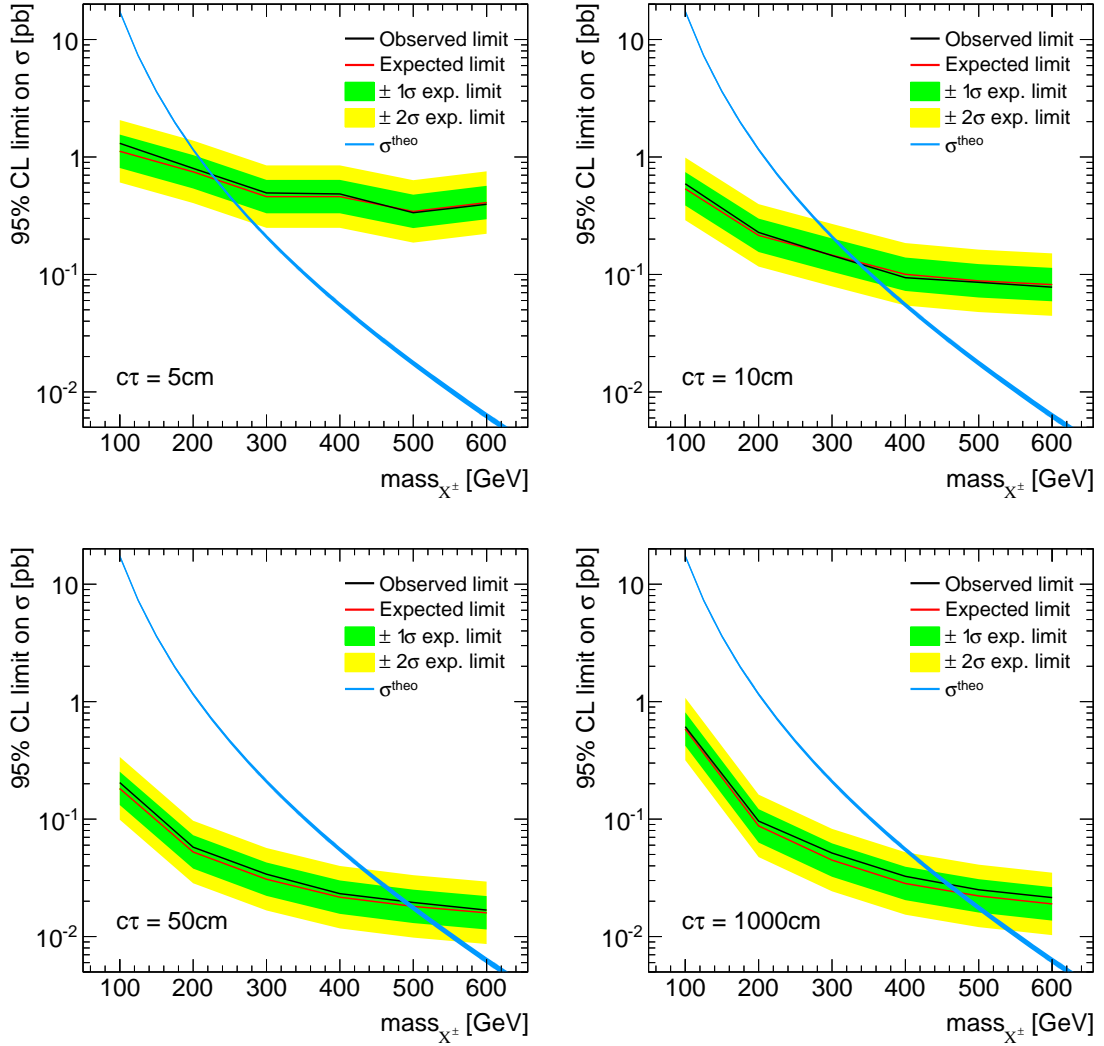Charginos with masses of $100\,\mathrm{GeV}$ can be excluded down to a lifetime of $c\tau = 2\,\mathrm{cm}$.

Figure 9.3: Four different CL_s exclusion limits for charginos with mean lifetimes of $5\,cm$ (top left), $10\,cm$ (top right), $50\,cm$ (bottom left), $1000\,cm$ (bottom right). The red line depicts the expected 95% confidence level (CL) upper cross-section limit with the 1-σ (green band) and 2-σ (yellow band) intervals. The black line is the observed limit. The signal cross section is depicted as a blue line. SUSY models can be excluded at 95% CL if the signal cross section is at least as large as the 95% CL observed upper limit on the cross section.
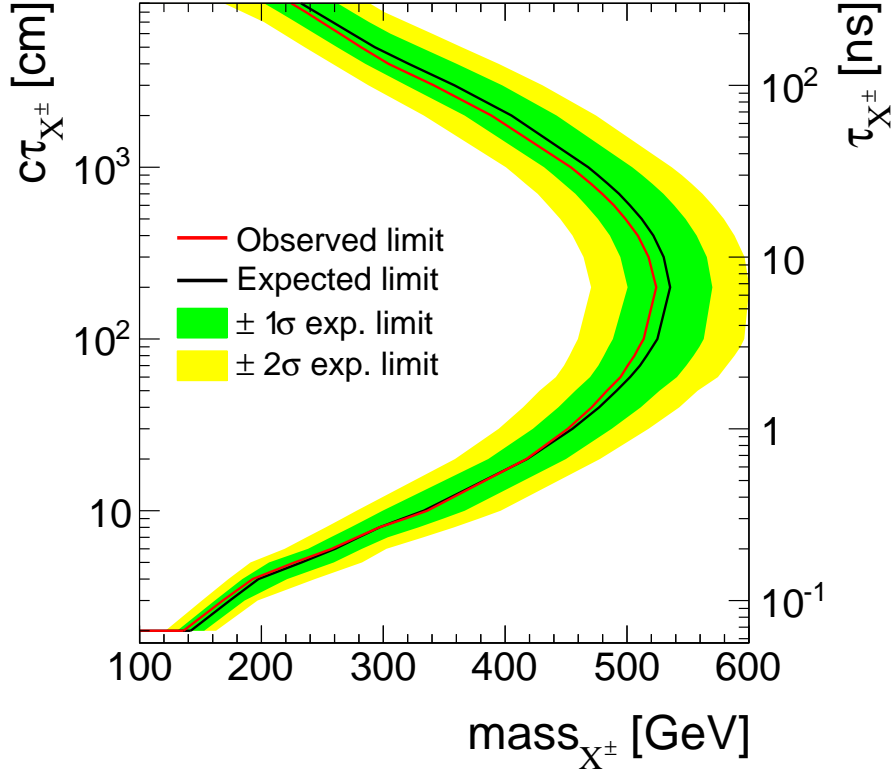
Figure 9.4: Excluded regions in the mass versus lifetime space. All excluded models are located left of the contour line. The red line depicts the expected 95% CL upper cross-section limit with the 1-σ (green band) and 2-σ (yellow band) intervals. The black line is the observed limit.

Charginos with a higher mass of 500 GeV are excluded for lifetimes between $c\tau = 70 - 500$ cm.

Since the lifetime of a wino-like chargino is determined by the mass splitting between $m_{\tilde{\chi}_1^\pm}$ and $m_{\tilde{\chi}_1^0}$, it is possible to express the lifetime of the chargino as a mass gap $\Delta m_{\tilde{\chi}_1^\pm \tilde{\chi}_1^0}$ between the chargino and the lightest neutralino. The correspondence between lifetime and mass gap is taken from [62], where the decay width of $\tilde{\chi}_1^\pm \to \tilde{\chi}_1^0 \pi^\pm$ is expressed in terms of chargino, neutralino, and pion mass. Thus, the mass gaps that are considered are bounded by the pion mass of ~ 140 MeV. The corresponding 2d exclusion limit can be found in Fig. 9.5. It can be seen that this search is sensitive to mass splittings between ~ 140 MeV $- 210$ MeV.

The presented exclusion limits confirm the exclusion from the search for disappearing tracks [11] with slight improvements in the low lifetime region. The comparison of the two
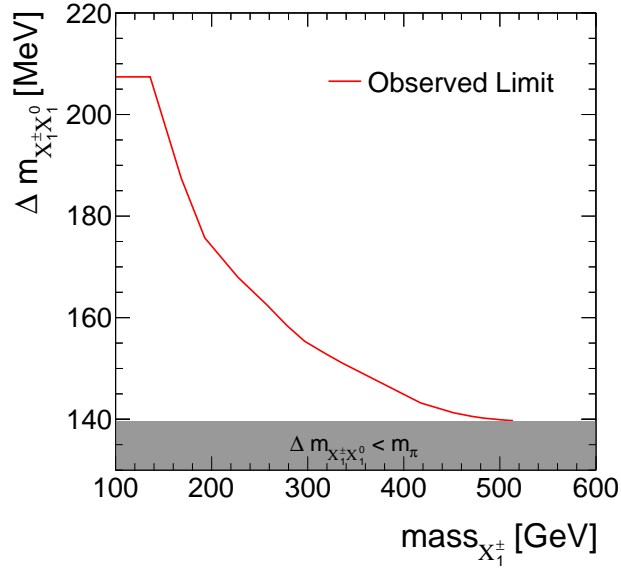
Figure 9.5: Excluded parameter region at 95% CL for wino-like charginos and neutralinos depending on the chargino mass and the mass splitting between $\tilde{\chi}_1^\pm$ and $\tilde{\chi}_1^0$, $\Delta m_{\tilde{\chi}_1^\pm \tilde{\chi}_1^0}$. All SUSY models between the red line and the grey area are excluded.

searches is shown in Fig 9.6.

For charginos with a lifetime of $\tau = 0.07\,\text{ns}$ ($c\tau = 2.1\,\text{cm}$), the observed limit of this search improves the limits derived in [11] by $\sim 35\,\text{GeV}$ in chargino mass, for a lifetime of $\tau = 0.4\,\text{ns}$ ($c\tau = 12.0\,\text{cm}$) by $\sim 25\,\text{GeV}$. For SUSY models with long chargino lifetimes the here presented search shows a higher exclusion power. The weaker exclusion for long lifetimes in [11] is caused by the additional selection cut on the number of missing outer hits, $N_{\text{lost}}^{\text{outer}} \geq 3$.

The confirmation of the excluded parameter space in [11] is especially interesting since the signal regions of the two searches are little correlated. The correlation between simulated signal events, that pass the selection from [11], N_A, and the selection used in this analysis, N_B, can be estimated by the event overlap ρ_{corr}

$$\rho_{\text{corr}} = \frac{N_{A \cap B}}{N_{A \cup B}} = \frac{N_{A \cap B}}{N_A + N_B - N_{A \cap B}}.$$

In order to avoid an over- or underestimation of the event overlap, only the most sensitive signal region from this search is included in N_B. The degree of correlation is depicted in Fig. 9.7 which shows the event overlap for signal models with chargino masses between $100 - 600\,\text{GeV}$ and lifetimes between $5\,\text{cm} - 1000\,\text{cm}$. It can be seen that the event overlap for intermediate lifetimes of around $100\,\text{cm}$ is around 60% and decreases for shorter
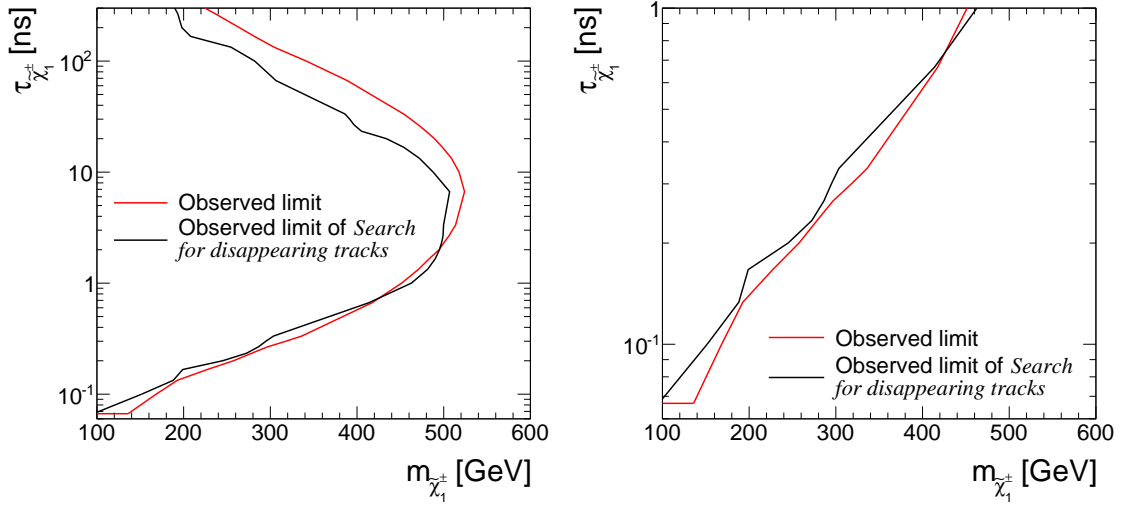
Figure 9.6: Comparison of the excluded regions in the mass versus lifetime space in this analysis (red line) and the search for disappearing tracks [11] (black line). The right figure is a zoom on the low lifetime region. All SUSY models left of the lines are excluded.
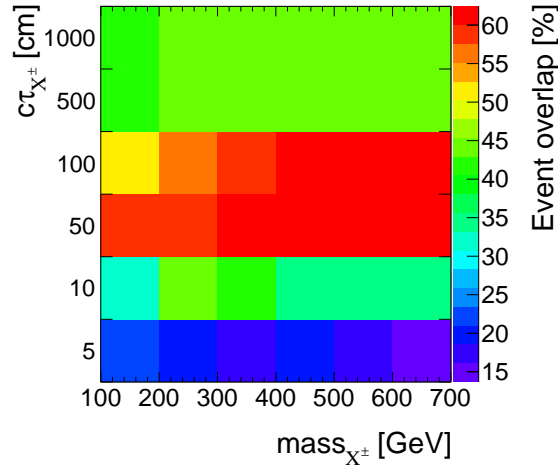

Figure 9.7: The event overlap between simulated signal events, that pass the selection from [11] and the selection used in this analysis for different signal models. The correlation is determined using only the signal region with the highest sensitivity of this analysis.

lifetimes to small overlaps of around $15 - 20\%$. Additionally, the two events that were observed in data by [11] in their signal region are not contained in any of the signal regions in the here presented analysis. Thus, this analysis constitutes an independent confirmation of the exclusion limits derived in [11].

10 Discussion and conclusion

The here presented search for highly ionising, short tracks is motivated by supersymmetric models with almost mass-degenerate wino-like charginos $\tilde{\chi}_1^{\pm}$ and neutralinos $\tilde{\chi}_1^0$. Such scenarios are well motivated by astrophysical observations that suggest the existence of large amounts of dark matter. It is possible to explain the relic density with wino-like neutralinos if they are non-thermally produced via the decay of long-lived particles, such as a wino-like chargino [9].

The presented analysis is designed to increase the search sensitivity on SUSY models with low chargino lifetimes. It extends the search for disappearing tracks [11] by the inclusion of the variable dE/dx. In order to increase the search sensitivity with respect to short lifetimes, energy information from the pixel silicon tracker is taken into account. For this purpose, a dedicated pixel energy calibration was carried out within this thesis to ensure stable energy measurements over time and across pixel modules. This is thus the first analysis at CMS that makes use of energy information from the pixel tracker. By adding pixel energy information the discrimination power of dE/dx is significantly increased.

Overall, dE/dx inclusion allows for loosening the requirement on the number of hits in the tracker with respect to [11] that leads to a strong suppression of signal events for low chargino lifetimes. The Asymmetric Smirnov discriminator, I_{as}, which is used for dE/dx discrimination in this analysis, shows good separation power and can lead to sensitivity increases up to 400% (cf. Fig. 7.1).

The Standard Model background is mainly estimated with data-based techniques. The main background to this search is arising from fake tracks, i.e. tracks that are reconstructed out of several particles' trajectories. Fake tracks are typically short and can have large values of I_{as}, thus showing a very signal-like signature in the detector. The uncertainty on the fake background is dominated by systematic uncertainties originating from low statistical precision in the simulated datasets. Simulating more events could therefore significantly improve the search sensitivity. This strategy is however technically

challenging, since storage capacity limits were already reached within the current analysis. Still, reducing the uncertainty will be one of the main tasks in order to increase the search sensitivity.

Even though this search already features low background, a further background suppression is desirable. However, the impact on the search sensitivity will be limited because of the high relative Poisson error on low background predictions. For instance, a reduction of the number of background events by 75% from 4 to 1 event reduces the signal yield required for a 5σ-discovery by around 30%, whereas a 75% reduction of expected background events from 400 to 100 reduces the required signal yield by 70%.

In the current analysis, the background is estimated at $19 - 24$ events in the low I_{as} signal regions and $2.5 - 2.6$ events in the high I_{as} regions. This background estimate is confronted with collision data recorded during the year 2012 at the CMS experiment at a centre-of-mass energy of 8 TeV. No evidence for physics beyond the Standard Model is found. Thus, the absence of any deviation from the Standard Model prediction is used to constrain the supersymmetric parameter space. Wino-like charginos are excluded down to lifetimes of $c\tau = 2\,\mathrm{cm}$ for $m_{\tilde{\chi}_1^\pm} = 100\,\mathrm{GeV}$. For high mass scenarios of $m_{\tilde{\chi}_1^\pm} = 500\,\mathrm{GeV}$, the excluded lifetime ranges between $c\tau = 70 - 500\,\mathrm{cm}$. This confirms the parameter exclusion limits of the search for disappearing tracks [11]. Interestingly, the signal regions of the here presented search and the search from [11] show little overlap. Therefore, this analysis serves as an independent cross check of [11]. Improvements of the exclusion of SUSY models with respect to existing searches of around $10 - 40\,\mathrm{GeV}$ in chargino mass are achieved in the low lifetime region.

Still, SUSY models with higher mass and low lifetimes could not be fully excluded by any search at the LHC. Therefore, it will stay interesting to further search for these phenomenologically interesting scenarios in collisions at a centre-of-mass energy of 13 TeV. In this context, the here presented approach of combining a selection of short tracks with dE/dx information is especially promising. The expected cross section for SUSY models with higher chargino masses of around 500 GeV will increase by a factor of two at $\sqrt{s} = 13\,\mathrm{TeV}$. Since dE/dx is much more discriminating for high masses, the sensitivity impact is expected to be even more pronounced for 13 TeV data.

Bibliography

[1] CDF, D0 Collaboration, T. Adams, "SUSY Searches at the Tevatron", in *Hadron collider physics. Proceedings, 19th Symposium, HCP2008, Galena, USA, May 27-31, 2008*. 2008. `arXiv:0808.0728`.

[2] ALEPH, DELPHI, L3 and OPAL Collaborations, "Joint SUSY Working Group". `http://http://lepsusy.web.cern.ch/lepsusy/`. LEPSUSYWG (June 2004).

[3] CMS Collaboration, "Search for new physics in the multijet and missing transverse momentum final state in proton-proton collisions at $\sqrt{s}=$ 8 TeV", *JHEP* **06** (2014) 055, `arXiv:1402.4770`. `doi:10.1007/JHEP06(2014)055`.

[4] CMS Collaboration, "Searches for Supersymmetry using the M_{T2} Variable in Hadronic Events Produced in pp Collisions at 8 TeV", *JHEP* **05** (2015) 078, `arXiv:1502.04358`. `doi:10.1007/JHEP05(2015)078`.

[5] ATLAS Collaboration, "Search for squarks and gluinos with the ATLAS detector in final states with jets and missing transverse momentum using $\sqrt{s} = 8$ TeV proton–proton collision data", *JHEP* **09** (2014) 176, `arXiv:1405.7875`. `doi:10.1007/JHEP09(2014)176`.

[6] T. Moroi and L. Randall, "Wino cold dark matter from anomaly mediated SUSY breaking", *Nucl. Phys.* **B570** (2000) 455–472, `arXiv:hep-ph/9906527`. `doi:10.1016/S0550-3213(99)00748-8`.

[7] J. Hisano, S. Matsumoto, M. M. Nojiri et al., "Direct detection of the Wino and Higgsino-like neutralino dark matters at one-loop level", *Phys. Rev.* **D71** (2005) 015007, `arXiv:hep-ph/0407168`. `doi:10.1103/PhysRevD.71.015007`.

[8] M. Ibe, S. Matsumoto, S. Shirai et al., "Wino Dark Matter in light of the AMS-02 2015 Data", *Phys. Rev.* **D91** (2015), no. 11, 111701, `arXiv:1504.05554`. `doi:10.1103/PhysRevD.91.111701`.

[9] T. Moroi, M. Nagai, and M. Takimoto, "Non-Thermal Production of Wino Dark Matter via the Decay of Long-Lived Particles", *JHEP* **07** (2013) 066, `arXiv:1303.0948`. `doi:10.1007/JHEP07(2013)066`.

[10] J. Hisano, S. Matsumoto, and M. M. Nojiri, "Explosive dark matter annihilation", *Phys. Rev. Lett.* **92** (2004) 031303, `arXiv:hep-ph/0307216`. `doi:10.1103/PhysRevLett.92.031303`.

[11] CMS Collaboration, "Search for disappearing tracks in proton-proton collisions at $\sqrt{s} = 8$ TeV", *JHEP* **01** (2015) 096, `arXiv:1411.6006`. `doi:10.1007/JHEP01(2015)096`.

[12] CMS Collaboration, "Searches for long-lived charged particles in pp collisions at $\sqrt{s}$=7 and 8 TeV", *JHEP* **07** (2013) 122, `arXiv:1305.0491`. `doi:10.1007/JHEP07(2013)122`.

[13] CMS Collaboration, "Phenomenological MSSM interpretation of the CMS 2011 5fb-1 results", *CMS Physics Analysis Summary* **CMS-PAS-SUS-12-030** (2013).

[14] CMS Collaboration, "Reinterpreting the results of the search for long-lived charged particles in the pMSSM and other BSM scenarios", *CMS Physics Analysis Summary* **CMS-PAS-EXO-13-006** (2014).

[15] CMS Collaboration, "Search for disappearing tracks in proton-proton collisions at $\sqrt{s} = 8$ TeV", *Public CMS Wiki* (2015). https://twiki.cern.ch/twiki/bin/view/CMSPublic/PhysicsResultsEXO12034, Topic revision: r9.

[16] CMS Collaboration, "Search for heavy long-lived charged particles in *pp* collisions at $\sqrt{s} = 7$ TeV", *Phys. Lett.* **B713** (2012) 408–433, `arXiv:1205.0272`. `doi:10.1016/j.physletb.2012.06.023`.

[17] CMS Collaboration, "Description and performance of track and primary-vertex reconstruction with the CMS tracker", *JINST* **9** (2014), no. 10, P10009, `arXiv:1405.6569`. `doi:10.1088/1748-0221/9/10/P10009`.

[18] H. Bethe, "Theory of the Passage of Fast Corpuscular Rays Through Matter", *Annalen Phys.* **5** (1930) 325–400. [Annalen Phys.397,325(1930)]. `doi:10.1002/andp.19303970303`.

[19] "National Institute of Standards and Technology". `http://physics.nist.gov/cgi-bin/Star/compos.pl?mode=text&matno=014`. Accessed: 2015-10-21.

[20] Particle Data Group Collaboration, "Review of Particle Physics", *Chin. Phys.* **C38** (2014) 090001. `doi:10.1088/1674-1137/38/9/090001`.

[21] L. Landau, "On the energy loss of fast particles by ionization", *J. Phys.(USSR)* **8** (1944) 201–205.

[22] H. Bichsel, "Straggling in Thin Silicon Detectors", *Rev. Mod. Phys.* **60** (1988) 663–699. `doi:10.1103/RevModPhys.60.663`.

[23] L. Quertenmont, "Search for Heavy Stable Charged Particles with the CMS detector at the LHC". PhD thesis, Louvain, U., 2010. `https://inspirehep.net/record/1088192/files/openfile.pdf`.

[24] D. Kotlinski. personal communication.

[25] T. W. Anderson, "On the Distribution of the Two-Sample Cramr-von Mises Criterion", *The Annals of Mathematical Statistics* **33** (1962), no. 3, pp. 1148–1159.

[26] F. James, "Statistical methods in experimental physics". 2006.

[27] CMS Collaboration, "Tracking and Vertexing Results from First Collisions", *CMS Physics Analysis Summary* **CMS-PAS-TRK-10-001** (2010).

[28] R. Gavin et al., "FEWZ 3.1: A User's Guide". `http://www.hep.anl.gov/fpetriello/FEWZManual_3.1.pdf`. Accessed: 2015-10-27.

[29] M. Czakon, P. Fiedler, and A. Mitov, "Total Top-Quark Pair-Production Cross Section at Hadron Colliders Through $O(\frac{4}{S})$", *Phys. Rev. Lett.* **110** (2013) 252004, `arXiv:1303.6254`. `doi:10.1103/PhysRevLett.110.252004`.

[30] J. Alwall, R. Frederix, S. Frixione et al., "The automated computation of tree-level and next-to-leading order differential cross sections, and their matching to parton shower simulations", *JHEP* **07** (2014) 079, `arXiv:1405.0301`. `doi:10.1007/JHEP07(2014)079`.

[31] T. Sjostrand, S. Mrenna, and P. Z. Skands, "PYTHIA 6.4 Physics and Manual", *JHEP* **05** (2006) 026, `arXiv:hep-ph/0603175`. `doi:10.1088/1126-6708/2006/05/026`.

[32] GEANT4 Collaboration, "GEANT4: A Simulation toolkit", *Nucl. Instrum. Meth.* **A506** (2003) 250–303. `doi:10.1016/S0168-9002(03)01368-8`.

[33] J. Allison et al., "Geant4 developments and applications", *IEEE Trans. Nucl. Sci.* **53** (2006) 270. `doi:10.1109/TNS.2006.869826`.

[34] B. Fuks, M. Klasen, D. R. Lamprea et al., "Gaugino production in proton-proton collisions at a center-of-mass energy of 8 TeV", *JHEP* **1210** (2012) 081, `arXiv:1207.2159`. `doi:10.1007/JHEP10(2012)081`.

[35] B. Fuks, M. Klasen, D. R. Lamprea et al., "Precision predictions for electroweak
     superpartner production at hadron colliders with Resummino", *Eur.Phys.J.* **C73**
     (2013) 2480, `arXiv:1304.0790`. `doi:10.1140/epjc/s10052-013-2480-0`.

[36] J. D. Brinson, "A search for disappearing tracks in proton-proton collisions at $\sqrt{s} =$
     8 TeV". PhD thesis, Ohio State U.
     `https://inspirehep.net/record/1381347/files/CERN-THESIS-2015-030.pdf`.

[37] C. H. J. Brinson and W. Wulsin, "Search for disappearing tracks", *CMS Analysis
     Note* **CMS-AN-12-400** (2014). Internal documentation.

[38] CMS Collaboration, "Tracking and Primary Vertex Results in First 7 TeV
     Collisions", *CMS Physics Analysis Summary* **CMS-PAS-TRK-10-005** (2010).

[39] A. B. et. al., "Search for New Physics in the Monojet final state at CMS", *CMS
     Analysis Note* **CMS-AN-12-421** (2012). Internal documentation.

[40] CMS Collaboration, "Search for dark matter, extra dimensions, and unparticles in
     monojet events in protonproton collisions at $\sqrt{s} = 8$ TeV", *Eur. Phys. J.* **C75**
     (2015), no. 5, 235, `arXiv:1408.3583`. `doi:10.1140/epjc/s10052-015-3451-4`.

[41] CMS Collaboration, "Studies of Tracker Material", *CMS Physics Analysis Summary*
     CMS-PAS-TRK-10-003 (2010).

[42] CMS Collaboration, "Measurement of Higgs boson production and properties in the
     WW decay channel with leptonic final states", *JHEP* **01** (2014) 096,
     `arXiv:1312.1129`. `doi:10.1007/JHEP01(2014)096`.

[43] CMS Collaboration, "Performance of Electron Reconstruction and Selection with
     the CMS Detector in Proton-Proton Collisions at s = 8 TeV", *JINST* **10** (2015),
     no. 06, P06005, `arXiv:1502.02701`. `doi:10.1088/1748-0221/10/06/P06005`.

[44] CMS Collaboration, "Performance of CMS muon reconstruction in *pp* collision
     events at $\sqrt{s} = 7$ TeV", *JINST* **7** (2012) P10002, `arXiv:1206.4071`.
     `doi:10.1088/1748-0221/7/10/P10002`.

[45] CMS Collaboration, "Performance of tau-lepton reconstruction and identification in
     CMS", *JINST* **7** (2012) P01001, `arXiv:1109.6034`.
     `doi:10.1088/1748-0221/7/01/P01001`.

[46] J. Neyman *Phil. Trans. Royal Soc. London, Series A* **236** (1937) 333–80. Reprinted
     in *A Selection of Early Statistical Papers on J. Neyman* (University of California
     Press, Berkeley, 1967).

[47] CMS Collaboration, "CMS Luminosity Based on Pixel Cluster Counting - Summer 2013 Update", *CMS Physics Analysis Summary* **CMS-PAS-LUM-13-001** (2013).

[48] D. B. et. al., "Hadronic Recoil Studies of Heavy Boosted Systems", *CMS Analysis Note* **CMS-AN-13-059** (2013). Internal documentation.

[49] CMS Collaboration, "Jet Energy Scale and Resolution in the CMS Experiment", *CMS Physics Analysis Summary* **CMS-PAS-JME-13-004** (2015).

[50] K. Goebel, "Probing supersymmetry based on precise jet measurements at the CMS experiment". PhD thesis, U. Hamburg, Dept. Phys., 2015. `http://www-library.desy.de/cgi-bin/showprep.pl?thesis15-003`.

[51] J. Pumplin, D. R. Stump, J. Huston et al., "New generation of parton distributions with uncertainties from global QCD analysis", *JHEP* **07** (2002) 012, `arXiv:hep-ph/0201195`. `doi:10.1088/1126-6708/2002/07/012`.

[52] M. Botje et al., "The PDF4LHC Working Group Interim Recommendations", `arXiv:1101.0538`.

[53] A. Vicini, "Practical implementation of the PDF4LHC recipe". `http://www.hep.ucl.ac.uk/pdf4lhc/PDF4LHC_practical_guide.pdf`. Accessed: 2015-11-27.

[54] CMS Collaboration, "Pileup Reweighting Utilities", *Internal CMS Wiki* (2012). https://twiki.cern.ch/twiki/bin/viewauth/CMS/PileupMCReweightingUtilities, Topic revision: r29.

[55] CMS Collaboration, "Estimating Systematic Errors Due to Pileup Modeling", *Internal CMS Wiki* (2013). https://twiki.cern.ch/twiki/bin/view/CMS/PileupSystematicErrors, Topic revision: r11.

[56] L. Q. at al., "Searches for Heavy Stable Charged Particles with Combined 2011 and 2012 Datasets", *CMS Analysis Note* **CMS-AN-12-293** (2013). Internal documentation.

[57] J. Ott, "Search for Resonant Top Quark Pair Production in the Muon+Jets Channel with the CMS Detector". PhD thesis, Hamburg U., 2013. `https://inspirehep.net/record/1296889/files/TS2013_046.pdf`.

[58] T. Junk, "Confidence level computation for combining searches with small statistics", *Nucl. Instrum. Meth.* **A434** (1999) 435–443, `arXiv:hep-ex/9902006`. `doi:10.1016/S0168-9002(99)00498-2`.

[59] A. L. Read, "Modified frequentist analysis of search results (The CL(s) method)",
     in *Workshop on confidence limits, CERN, Geneva, Switzerland, 17-18 Jan 2000:*
     Proceedings. 2000.

[60] A. L. Read, "Presentation of search results: The CL(s) technique", *J. Phys.* **G28**
     (2002) 2693–2704. [,11(2002)]. `doi:10.1088/0954-3899/28/10/313`.

[61] CMS Collaboration, "Documentation of the RooStats-based statistics tools for
     Higgs PAG", *Internal CMS Wiki* (2015).
     https://twiki.cern.ch/twiki/bin/viewauth/CMS/SWGuideHiggsAnalysisCombinedLimit,
     Topic rev: r124.

[62] C. H. Chen, M. Drees, and J. F. Gunion, "Addendum/erratum for 'searching for
     invisible and almost invisible particles at e+ e- colliders' [hep-ph/9512230] and 'a
     nonstandard string/SUSY scenario and its phenomenological implications'
     [hep-ph/9607421]", `arXiv:hep-ph/9902309`.

1593